Crystal to Glass Transition and its Relation to Melting

Thesis by

Mo Li

In Partial Fulfillment of the Requirements
for the Degree of
Doctor of Philosophy

California Institute of Technology
Pasadena, California

1994

(Submitted May 5, 1994)

To my parents,
my wife and daughter

Acknowledgments

I would like to take this opportunity to express my sincere gratitude to my advisors, Professor William L. Johnson and Professor William A. Goddard, for their support, encouragement, and guidance, for the trust and freedom they have given me during the course of my graduate work, and for setting up an extremely fine example of intellectual integrity, creativity, and dedication. I feel indebted to them for their inspiration and influence on me that go far beyond my scientific carrer.

I wish to express my appreciation to Professors Vasek Vitek and Takeshi Egami in University of Pennsylvania who introduced me into the field of glass transition and computer simulation. I am greatly indebted to Professors Noel Corngold, David Goodstein, and Brent Fultz for the time they spent on reading my thesis and to Peter Weichman, David J. Webb, Carl E. Krill, Hans J. Fecht, Rainer Birringer, and Konrad Samwer for many stimulating discussions. I have the special pleasure of thanking Professor Konrad Samwer for his critical comments on and proofreading of my thesis.

My special thanks also go to my friends and colleagues in both Johnson and Goddard group for forming such a friendly and supportive environment.

I dedicate this thesis to my parents, my wife, and daughter. I would like to express my deep gratitude and appreciation to my wife for her love, friendship, support, encouragement, and sacrifice during the time of hardship and struggle. I dedicate this thesis to my daughter. Because of her, my life becomes meaningful.

Finally, I like to extend my heartfelt appreciation and thanks to my mother-in-law and late father-in-law for their invaluable helps and caring for my family.

Abstract

This work contributes to the understanding of thermodynamic aspects and microscopic mechanisms of the crystal to glass transition and its relationship to melting. The topological order to disorder transition was investigated primarily *in a model system consisting of* Lennard-Jones binary *solid solutions via molecu*lar dynamics simulations. Under constant temperature and pressure, thermodynamic properties and structures of the solid solutions are mainly determined by solute/solvent atomic size difference and solute concentration. At a critical atomic size difference and/or concentration, the transition was found to occur with extremely small latent heat and density change, but large softening of shear elastic constants. Microscopic details such as atomic configuration show that the transition is induced by collective topological defects created by differences in atomic sizes of the solute and solvent atoms. The inhomogeneity in atomic displacements caused by these defects was shown to be directly responsible for crossover of the transition from a first order transition to a continuous one. The fundamental difference between melting and the crystal to glass transition was demonstrated by their thermodynamic, dynamic, and structural behavior under different kinetic environments. It was shown that melting is intrinsically a first order transition, whereas crystal to glass transition can occur in a variety of forms that are crucially dependent on the kinetic constraints imposed on the solid phases.

Table of Contents

Chapter 1

Introduction

It is now well known that a metastable glassy phase can be obtained either from a liquid phase or from a gas phase by techniques that can greatly reduce the atomic mobility so as to prevent nucleation and growth of crystalline phases [1.1]. This thesis, however, deals primarily with a different type of glass formation that begins with a crystalline solid phase [1.2]. Unlike the liquid to glass transition where space symmetry of a parent phases is the same as that of the glass phase (although an entirely different symmetry, the ergodicity symmetry, is obviously broken at the liquid to glass transition [1.3]), the crystal to glass transition (CGT) involves two phases that have completely different symmetry. In this thesis, we shall investigate the nature of the transition and behavior of related thermodynamic properties, dynamic properties, and structural changes of both phases. We will focus our attention on microscopic mechanisms and collective behavior of atoms at the transition. In particular, we are interested in the effects of defects, microscopic strain and stress, and the role they play on destabilizing the crystallinity.

The only phase transition that closely resembles this type of topological order to disorder transition is thermal melting. When heated up to melting temperature, a crystalline phase transforms readily into a liquid. The liquid phase is topologically different from the crystalline phase in such a way that there exists no mapping, or transformation of atomic coordinates, so that the former can be continuously related to the latter [1.4]. A glass can be considered as a frozen liquid that has a similar static structure factor as that of a liquid above melting temperature. Atoms in a glass lack mobility and thus cannot diffuse as easily as in the liquid. If slow relaxation of the metastable glassy structure is neglected, atoms in a well equilibrated glass appear to be indefinitely locked into the instantaneous coordinates of a liquid phase. From this perspective, the crystal to glass transition can be regarded as a "melting" transition at which a crystalline phase becomes a configurationally frozen, metastable liquid.

Although such an analogy made between melting and the CGT neglects the dynamic aspect of the transition (a glass is different from a liquid dynamically; see mode coupling theory [1.5]), it certainly has facilitated the understanding of the crystal to glass transition tremendously [1.2, 1.6]. In this thesis, we shall review various theories and models of melting which have been extensively used to explain the crystal to glass transition. We will show that it is the difference in the imposed kinetic constraints that can differentiate melting and the crystal to glass transition.

The crystal to glass transition has been observed to occur in almost all types of crystalline solids, covalent, ionic and metallic systems [1.2, 1.7]. In the present work, much of our attention will be focused on metallic systems only. Because of simplicity of their structural units and isotropic interactions, each atom in a metallic system can be treated as a particle without internal structure. So it is relatively easy to study a metallic system, especially theoretically. Metallic glasses exhibit a variety of fascinating properties that range from magnetic, photoelectronic, and thermophysical as well as mechanical properties that other forms of condensed matter lack [1.8]. These properties make metallic glasses an extremely promising technological material to be used in various applications where conventional crystalline materials have failed to perform satisfactorily [1.1, 1.8].

Traditionally metastable metallic glasses are prepared by rapid quenching of melts at cooling rates of $10^4 \sim 10^7$ K/s [1.1, 1.8]. However, glasses obtained by these techniques are limited severely by their size and geometry. Because a large cooling rate is required, techniques such as rapid solidification and vapor deposition can only produce samples with one dimension greatly reduced. Applications for such thin metallic sheets or ribbons have been found to be very limited, despite the very promising properties these materials exhibit. In addition, these limitations have posed great difficulty for measurements of physical properties that are manifested on long wavelengths or large sample size.

To overcome the shortcomings in synthesis of metallic glasses, great efforts have been made in the last several decades [1.1, 1.2]. The crystal to glass transition, among the relatively successful attempts, has opened a new avenue for production of large sized, bulk metallic glasses not only for technological applications, but also for scientific investigation of physical properties of these materials. In addition, like melting, the crystal to glass transition has posed fascinating but extremely challenging problems for our understanding of topological order to disorder transitions and metastable phase transitions in general.

Topological order to disorder transitions are often associated with some types of internal or external perturbations on an ordered system that usually cause random displacements of atoms from the ordered state. The disordering is random in nature and is often manifested in the formation of a variety of defects [1.9]. In the case of melting, input thermal energy enhances vibrations of atoms and when the melting temperature is reached, the mean amplitude of random deviations of atoms from their lattice positions become so large that one can no longer associate each atom with the underlying equilibrium lattice position; thus a liquid phase forms. At elevated temperature, except very close to melting temperature, crystalline solids remain in thermodynamic equilibrium because thermal activation enables access to the entire phase space.

The types of external perturbations that can induce the CGT are not only large in number but also in variety. The CGT has been observed during irradiation of solids with high energy particles [1.10], hydrogen absorption by crystalline intermetallics [1.11], severe mechanical deformation of crystals [1.12] and solid-state interdiffusion reactions of elemental metals [1.13]. In the case of mechanical deformation induced CGT, externally applied stresses directly drive atoms out of their equilibrium positions, while in hydrogen and interdiffusion induced CGT, internal stress fields created by different chemical species drive each atom away from its underlying equilibrium lattice position. Unlike in melting, a solid phase that undergoes the CGT is often in a thermodynamic metastable state. The metastability is characterized by elevated free energies compared with the equilibrium crystalline phase under the same thermodynamic conditions, such as composition, temperature and pressure. The metastability is usually made possible by imposing kinetic constraints on the system during the course of the CGT. Usually this is achieved by keeping the system below the glass transition temperature. At such a low temperature, atoms lack sufficient thermal activation to execute long-range diffusion. So the system is able to retain its chemical homogeneity. The CGT under such a constraint is called polymorphic amorphization, or polymorphic melting. Maintaining such a condition is necessary in order to prevent other more stable phases from forming due to diffusion that can preempt the CGT. Various crystalline defects created during the course of the CGT will also be constrained from large scale rearrangement due to the low thermal activation, giving rise to the needed excess free energy to drive the metastable crystal to a glass. As shown later in this work, “frozen-in” disorder plays an extremely important role in destabilizing the crystallinity. Depending on temperature and certain material properties, “frozen-in” disorder can induce the CGT with characteristics that are similar to those of a smeared first-order phase transition.

In order to study a phase transition, the most convenient way is to relate thermodynamic properties to symmetry change, or to use an order parameter [1.14]. However, in a topological order to disorder transition, there are no apparent symmetry relations between the two phases. The lack of an underlying lattice in the disordered phase poses a great difficulty for mathematical analysis. So finding meaningful and manipulatable order parameters has always been a challenge. Certain physical quantities such as density and the Bragg diffraction intensities have been widely used in describing melting and vaporization transitions [1.15], but they will not serve the purpose for the CGT. This is because neither the liquid to glass transition nor the CGT necessarily involves any appreciable change in densities. In addition, an order parameter based on diffraction peaks contains many components that correspond to different reciprocal lattice vectors, making it very difficult to manipulate. Recently, orientational symmetry has been emphasized [1.16] that made the order parameter approach to the glass transition and melting possible [1.16-18]. The biggest challenge to this so called orientational order parameter approach comes from the experiments. So far, all results on atomic systems, mainly from computer simulations, are widely divided and still remain the subject of much debate [1.19, 1.20].

Such difficulties can be avoided, though not entirely, in computer simulations. The only limitation for computer simulation is sample size and available simulation time. With modern digital computers and efficient algorithms, one can perform simulations comfortably with a few thousands atoms for the real time equivalent of a couple of hundred nanoseconds. However, problems can still arise at phase transitions where extremely large critical fluctuations and critical slowing down can lead to diverging correlation lengths and relaxation times that are far beyond the sample size and available time [1.21]. If no special measure is taken, these effects can lead to very misleading results. Fortunately, techniques such as finite size scaling can offer help in reducing these problems to a tolerable level [1.21-22]. Additional problems arise in systems which contain certain random variables, such as the "frozen-in" random disorder and random substitutional solid solutions which we are going to deal with. The difficulties for a random system can be categorized into two kinds. One is insufficient sampling due to the limited distribution of random variables on a finite size sample. The finite size scaling can not cure this problem and an additional configurational sampling over the random variables is needed. Another problem is associated with slow relaxation due to low temperature of the system. So extended simulation time is need. The details will be presented in the next chapter. Computer simulation can also offer additional information relating macroscopic properties to microscopic parameters. For instance, by manipulating model interatomic interactions, one can tailor the system and thus relate the results to different real systems that have similar features in their interatomic interactions.

The primary reason for us to investigate the CGT using computer simulation stems from the difficulties experienced in synthesizing metastable crystalline phases which are chemically homogeneous, bulk, and free of extrinsic defects. So far, almost all the experiments conducted on the CGT use crystalline phases that contain macroscopic scale chemical inhomogeneity and a variety of extrinsic defects. The results obtained from these experiments at low temperature are kinetic in nature. Although attempts have been made in the last few years, the thermodynamic aspects of the transition is still far from understood [1.2, 1.23-24].

The most frequently encountered problem in a bulk metastable crystalline phase is caused by the failure to maintain kinetic constraints. Since the system is typically not in equilibrium and the metastable crystalline phase is frequently driven to evolve along competing pathways favored by other processes, so that keeping it homogeneous both in its chemical composition and structure becomes a real challenge. For example, chemical segregation and/or formation of more stable crystalline phases are frequently observed in bulk samples [1,23]. Furthermore, in real crystals, defects and imperfections, free surfaces and interfaces, etc., may serve as preferred nucleation sites for new phases and thereby complicate experimental observations.

Computer simulation provides an alternative method which can eliminate some of the problems encountered in experiments. With this method, it is possible to study the CGT on a homogeneous system that is free of these complications to the maximum possible extent. In addition, we can obtain detailed information about atomic structure, thermodynamic and dynamic properties of the metastable systems close to the CGT. It can also provide information such as heat capacity, thermal expansion coefficients and elastic constants, which is not otherwise available. The most profitable aspect of computer simulation is its ability to provide information on the atomic level. Then the macroscopic properties can be linked to their microscopic origins.

This thesis is organized as follows. In chapter 2 we shall give a brief introduction to the computational method, molecular dynamics simulation techniques. Since a large number of physical quantities are calculated, compared and analyzed later on, it is convenient to define them and give brief explanations of each of these quantities in this chapter. Thermodynamic potentials such as free energy, enthalpy and entropy, density, phase diagrams, and thermodynamic response functions such as thermal expansion, heat capacity and elastic constants, are of primary interest to identify the nature of the CGT. Time dependent properties such as the vibrational density of states, diffusion, mean square atomic displacements, and time dependent density-density correlation functions provide crucial information about dynamic characteristic of the system undergoing the CGT. For instance, the diffusional information obtained from mean square displacements, or density of states, can tell us directly whether the polymorphic constraint is in force or not, and how different types of atoms diffuse in a multicomponent system. Topological defects such as disclinations, dislocations and grain boundaries can be identified through a mapping technique using the Voronoi polyhedron construction. The information provided by this direct visualization of disorder will help us greatly to identify the role these defects play, and their manifestation in destabilizing the crystal. Random stress and strain associated with the randomly "frozen-in" disorder are analyzed through their distributions and their correlation functions in space. We also analyze the translational as well orientational symmetry at different stages of the CGT via spatial correlation functions. These correlation functions can give information on the nature of transition and its special relation to the symmetry.

We have found that it is convenient for various purposes such as visualization, to work in two and three dimensions separately. Chapter 3 deals primarily with the CGT in a binary Lennard-Jones random solid solution in three dimensions. Our emphasis will be on the elastic instability mechanism proposed for the CGT [1.2]. So the elastic behavior of the solid solution will be investigated as the amount of disorder increases [1.25].

In chapter 4 the results obtained in a three-dimensional system will be interpreted using a phenomenological Landau theory. The role of disorder will be explored by taking into account the interactions between the primary order parameter and a local, microscopic strain field. The consequence of this interaction is a profound one. It is found that the nature of a normal first order transition, such as the polymorphic melting, can be changed to a continuous one by the presence of microscopic strains. The observed thermodynamic properties and elastic properties in the three-dimensional simulation can be rationalized by this theory.

Due to the three-dimensional nature, the system of chapter 3 and 4 can not be examined thoroughly, except for the case of some important thermodynamic properties, and certain structural changes. So we have turned to a two-dimensional system in chapter 5 for these "hard-to-get" details of the microscopic features such as atomic configurations. This is the major content of chapter 5. Because of convenience in computations in 2D, a large amount of microscopic information is available, so the CGT can be investigated in detail. These results will be compared with those in 2D melting in order to examine the analogy proposed early, with particular emphasis on the effects of kinetic constraints.

Chapter 6 will give a brief summary of the present work and a discussion of the relation between melting and the CGT.

References

1.1 Elliott, S. R., *Physics of Amorphous Materials*, 2nd ed., (Harlow, Exxex, Englnad: Longman Scientific & Technical; New Yok, 1990).

1.2 Johnson, W. L., Prog. Mat. Sci., **30**, 81(1986).

1.3 R. G. Palmer, Adv. Phys., **31**, 669(1982)

1.4 Nash, C. and Siddhartha, S., *Topology and Geometry for Physicist*, (Academic Press, London, New York, 1983).

1.5 U. Bengtzelius, W. Götze and L. Sjögren, J. Phys. C: Solid State Phys., **17**, 5915 (1984); U. Bengtzelius, and L. Sjögren, J. Chem. Phys., **84**, 1744 (1986).

1.6 D. Wolf, P. R. Okamoto, S. Yip, J. F. Lutsko and M. Kluge, J. Mat. Res., **5**, 286 (1990).

1.7 A. Kouchi and T. Kuroda, Nature, **344**, 134 (1990)

1.8 *Glassy metals I, II*, edited by H.-J. Günthrodt and H. Beck, (Springer Verlag, Berlin, 1981).

1.9 D. R. Nelson, *Phase Transitions and Critical Phenomena* (Academic Press, London 1983), Vol. 7, pp. 1.

1.10 K. C. Russel, Prog. Mat. Sci., **28**, 229 (1985); *Phase Transformation During Irradiation*, edited by F. V. Nolfi (Applied Science, Engelwood, NJ 1983).

1.11 X. L. Yeh, K. Samwer and W. L. Johnson, Appl. Phys. Lett., **42**, 242 91983).

1.12 C. C. Kock, O.B. Cavin, C. G. McKamey and J. O. Scarbrough, Appl. Phys. Lett., **43**, 1017 (1981).

1.13 R. B. Schwarz and W. L. Johnson, Phys. Rev. Lett., **51**, 415 91983); S. R. Herd, et al., Appl. Phys. Lett., **42**, 597 (1983).

1.14 L. D. Landau and E. M. Lifshitz, *Statistical Physics*, 2nd edition, (Pergamon

Press, Oxford, 1080).

1.15 S. Alexander and J. McTague, Phy. Rev. Lett., **41**, 702 (1978).

1.16 D. R. Nelson and B. I. Halperin, Phys. Rev. B, *19*, 2457, 91979).

1.17 D. R. Nelson and J. Toner, Phys. Rev. B, **24**, 363 (1981); A. D. Haymet, Phys. Rev. B, **27**, 1725 91983).

1.18 P. J. Steinhardt, D. R. Nelson and M Ronchetti, Phys. Rev. B, **28**, 784 (1983).

1.19 R. M. Ernst, S. R. Nagel and G. Grest, Phys. Rev. B, **43**, 8070 (1991).

1.20 K. J. Strandburg, Rev. Mod. Phys., *60*, 161 (1988).

1.21 K. Binder, *Monte Carlo Methods in Statistical Physics*, Topics in Current Physics (Springer-Verlag, Berlin, 1986), Vol. 7.

1.22 V. Privman, *Finite Size Scaling and Numerical Simulation of Statistical Systems* (World Scientific Publishing Co., Singapore, 1990).

1.23 K. Samwer, H. J. Fecht and W. L. Johnson, *Glassy metals III*, edited by H.-J. Günthrodt and H. Beck, (Springer Verlag, Berlin, in print), chapter 2.

1.24 C. E. Krill, Ph.D. Thesis, California Institute of Technology, 1992.

1.25 M. Li and W. L. Johnson, Phys. Rev. Lett., **70**, 1120 (1993).

Chapter 2

Molecular Dynamics Simulation and Phase Transitions

2.1 Introduction

Computer simulation has been extensively used in the last several decades in investigation of physical properties and phase transitions. It has become an indispensable part of scientific research [2.1]. Its merits lay in the ability to provide essentially exact information of a system under investigation with only an arbitrariness introduced by interatomic interactions used. Unlike analytical approaches where problems have to be simplified very often in order to be made feasible, computer simulations can provide direct linkage between microscopic and macroscopic properties for any system without invoking any approximation. Such a characteristic makes it possible to use simulations to tackle problems where analytic approaches fail. Like any real experiment, computer simulation is performed in a fashion that is subjected to constraints from conditions provided by the system under investigation. Its power also lays in the fact that it can be applied to situations beyond the current experimental capability. However, like all its counterparts, computer simulation also has its own shortcomings and disadvantages. The most noticeable ones result from the finite size and finite simulation time. Effects caused by these limitations can become serious when a system is close to a phase transition. As discussed in the last chapter, critical fluctuations can lead to diverging length scale and relaxation time. Even for a typical first order phase transition, finite size can also present a big problem for nucleation and interface formation. Finite size scaling, a technique developed for reducing the same problem encountered in experiments, can effectively help to avoid the drawbacks in certain cases. However, there are other cases such as a random system where special measures have to be taken in order to reduce the effects of finite size effects.

In the following sections, we shall give a brief introduction to a specific simulation technique, molecular dynamics. Various physical quantities that are typically computed using this method will be introduced.

2.2 Molecular Dynamics Simulation Method

Molecular dynamics (MD) is a computer simulation technique used to generate phase space trajectories (atomic positions and velocities) for a collection of atoms. For a given interatomic interaction between atoms the corresponding Newton equations of motion for all the atoms in the system are integrated numerically for a set of discretized time steps. The MD ensembles generated from these trajectories provide linkage between microscopic properties and average thermodynamic properties. Equilibrium thermodynamic averages of a physical quantity A, equal the ensemble average,

$$< A >=< A >_{ensemble} \,. \tag{2.1}$$

If a system is ergodic, that is, if the ensemble average is the same as the time average, the thermodynamic average can be obtained from the time average over the trajectories generated from the MD,

$$< A >= \lim_{T\to\infty} \frac{1}{T} \sum_{\tau=0}^{\tau=T} A[\mathbf{r}(\tau); \mathbf{p}(\tau)], \tag{2.2}$$

where τ is the discretized time used in the simulation, T is the total simulation length, $\mathbf{r}(\tau)$ and $\mathbf{p}(\tau)$ denote collective symbols for atomic positions and momenta.

Depending on what extensive or intensive thermodynamic variables are fixed during a MD simulation, the ensemble generated can be different. For a system with N atoms, and total potential energy E and fixed density, or volume V, the ensemble is microcanonical (NEV); while if a system is kept at a constant temperature and density, it is a canonical ensemble (NTV). Since most experiments are done under constant pressure and temperature, the most desirable ensemble is the Gibbs ensemble (NPT). There are a variety of ways to generate a constant temperature ensemble, but the most convenient one is devised by Nosé [2.2]. Throughout this work, we shall use the Nosé algorithm to achieve the constant temperature.

In order to simulate an infinite system from a finite sample with N atoms, periodical boundary conditions are usually used. Atoms that moved out of the central simulation "box" at one side of the boundaries will be put back to the other side. This technique can eliminate boundary effects caused by a large fraction of atoms sitting on boundaries of a finite system. So its real function is to simulate a portion of an infinite system that is embedded in an infinitely large environment. For certain physical properties that only manifest on large scales, such as the composition fluctuations during phase decomposition and critical opalescence, a large number of atoms have to be used. So in this case, using the periodic boundary condition will not guarantee the accuracy of the properties from a simulation on a finite system.

2.3 Modified Parrinello-Rahman Molecular Dynamics

Most molecular dynamics simulations are performed in the microcanonical and canonical ensembles. In microcanonical ensemble, the total energy and volume are held fixed and in canonical ensemble, temperature and the density are held invariant. However, such constraint on certain thermodynamic variables can lead to an undesirable consequence, that is, fluctuations of these thermodynamic quantities from their equilibrium values are suppressed. Since fluctuations and responses of a system depend on the ensemble generated by the molecular dynamics trajectories [2.3], most of the thermodynamic response functions, particularly those relevant to structural variations, are not directly available.

Recently proposed molecular dynamics techniques attempt to remedy these difficulties. Andersen [2.4] was the first to use volume as a dynamic variable to allow fluctuation of the MD cell. Using this technique, he was able to extend molecular dynamics from microcononical and canonical ensembles to constant pressure and temperature (NPT) and constant pressure and constant enthalpy (NPH) ensembles. This idea of using macroscopic quantities as dynamic variables led Parrinello and Rahman [2.5] (PR) to propose a new molecular dynamics method which allows not only volume but also shape, or symmetry, variations of the MD cell. With Parrinello-Rahman molecular dynamics (PR MD), it is possible to study complicated problems like structural phase transitions and mechanical properties of materials where structural change is the primary concern. Most importantly, the response functions related to the symmetry change, such as elastic constants [2.6] and the thermal expansion coefficient, can be obtained.

Despite the promise of Parrinello-Rahman molecular dynamics, however, in practice it has been found to have several severe problems which make it difficult and unambiguous to interpret simulation results and, worst of all, lead to unphysical results. The primary problem is *symmetry variance*, or MD cell distortion, which occurs when a stable or equilibrium structure is used in a simulation and occurs even at zero temperature, when thermal fluctuations are completely absent.

In these cases, the MD cell distorts in a continuous manner and finally ends up in a structure of totally different symmetry. For example, *fcc* to *bcc* distortion has been observed and interpreted as a consequence of using pair potentials [2.5]. This is disturbing when investigating structure changes induced by structural phase transitions or mechanical deformation, because one cannot tell whether or not the structure variations are artificial or arise from true physical causes. (For example, the Bain transformation in iron involves the tetragonal distortion of the *fcc* cell.) Secondly, it has been found that PR MD often leads to MD cell *rotation*, which has been observed in molecular systems [2.7] as well as in simple Lennard-Jones solids [2.8]. Rotation of the MD cell indicates that the structure being simulated is not in mechanical equilibrium [2.9]. The direct consequence of such rotation is that it is almost impossible to find an equilibrium reference state for the calculation of strains and elastic constants. Besides, rotated coordinates make it difficult to interpret simulation results. The last and most practical issue is the very *slow convergence* of RP MD in calculating thermodynamic quantities such as the thermodynamic response functions, which are directly related to fluctuations or to derivatives of structure variations. It has been reported [2.10] that elastic constants of a simple Lennard-Jones solid have been obtained, but with very slow convergence. However, these results have not been confirmed as yet. In contrast, the present author found that it is impossible to calculate the elastic constants in nearest-neighbor LJ solids using PR MD, due to the above mentioned distortions and rotations. Furthermore, there are no reports of heat capacity, thermal expansion and compressibility calculated directly from fluctuations in Parrinello-Rahman MD simulations, even though extensive work has been done related to structural changes.

In practice, constant energy and shape (EhN) or constant temperature and constant shape (ThN) ensemble PR MD [2.6] are used to calculate C_P or C_V respectively, as well as adiabatic or isothermal elastic constants, while constant (NPT) or (NPH) ensemble PR MD are used to obtain equilibrium structures [2.11]. Since the volume and shape of a MD cell in constant (EhN) and (ThN) ensemble MD are fixed, distortions and rotations of the MD cell are no longer a concern. The calculated elastic constants and heat capacities using these fixed volume (or shape) PR MD has been found to converge very quickly [2.6]. However, it is inconvenient and time consuming to switch between different ensemble molecular dynamics in order to obtain the desired structures, fluctuations, and response functions. In particular, when the evolution of fluctuations and responses is needed for cases like phase transitions and structural variations, such shuffling among two or three different ensemble MD becomes quite a burden. Furthermore, since most experiments are performed under constant temperature and pressure, it is desirable for one to use constant (NPT) PR MD in which volume is allowed to fluctuate, to compare the results with experimental ones under the same conditions.

In this section we present a new version of the Parrinello-Rahman type with a modified kinetic energy term associated with the phenomenological dynamic variable of shape, or symmetry. We will test this algorithm by calculating certain thermodynamic and structural properties of a nearest neighbor Lennard-Jones solid. These results are shown to be in good agreement with those from existing Monte Carlo simulations [2.12,2.13] and those from constant shape, or symmetry, molecular dynamics simulations [2.6]. All of these results are obtained with fast convergence of only about 10^5 or less MD time steps.

In the original Parrinello-Rahman molecular dynamics, the shape, or symmetry, of the simulation MD cell is used as phenomenological dynamic variable. The cell is a parallelepiped with its edges represented by the three vectors **a**, **b** and **c**. The positions and velocities of particles in the MD cell are scaled by a matrix h, that is, $\mathbf{r}_i = h\mathbf{s}_i$ and $\dot{\mathbf{r}}_i = h\dot{\mathbf{s}}_i$, where $h = \{\mathbf{a}, \mathbf{b}, \mathbf{c}\}$. The Lagrangian proposed by Parrinello-Rahman includes phenomenological kinetic and potential terms for both the scaled particles and the MD cell,

$$L = \frac{1}{2}\sum_{i=1}^{N} m_i \dot{\mathbf{s}}_i^t G \dot{\mathbf{s}}_i - \sum_{i=1}^{N}\sum_{j>i} \phi(r_{ij}) + \frac{W}{2} Tr(\dot{h}^t \dot{h}) - P_{ext}\Omega, \tag{2.3}$$

where $G = h^t h$ is the metric tensor (h^t is the transpose of h), $\Omega = det|\mathbf{a} \cdot \mathbf{b} \times \mathbf{c}|$ is the volume of the MD cell, and P_{ext} is the externally applied pressure. W is the fictitious mass associated with the phenomenological dynamic variable h. A pairwise interaction $\phi(r_{ij})$ is assumed. The equations of motion for the time evolution of the dN particles, where d is the dimensionality of the system being simulated, and h matrix take the form

$$m_i \ddot{\mathbf{s}}_i = -\sum_{j \neq i} \chi_{ij} \mathbf{s}_{ij} - m_i G^{-1} \dot{G} \dot{\mathbf{s}}_i, \tag{2.4}$$

and

$$W \ddot{h} = [\sigma - P_{ext} I] A, \tag{2.5}$$

where $A = \frac{\partial \Omega}{\partial h} = \Omega h^{-t}$ is the area tensor (h^{-t} is the inverse transpose of h). σ is the microscopic stress tensor, which is defined as

$$\sigma = \Omega^{-1}[\sum_i \frac{\mathbf{p}_i \mathbf{p}_i}{m_i} - \sum_{i>j} \chi_{ij} \mathbf{r}_{ij} \mathbf{r}_{ij}], \tag{2.6}$$

with linear momemtum $\mathbf{p}_i = m_i h \dot{\mathbf{s}}_i$ and $\chi_{ij} = r_{ij}^{-1} \frac{\partial \phi(r_{ij})}{\partial r_{ij}}$. In PR MD the strain tensor is defined as [2.14]

$$\epsilon = \frac{1}{2} h_0^{-t} [G - G_0] h_0^{-1}, \tag{2.7}$$

where $h_0 \equiv < h >$ is the equilibrium MD cell under no external applied pressure or stress. It is used as the reference for strain calculation and $< \cdots >$ stands for time average.

The equation of motion for $\mathbf{s}_i$ in the constant (NPT) ensemble PR MD can be shown easily to take the form

$$m_i \ddot{\mathbf{s}}_i = f^{-2}[-\sum_{j \neq i} \chi_{ij} \mathbf{s}_{ij} - m_i(f^2 G^{-1} \dot{G} + 2 f \dot{f}) \dot{\mathbf{s}}_i]. \tag{2.8}$$

The Nosé scaling method [2.2] is used to fix the temperature, and f is the Nosé scaling variable. The equation of motion for h remains the same as in (3).

Using the equations of motion (2.4) and (2.8), we simulated a nearest-neighbor Lennard-Jones solid. We used 500 atoms arranged in a cubic cell with the fcc structure. Initially the atoms are kept at the positions corresponding to the Lennard-Jones potential well minimum, or the nearest neighbor distance is kept at $(2.0)^{1/6}$. Temperature and pressure are set equal to 0.3 and 0.0 (in reduced LJ units) respectively. The fifth-order Gear's predictor-corrector algorithm is used to solve the equations of motion. The length of time step in our MD runs is kept at 0.005 (in reduced LJ units). It is found that the cubic MD cell rotates continuously accompanied by a tetragonal distortion. For a typical run, at 500 MD steps the MD cell $h = (\mathbf{a}, \mathbf{b}, \mathbf{c})$ looks like

$$\begin{pmatrix} 1.56 & -7.27 & -2.46 \\ 5.32 & 2.93 & -5.04 \\ 5.55 & -0.89 & 5.73 \end{pmatrix}$$

with $|a| = 7.84, |b| = 7.89$ and $|c| = 8.02$. And the angles between each of the vectors are $\theta_{ab} = 90.64, \theta_{bc} = 91.80$ and $\theta_{ac} = 88.95$. With such rotation and distortion it is virtually impossible to find an equilibrium reference h_0 to calculate strain and elastic constants.

Since the PR molecular dynamics used above is not derived from first principles, in order to modify PR MD one must first check the invariance or conservation of dynamic and structural variables. First, the kinetic energy term associated with the h matrix is not invariant with the choice of the h matrix, or MD cell (which has been observed also by other researchers; Nosé and Klein 1983 [2.7], Cleveland 1988 [2.15] and Wentzcovitch 1991 [2.16]). However, in a system with translational symmetry two different choices of h are related by a transformation matrix B such that $h_2 = h_1 B$ and $\dot{h}_2 = \dot{h}_1 B$. Any dynamic or structural variable in such a system must be invariant with respect to the transformation. A simple choice of a new kinetic energy term

$$K_h = \frac{W}{2} Tr(\dot{h} Q \dot{h}^t), \tag{2.9}$$

where Q is chosen to be any linear function of $h^{-1}h^{-t}$, would eliminate the dependence of K_h on the choice of MD cell. Such a choice of Q makes the transformation of K_h with respect to different choices of MD cell invariant, that is,

$$\begin{aligned} K_{h_2} &= \frac{W}{2} Tr(\dot{h}_2 Q_2 \dot{h}_2^t) \\ &= \frac{W}{2} Tr(\dot{h}_1 Q_1 \dot{h}_1^t) \\ &= K_{h_1}, \end{aligned}$$

where $Q_1 \sim h_1^{-1} h_1^{-t}$ and $Q_2 \sim h_2^{-1} h_2^{-t}$. The proportionality constant C in $Q = C h^{-1} h^{-t}$ should be chosen as Ω^2 such that the kinetic energy approaches the isotropic limit when $h = \Omega^{1/3}\mathrm{I}$, where I is an unit matrix,

$$K_h = \frac{1}{2}W'\dot{\Omega}^2, \tag{2.10}$$

where the $W' = W/3$ is the mass associated with the MD cell volume. Eq. (2.10) was originally proposed by Andersen [2.4] to simulate the MD cell volume fluctuations in an isotropic media such as liquid and glass.

After replacing K_h, the new Lagrangian leads to a new equation of motion for the h matrix,

$$W\ddot{h} = \Omega^{-1}[\sigma - P_{ext}I]h + W\Omega^{-2}[-2\Omega\dot{\Omega}\dot{h} + Tr(\dot{h}Q\dot{h}^t)h + \dot{h}Q\dot{G} - \Omega A\dot{h}^t\dot{h}]. \tag{2.11}$$

The equation of motion for variable $\mathbf{s}_i$ remains the same as in equation (2.8).

In addition, the total angular momentum in RP MD is not formally conserved. We found that the nonconservation of angular momentum is related to the approximation used for the scaling relation for particle velocity, $\dot{\mathbf{r}}_i = h\dot{\mathbf{r}}_i$. In fact, this relation neglects the part contributed from the MD cell breathing, that is, $\dot{h}\mathbf{r}_i$. If the RP MD cell h is analogous to a "piston" or, a box with all its walls connected by mobile hinges, to maintain a constant pressure (stress in general) and temperature each atom has to exchange linear and angular momentum with the outside *heat bath* and *pressure or stress reservoir.* In an equilibrium system conservation of total angular momentum keeps the shear stress tensor symmetric, and thus the strain tensor symmetric, leaving the system unrotated [2.9]. Unlike most constant volume MD, the Parrinello-Rahman MD has orientational degrees of freedom for the MD cell (the h matrix has nine components, six of which specify shape and volume and the additional three describe orientation). Because of this, nonconserved total angular momentum can lead to net rotations at the end of a simulation, as we in fact observed. (Although the use of periodic boundary conditions also leads to total angular momentum nonconservation, weighting over a long time might be expected to average out such an effect). So neglecting $\dot{h}\mathbf{s}_i$ will not only lead to violation of the law of conservation of angular momentum but also the total linear momentum.

However, if the full expression $\dot{\mathbf{r}}_i = h\dot{\mathbf{s}}_i + \dot{h}\mathbf{s}_i$ is used in the formulation of a new MD, the resulted equation of motion for the h matrix will no longer depend on the microscopic stress tensor (2.6), even though all the conservation laws are obeyed. In the case of isotropic limit, it can be shown that the equation of motion for the MD cell becomes $W\ddot{h} = -P_{ext}$. For most cases the external pressure is zero, so the equation of motion for the MD cell is completely decoupled from the rest of the system. This may explain the justification of neglecting the second term in the original proposal by Andersen [2.4]. A more convincing argument for the approximation is based on the fact that fluctuations of the wall (h tensor) is much slower than the scaled particles (with coordinates $\mathbf{s}_i$). Typically, the ratio of the frequencies of MD cell fluctuation to the scaled particle vibration is $\frac{1}{10}$ to $\frac{1}{100}$ in an equilibrium monoatomic Lennard-Jones solid. Therefore, one can neglect the MD cell fluctuation. However, close to structural phase transition the MD cell fluctuates more quickly and on the other hand, particle vibration becomes slower, such the approximation may not be valid. In fact, we have observed certain distortions and rotations of the MD cell in systems close to the CGT.

There are certain empirical measures one could take to reduce the effects of rotation and distortion. The most effective ones are as follows. First one can increase the MD wall mass and second, one can set the initial atomic configurations as close as possible to the equilibrium or steady one. These tricks were found to be able to reduce the problem to a tolerable level. But the underlying mechanism has not been clear yet.

Using Eq. (2.8), (2.11) and the following one for the Nosé variable f

$$M\ddot{f} = \frac{2K}{f} - \frac{2(D+1)T}{f}, \tag{2.12}$$

where M is the mass for Nosé variable f, K is the kinetic energy of atoms in Eq. (2.3) and D is the number of degrees of freedom of the system, we calculated the nearest neighbor Lennard-Jones solid again using this new formulation. The distortion and rotation have not shown up in these calculations and the average thermodynamic properties converge very rapidly with a chosen optimal MD cell mass W. Average total energy, MD cell edge lengths and the angles between them for the nearest neighbor LJ solid become stable at 5×10^4 and 10^6 MD steps. All of the average properties have reached equilibrium in at most 10^4 MD steps. The fluctuations and hence the response function calculated show excellent agreement with those calculated from Monte Carlo [2.12-13] and constant (NhT) MD [2.6]. From the convergence of fluctuations we conclude that the ensemble generated from Eqs. (2.3), (2.11) and (2.12) is a Gibbs ensemble and is ergodic.

2.4 Thermodynamic Properties and Fluctuations

Thermodynamic properties that are of great interest to understand phase transitions are thermodynamic potentials and response functions. These include Gibbs free energy G, entropy S, enthalpy H, the total potential energy E, kinetic energy K, density D, isothermal heat capacity C_p, thermal expansion α_T, compressibility κ_T and isothermal elastic constants, etc.. At a phase transition, these quantities will often show dramatic changes. In particular, thermodynamic response functions, which are second derivatives of thermodynamic potentials, are extremely sensitive to the changes. A first-order transition usually shows finite changes of latent heat or entropy and finite change of density. In addition, very little precursor effects can be seen far away from the transition. In contrast, the thermodynamic functions change continuously at a continuous transition and thermodynamic response functions usually show large precursor effects quite far away from the transition; and they diverge and show singular behaviors at the transition [2.17].

Except for free energy and entropy, the rest of the thermodynamic quantities are straightforward to calculate using MD. For instance the total potential energy and enthalpy are obtained easily by

$$E = < \sum_{i>j} \phi(r_{ij}) > \tag{2.13}$$

and

$$H = E + P_{ext}\Omega, \tag{2.14}$$

where $\phi(r_{ij})$ is a pair potential, P_{ext} is the external pressure and Ω is equilibrium volume. Calculation of absolute free energy and entropy needs special treatment because they are not functions of mechanical variables, $\mathbf{r}_i$ and $\mathbf{p}_i$, rather they are functions of phase space variables. In order to obtain them, one needs to sum over all the states in the phase space.

The thermodynamic response functions have close connections to such subtle properties as thermal fluctuations in the system. At a continuous phase transition, the fluctuations will become extremely large and result in divergent response functions [2.17]. The fluctuations and response are related through expressions

$$< (\delta H)^2 >= k_B T^2 C_P, \tag{2.15}$$

$$< (\delta \Omega)^2 >= \Omega k_B T \kappa_T, \tag{2.16}$$

$$< (\delta \Omega \delta H) >= \Omega k_B T^2 \alpha_T, \tag{2.17}$$

$$< (\delta \epsilon_{ij} \delta \epsilon_{kl}) >= \frac{k_B T}{\Omega} C^{-1}_{ijkl}, \tag{2.18}$$

where Ω is the equilibrium volume, T the temperature and ϵ the strain tensor defined in Eq. (2.7). C_P, κ_T, α_T and C_{ijkl} are isobaric heat capacity, volume isothermal compressibility, thermal expansion coefficient and isothermal elastic constants respectively. The time average of fluctuations is given by $< \delta A \delta B >=< AB > - < A >< B >$, where A and B are functions of the dynamic variables. The elastic constants are inversely related to the strain fluctuations [2.14].

2.5 Dynamic Properties

Dynamic properties are characteristics of time dependent processes in the system and are closely related to the transport properties. An advantage of a molecular dynamics simulation, compared with other simulation techniques such as Monte Carlo method, is that it can calculate time dependent properties naturally from the trajectories generated. For instance, the Einstein relation relates the mean square displacements of atoms to diffusion constants,

$$D = \lim_{t \to \infty} \frac{1}{6t} < \delta r^2(t) >= \lim_{t \to \infty} \frac{1}{N} \sum_{i=1}^{N} < |\mathbf{r}_i(t) - \mathbf{r}_i(0)|^2 >, \tag{2.19}$$

in a three-dimensional system, where D is the diffusion constant, t is time and N the total number of atoms. The average is over the ensemble at the initial time

$t = 0$, or over the time origins chosen along the trajectories. From the slope of the $< \delta r(\mathrm{t})^2 >$ versus t, one can obtain the diffusion D.

Transport properties can also be obtained from time correlation functions by so called Green-Kubo relation [2.18]. The velocity-velocity autocorrelation function can also lead to diffusion constants through its Fourier transform at low frequency limit. The velocity autocorrelation function is defined as

$$Z(t) =< \mathbf{v}(t) \cdot \mathbf{v}(0) > / < \mathbf{v}(0) \cdot \mathbf{v}(0) >, \tag{2.20}$$

where $\mathbf{v(t)}$ is the particle velocity. Fourier transform of $Z(t)$ gives rise to the so called generalized vibration density of states.

Other time correlation functions that are relevant to the CGT are time dependent density-density correlation functions and time dependent orientational correlation functions defined as follows,

$$G(\mathbf{r},t) = \frac{1}{N} < \rho(\mathbf{r},t)\rho(0,0) > \tag{2.21}$$

and

$$O(\mathbf{r},t) = \frac{1}{N} < \psi(\mathbf{r},t)\psi(0,0) >, \tag{2.22}$$

where $\rho(\mathbf{r},t)$ and $\psi(\mathbf{r},t)$ are particle density and orientational order parameter respectively. The later will be defined in next section. The Fourier Transform of G($\mathbf{r}$, t) gives rise to the dynamic structure factor $S(\mathbf{k},\omega)$ which can be measured by inelastic neutron scattering [2.19].

2.6 Topological Defects

We are interested in topological defects for the following reasons. First, they can directly alter the topological ordering and second, they can result in nonhomogeneous, "frozen-in" microscopic strain and stress field. As demonstrated in the next chapter, the static strain field has a significant effects on the CGT. In this section, we shall define these defects.

The structure of a topologically disordered metallic glass is conventionally described by radial distribution functions (RDF) which can be readily obtained from most scattering experiments. Since it is a two-body density-density correlation function averaged over all directions throughout the entire sample, in principle the RDF can not provide local information on atomic arrangements over a scale of a few nanometers. For instance, the split second peak of a RDF present in most of metallic glasses could not be explained until Bernal's dense random packing model (DRP) [2.20] was available. The detailed atomic arrangements in the disordered material available in models such as the DRP and the computer simulations [2.21] that followed also led to the possibility of the description of topological defects. The distribution of the five different types of Bernal's polyhedra [2.20] and the deviations of certain faces and volumes from a crystalline counterpart in the Voronoi polyhedra [2.21] in glasses are examples of the attempts to describe structure of glasses by certain irregularities or disorder in these geometrical quantities.

In fact, description of defects in topologically disordered materials has been a very difficult task owing to the fact that they do not possess any reference lattice as in the crystalline counterpart (where topological defects are often associated with breaking of translational symmetry). For example, the usual way to identify a dislocation in a crystalline phase using Burgers circuit [2.22] becomes meaningless without a reference lattice. However, topological disordering of a glass phase can be presented, to at least some extent, by changes of the *nearest neighbor coordinates* of the atoms [2.23]. The defects defined in this way are clearly confined to the local atomic arrangement and therefore, any topological disordering beyond the scale of the nearest neighbor is not adequately presented. So strictly speaking, the definition of topological defects in a glass phase does not necessarily have the same physical content as in its crystal counterpart, even though the same name may be used without specification of this distinction.

Identifying such topological defects in crystalline and noncrystalline materials is conveniently done by examining the nearest neighbor coordinates of each atom with the help of certain mapping techniques. The most reliable method to obtain nearest neighbors of an atom is the Voronoi polyhedron construction [1.1]. A Voronoi polyhedron of an atom, or Voronoi cell, is defined as a region bounded by planes bisecting the vectors connecting the center of the atom to these of its nearest neighbors. A Voronoi Polyhedron in a Bravis lattice is a Wagner-Seitz cell which has the same point group symmetry as that of the lattice. However, a disordered, glassy phase lacks any long-range translational symmetry. Since the edges (E), vertices (V) and faces (F) of Voronoi polyhedra obey Euler-Poincaré relation

$$V - E + F = 2, \tag{2.23}$$

in three dimensions, the absence of the translational symmetry, or the topological order in a glass is reflected by the distorted geometry (the relative variations of lengths of the edges, areas of faces, numbers of faces and vertices, etc.) and varying volumes of its Voronoi cells. The topological disordering is characterized by the random fluctuations of these geometrical entities from one Voronoi cell to another throughout the system [1.1, 2.21].

Using the definition stated above, we can define different types of topological defects in crystalline or amorphous solids from their nearest neighbor coordinations.

Because the symmetry of local order is the same as that of the lattice in crystalline solids, this definition of topological defects for crystalline solids is not restricted to their local atomic configurations. Defects defined by their nearest neighbor coordinations are the same as defined on an infinitely large system. However, deviations from this observation occur in disordered phases where low energy, local ordering, such as icosahedral clusters, does not possess the same symmetry as that of the crystalline lattice, so care must be taken in this case. Topological defects can be defined easily in two dimensions by directly mapping out the nearest neighbors. Some commonly encountered defects in two dimensions will be presented as follows.

Line defects include disclinations and dislocations. A disclination in a close packed hexagonal lattice can be defined as a defect centered on an atom which has a number of nearest neighbors different from the average coordination number. Most frequently observed ones are 5- and 7-nearest neighbor disclinations which are termed "negatively" and "positively" charged disclinations (Fig. 2.1). A disclination can not only destroy long range translational order but also orientational order. A dislocation (only edge dislocations exist in two dimensions) is composed of an extra row of atoms along one of the close packed directions (in order to have the smallest Burgers vector). Such a configuration can be decomposed into two disclinations with opposite charges (Fig. 2.2). A dislocation with an extra row of atoms can effectively destroy translational order but leave the orientational order intact.

However, complications can arise in two dimensions because of the degeneracy of the configurations of line defects and point defects. For instance, a Frankel pair composed of an interstitial and a vacancy separated only by a few lattice spacings

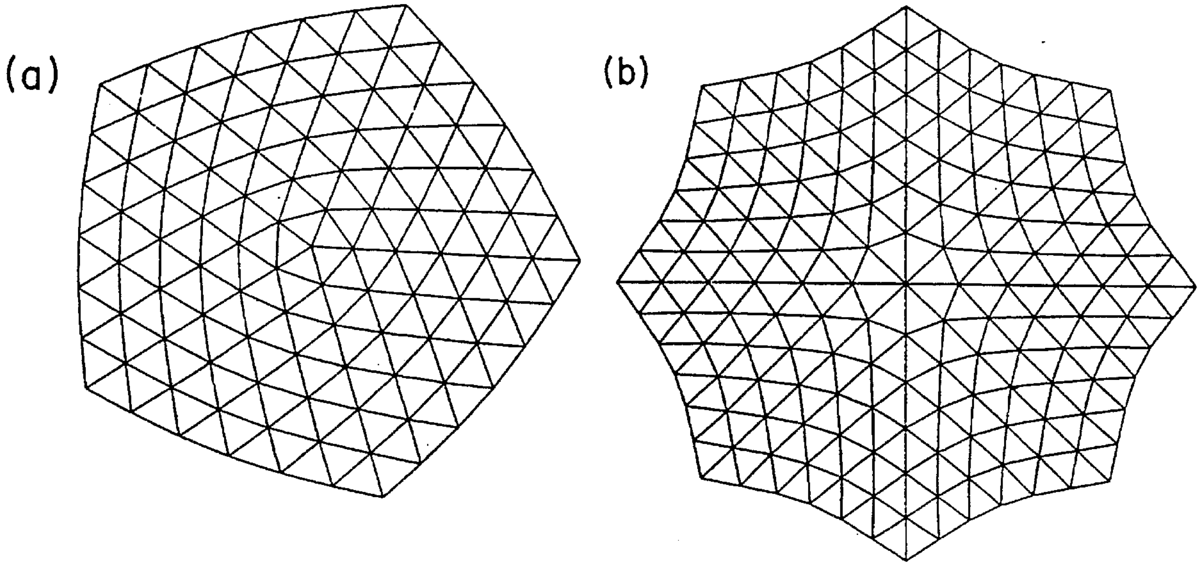

Fig. 2.1 Disclinations in a two-dimensional hexagonal lattice. Crystal orientations change by 60° along a circuit enclosing both disclinations. They can effectively disrupt orientational order and translational order of the lattice. Note they can be identified by nearest neighbor coordinates. (a) a disclination with 5 nearest neighbors (negatively charged) and (b) a disclination with 7 nearest neighbors (positively charged).

apart, after some local relaxation, can look the same as a dislocation pair from two dislocations consisting of two 5- and two 7-nearest neighbor disclinations.

The definition of disclination and dislocation will be carried directly to the case of amorphous materials, although, as we mentioned early, their physical meaning is not quite the same. But they offer certain help for comparison of how these defects evolve from crystalline phases to amorphous phases.

Planar defects are grain boundaries and stacking faults in crystalline phases. But the number of planar defects in an amorphous phase is considerably restricted compared with its crystalline counterpart due to the absence of translational symmetry, or lattice periodicity. Strictly speaking, whether the equivalents of the planar defects exist or not in amorphous solids is still not entirely clear [2.23]. This may justify the classification of defects by only nearest neighbor coordinations.

As well known, a grain boundary in a crystalline phase can be considered as composed of large number of dislocations. A small angle grain boundary is composed of relatively smaller number of edge dislocations, the identity of which can be well resolved. In contrast, a large angle gain boundary is densely packed with dislocations and the identification of each dislocation is almost impossible. Two adjacent grains are separated by a grain boundary across which they have different orientations. In two dimensions, a grain boundary or any other two-dimensional defect degenerates into a line defect and thus the identification of these defects is mainly by visual inspection of their atomic configurations (Fig. 2.3).

Identification of topological defects in three dimensions faces essentially two difficulties. First, there has been lack of direct experimental evidence of extended defects in amorphous materials so far, although indirect evidence has shown the existence of point "defects" similar to those found in crystalline materials [2.23]. The absence of lattice periodicity and open packing in amorphous phases make it difficult to observe the defects (for instance, strain contrast cause by dislocations in crystalline materials is not available in amorphous materials). This leads to the conclusion that extended defects are "delocalized" by which it is meant that an extended defect like a dislocation in three dimensions will be broken up into

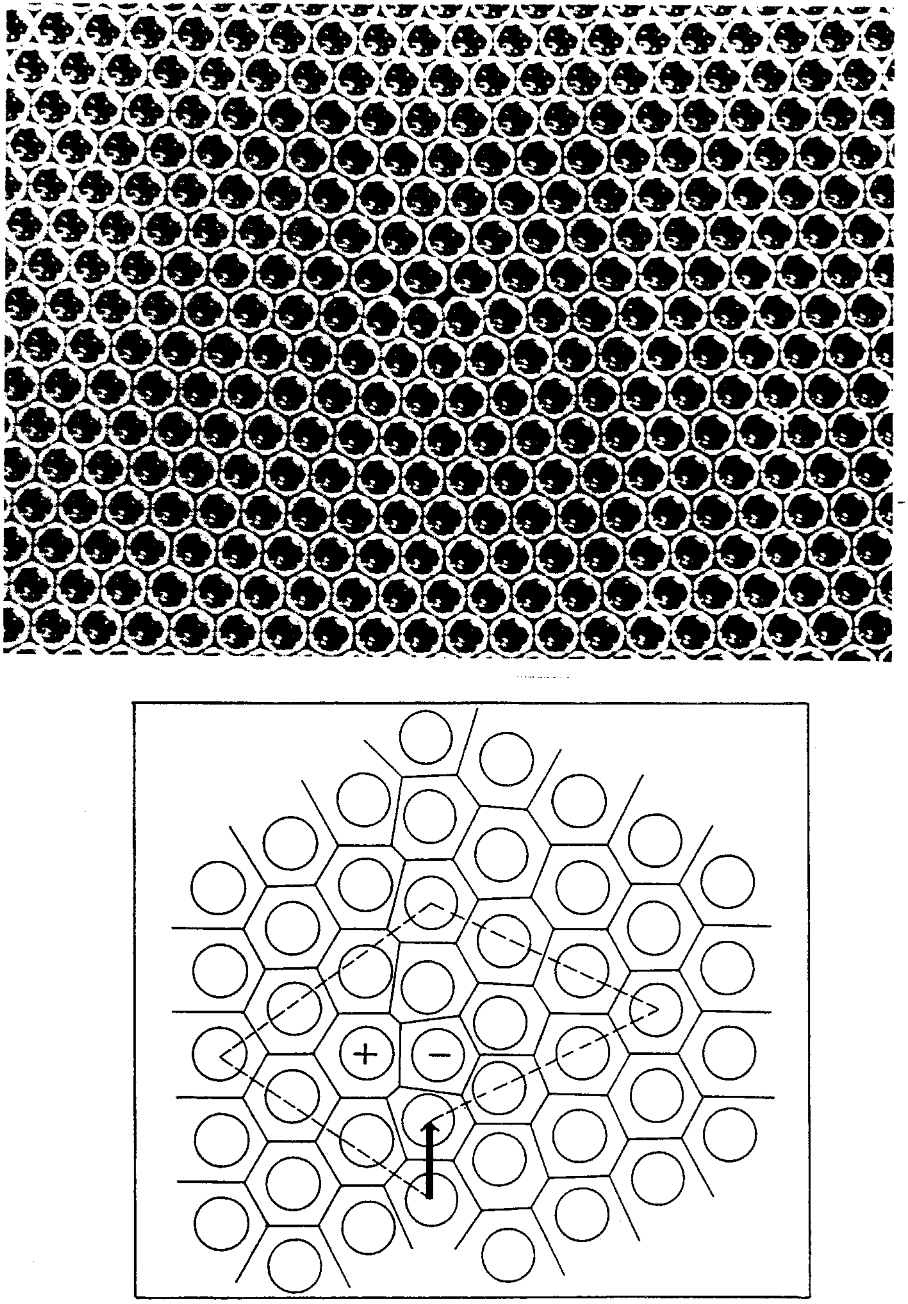

Fig. 2.2 An edge dislocation in a two-dimensional hexagonal lattice. Note the extra atomic planes. It can effectively disrupt translational order of the lattice, but leave orientational order intact. *Top*: an edge dislocation formed on a bubble raft [2.26] and *Bottom*: such a dislocation can be decomposed into two disclinations [2.27].

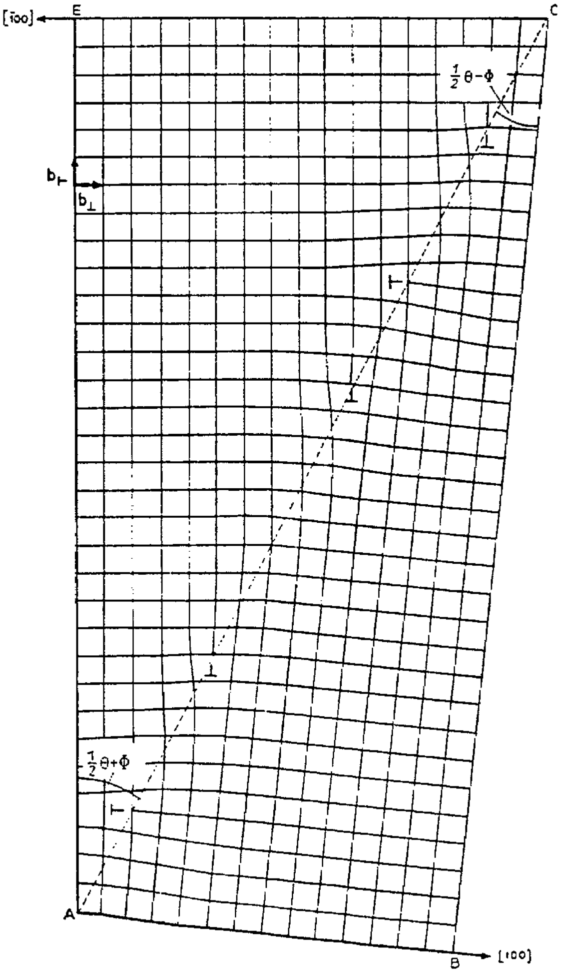

Fig. 2.3 A small angle asymmetric grain boundary made of edge dislocations with perpendicular Burgers vectors [2.28]. Note it can not only interrupt translational order but also orientational order in the adjacent grains.

segments of a few lattice spacings with no correlations between each of them either in direction or configurations. This leads to a more fundamental question of very existence of any extended defects at all. However, recent theories [2.24, 25] have predicted that at least line defects like disclinations can be stable in amorphous phase, but as stated earlier, no direct observations have been available for these defects yet.

As mentioned earlier, the defects, the topological defects and point defects such as solute atoms (an impurity in a supersaturated solid solution), have nonhomogeneous strain and stress field associated with them [2.22]. The internal, microscopic fields can be retained by the kinetics. This static field from the frozen configuration of defects can play an important role in affecting crystalline stability.

Before ending this section, we like to mention some technical problems associated with identifying the nearest neighbors using Voronoi Polyhedron construction in multicomponent systems. The usual way of bisecting the vector connecting the nearest neighbor atoms will lead to errors due to the different atomic sizes, which sometimes can be substantial. Bisecting the nearest neighbor bond in order to local planes of a Voronoi polyhedron can misidentify atoms as the nearest neighbors in such a system. In the present work, we used the Radical Plane method [2.29] to identify nearest neighbors in the binary solid solution.

2.7 Symmetry, Order and Microstructures

The absence of any long-range symmetry in a topologically disordered phase does not necessarily exclude the possibility of existence of other local ordering. The well defined first and often, second peaks in RDF of most glassy phases indicate that atoms in these materials are arranged in a quite orderly manner on that scale. The local ordering therefore is not an exception but a common characteristic of glasses. However, the manifestation of this local ordering can be quite different in its size, in the atomic configurations, and in its chemical ordering.

It has long been argued that a glass can be represented by an ensemble of microcrystals with completely random orientations of each grain [2.30-31]. However, the RDF's constructed from this model agree only qualitatively with experimental measured RDF's [2.31] or RDF's constructed from DRP [2.20]. Unfortunately, this issue was not pursued further after initial attempts [2.31]. Recently, this matter was addressed, not from direct structural modeling, but from kinetic properties of crystalline and amorphous phases [2.32]. According to this proposal, a microcrystal is different from an amorphous phase in its kinetic behavior on nucleation and growth. A microcrystal, when heated up, needs only to grow, while an amorphous phase needs to first underdo nucleation and then grow. Isothermal calorimetry close to the crystallization temperatures would be able to distinguish the difference.

However, atomic disordering on the scale of a few nearest neighbor coordination shells involves the configurational changes on the scale of a critical crystal nuclei. Also local inhomogeneities in chemical compositions and densities in amorphous phases can further complicate the issue, making it difficult to distinguish a true amorphous phase, as depicted by the DRP model [2.20], and a microcrystal-like ensemble. This issue will become more clear when results on two-dimensional solid solutions are presented in chapter 5.

To observe any local ordering and collective behavior of atoms, correlation functions of a variety of physical quantities representing symmetry and composition distributions are needed. First, we define the correlation functions of translational and orientational order. A translational order parameter is defined as

$$\rho_{\vec{G}}(r) = e^{-i\vec{G}\cdot\vec{r}}, \tag{2.24}$$

where $\vec{G}$ is a reciprocal vector of a perfect lattice and $\vec{r}$ is the position of an atom.

The translational correlation function is defined as

$$C_{\vec{G}}(r) = < \rho_{\vec{G}}(r) \rho_{\vec{G}}(0) > . \tag{2.25}$$

It is directly related to the structure factor in Bragg diffractions at a specific reciprocal vector $\vec{G}$,

$$S(\vec{G}) = \frac{1}{N} \sum_{i=1}^{N} \sum_{j=1}^{N} < e^{-i\vec{G}\cdot\vec{r}_i} e^{-i\vec{G}\cdot\vec{r}_j} > = \sum_{i=1}^{N} C_{\vec{G}}(\vec{r}_i), \tag{2.26}$$

where N is the total number of atoms in the system. From Eq. (2.25) it is clear that all atoms contribute to the diffraction intensity at $\vec{G}$ for a system with long-range translational order and only fraction of the atoms will contribute if short-range translation order exists. The correlation length within which the translational symmetry is preserved defines the size of a crystal-like entity.

An orientational order, which presents orientation of local crystallographic axes (for instance, directions of atomic planes), can be defined by a so called bond orientational order parameter [1.16-19],

$$\psi_m(r) = e^{-im\theta(\vec{r})}, \tag{2.27}$$

in two dimensions, where $\theta(\vec{r})$ is the angle that a vector connecting an atom to its nearest neighbor makes with respect to a reference axes. $m = 6$ for a hexagonal lattice and $m = 4$ for a square lattice. In three dimensions, $\psi_m(r)$ is defined as a spherical harmonic $Y_m^l(r)$ [1.18]. The orientational correlation function is defined as

$$C_m(r) = < \psi_m(r) \psi_m(0) > . \tag{2.28}$$

The correlation functions defined above are closely related to the local ordering. The change in their magnitudes and the correlation lengths can reveal possible mechanisms of disruptions of this type of ordering due to the presence of topological defects. The spatial extension and local symmetry of local ordering in a topologically disordered phase can also be measured by these correlation functions. For instance, a collection of atoms that are locally ordered can form certain types of configurations with relatively lower energy [1.18, 2.33] in an isotropic glass phase. This locally ordered atoms form icosahedral clusters [1.18] that can be measured by the bond orientational correlations functions. It was found that such local order possesses five-fold point symmetry, thus long translational arrangement is not possible, but orientational order over a relatively long range is not prohibited [1.18].

2.8 Atomic Displacements, Frozen-in Random Strain and Stress

There are two equilibrium conditions a system must satisfy in order to be in a metastable system. One of these conditions is thermodynamic equilibrium and another is mechanical equilibrium. It is very important to distinguish them, especially in the case of the CGT and melting. For example, a point defect is in thermodynamical equilibrium at any finite temperature, but mechanically it is not. A dislocation in three dimensions is mechanically stable but thermodynamically it is not in equilibrium. The mechanical equilibrium is determined by either boundary conditions or constraints on mechanical variables that cannot be either included in the system's Hamiltonian or can not be intergrated in the partition function. In the CGT or any metastable phase transition, the thermodynamic metastable equilibrium caused by defects and kinetic constraint plays a crucial role in determining the phase stability.

In the next chapter we shall use a binary solid solution as a model system to demonstrate how the CGT proceeds. In this system, two types of atoms are mixed together randomly to form a metastable solid solution. Atomic configurations, or local packing formed by these two atoms are not in mechanical equilibrium if the atomic size difference between them exceed certain limits. Such nonequilibrium arrangement will result in enormously large stress on atoms in the vicinity of the solute atom. This stress field is defined as in (2.7) for each atom. This stress field, $\sigma(\mathbf{r}_i)$, is randomly distributed in space because the mismatching solute atoms are randomly distributed in solid solution. These "impurity" atoms are the source of stresses. The atoms that are affected by these stresses can relax to reach an equilibrium. However, under the kinetic constraint, large atomic coordination arrangements are prohibited, but local, small amplitude ***atomic displacements*** could occur. In general, not all the atoms that are displaced can reach equilibrium. A certain number of these atoms can form topological defects because mechanically they are stable. This case includes dislocations, grain boundaries and interfaces. These defects will have inhomogeneous strain and stress fields around them [2.22] that can in turn influence the atomic displacements. Depending on specific kinetic constraints imposed on the system, the configuration and density of these defects can change dramatically. If the temperature is low, these nonequilibrium, random, defects and thus the strain field can be retained. This *"frozen-in" strain field* will be shown to play a crucial role in determining the metastable phase stability, the CGT, (chapter 4), and in distinguishing melting and the CGT (chapter 6).

2.9 Finite Size Scaling

The finite size effects on MD simulations are from two different origins. The first is related to some intrinsic length scale of the systems that is larger than the system size used in MD. This happens mostly when systems are close to phase transitions. A second order transition can be affected most seriously because of the diverging correlation lengths at the transition. A first-order transition can also be influenced by a finite size sample in simulations of critical nucleation which requires far more atoms than one can currently handle. The large fraction of atoms sitting on interfaces will prohibit the possible phase fluctuations and lead to large hysteresis, and sometimes even disappearance of the characteristic of the first-order transition. Systematic methods have been developed for eliminating the finite size effects that occurred in experiments [1.22]. This so called finite size scaling of a variety of physical quantities as function of system sizes has been found to be quite satisfactory. In computer simulations, similar scaling relations can be applied to eliminate finite size effects. This technique will be tried for a two-dimensional Lennard-Jones solid solution at the CGT.

The second is attributed to the realization of probability distributions of certain random variables on a finite sample. For a random variable $R(r)$ distributed on a finite sample, its probability distribution $\mathrm{P_R}$ will approach the correct value if only the sample size goes to infinity (or sufficiently large). If the sample is not large enough, the random distribution can-not be realized. The same problem was encountered in spin glasses [2.34] where probability of having a true random distributions of spin configurations is also restricted by finite system sizes. To get rid of this size limitation, an additional average is performed over the ensemble of random spin configurations on a finite system size, that is,

$$<< A >>=<< A >>_{random-configuration}, \tag{2.29}$$

where the $< A >$ is the usual thermodynamic average over a MD ensemble. In MD simulation, generating such the ensemble of random configurations cannot be done as naturally as in Monte Carlo simulations, so we chose to take the average over several different runs with different initial conditions on a finite system. In practice, we found that in atomic system, averages over several different (usually around ten), initial random configurations are adequate to get satisfying convergence.

In addition, there is a particular aspect of finite size effects related to the MD method we used. If the size is below certain threshold value, an obvious MD cell distortion will arise. This artificial structural change is found to be related to the nonhomogeneous distributions of random solute atoms in a finite sample. The minimum MD cell size is obtained by increasing the system size by trial and error until no distorsions are observed.

References

2.1 K. Binder, Monte Carlo Methods in Statistical Physics, Current Topics in Physics (Springer Verlag, Berlin 1986); G. Ciccotti, D. Frenkel and I. R. McDonald, *Simulation of Liquids and Solids*, (North-Holland, Amsterdam 1987).

2.2 S. Nosé, Mol. Phys., **52**, 255 (1984).

2.3 J. L. Lebowitz, J. K. Percus and L. Verlet, Phys. Rev., **153**, 250 (1967).

2.4 H. C. Andersen, J. Chem. Phys., **72**, 2384 (1980).

2.5 M. Parrinello and A. Rahman, Phys. Rev. Lett., **45**, 1196 (1980).

2.6 J. R. Ray, Comput. Phys. Rept., **8**, 109 (1988).

2.7 S. Nosé and M. L. Klein, Mol. Phys., **50**, 1055 (1988).

2.8 M. Li and W. L. Johnson, Phys. Rev. B, **46**, 5237 (1993).

2.9 L. D. Landau and E. M. Lifshitz, *Theory of Elasticity*, 3rd ed. (Pergamon Press, OXford 1986), pp. 4-7.

2.10 M. Sptrik, R. W. Impey and M. L. Klein, Phys. Rev. B, **29**, 4368 (1984).

2.11 C. Massobrio and V. Pontikis, Phys. Rev. B, **45**, 2484 (1992).

2.12 E. R. Cowley, Phys. Rev. B, **28**, 3160 (1983)

2.13 W. Westera and E. R. Cowley, Phys. Rev. B, **11**, 4008 (1975).

2.14 M. Parrinello and A. Rahman, J. Chem. Phys., **76**, 2662 (1982).

2.15 C. Cleveland, Phys. Rev. B, J. Chem. Phys., **89**, 4987 (1988).

2.16 R. M. Wentzcovitch, Phys. Rev., B, **44**, 2358 (1991).

2.17 L. E. Reichl, *A Modern Course in Statistical Physics* (University of Texas Press, Austin, 1980).

2.18 R. Kubo, J. Phys. Soc., **12**, 570 (1957); M. S. Green, J. Chem. Phys., **22**, 398 (1954).

2.19 S. W. Lovesey, *Neutron Scattering from Condensed Matter* (Clarendon Press. Oxford, 1984).

2.20 J. D. Bernal, Nature, **183**, 141 (1959); Nature, **185**, 68 (1960); Proc. Roy. Sco., Ser. A, **280**, 299 (1964).

2.21 J. L. Finney, Proc. Roy. Sco., Ser. A, **319**, 479 (1970).

2.22 F. N. R. Nabarro, *the Theory of Dislocations* (Oxford University Press, Oxford, 1967).

2.23 F. Spaepen, J. Noncrystalline Solids, **31**, 207 (1978).

2.24 N. Rivier and D. M. Duffy, J. Phys (Paris), **43**, 293 (1982).

2.25 M. Kléman, J. Phys (Paris), **43**, 1389 (1982); M. Léman and J. F. Sadoc, J. Phys. Lett. (Paris), **40**, L569 (1979).

2.26 W. L. Bragg and J. F. Nye, Proc. Roy. Soc., A**190**, 474 (1947).

2.27 J. P. McTague, D. Frenkel and M. P. Allen, *Ordering in Two Dimensions*. edited by S. K. Shinha (North Holland, Amsterdam, 1980).

2.28 W. T. Reed, *Dislocations in Crystals* (McGraw-Hill, New York, 1953).

2.29 W. Fischer and E. Kock, Z. für Kristallographie, **150**, 245 (1979).

2.30 A. I. Gobanov, *Quantum Electron Theory of Amorphous Conductors* (Consultants Bureau, New York, 1965).

2.31 G. S. Cargill III, *Solid State Physics*, **30**, 227 (1975).

2.32 C. L. Chen and F. Spaepen, Mat. Sci. Engr. A, **133**, 342 (1991); Phil. Mag. B, **63**, 585 (1991).

2.33 M. R. Hoare, J. Noncrystalline Solids, **31**, 157 (1978).

2.34 K. H. Fisher and J. A. Hertz, *Spin Glasses* (Cambridge University Press. Cambridge, 1991).

Chapter 3

Lattice Instability Mechanism for Crystal to Glass Transition

3.1 Introduction

In this chapter, we shall give a brief introduction of thermodynamics and kinetics of metastable solids with emphasis on effects of kinetic constraints (see [1.2] for a detailed review). We will focus on polymorphic amorphization in multicomponent alloy systems. In particular, the concept of polymorphic melting will be introduced that relates a metastable, homogeneous, crystalline phase to an amorphous phase, or a diffusionless undercooled liquid at the CGT with no composition change. The CGT was considered as a transition from a topologically ordered phase to a disordered phase. The same symmetry relation suggests that the CGT is analogous to melting and therefore, the CGT results from crystalline *lattice instability* in the same way as in thermal melting. In 3.3 we will review some instability criteria and models an emphasis on elastic instability, atomic displacements, and atomic strains. In 3.4 we shall present results from a MD simulation of a model system, a Lennard-Jones (LJ) binary random solid solution. Elastic behavior shall be emphasized in this work, along with other quantities that characterize the transition. However, inherent difficulties resulted from requirements of large sample size and long simulation time, and visualization of atomic configuration and defects in the three-dimensional system have limited us from further exploring the transition. In 3.5 we shall compare these results with experimental ones. The observed lattice instability, represented by elastic constant softening, and seemingly continuous phase transition will be explained by a phenomenological Landau theory in the next chapter. This theory illustrates the importance of random, "frozen-in" strains and its role in altering the nature of the transition. Detailed work in two dimensions, where the computational limitations can be greatly reduced, will be given in chapter 5.

3.2 Thermodynamics and Kinetics of the CGT

Although thermodynamic properties are formally defined for systems at equilibrium, analogous quantities such as thermodynamic potentials and relationships among these quantities can also be used in metastable systems provided that the relaxation time, τ_R, of the metastable system toward equilibrium is longer than experimental observation time, T, that is,

$$\tau_R < T < \tau_K, \tag{3.1}$$

where τ_K is the characteristic time at which kinetic constraints remains effective. If this condition is satisfied, thermal averages can still be obtained by the time average (equation (2.2)). The ensemble average (equation (2.1)) is no loger uniquely defined since the ergodicity hypothesis assumed for an equilibrium system does not hold for a metastable system [3.1].

In section 2.8, we mentioned one type of metastability caused by *boundary conditions*. This type of metastability often happens to systems with extended structural defects, such as dislocations, grain boundaries and free surfaces. The stress field generated by these defects cannot dissipate because of the presence of certain boundary conditions [3.2]. So the free energy of these systems will be higher than the same system having no imperfections. Metastability can also be achieved under a more general condition, or under *kinetic constraints*. This constraint is more profound because of its effects on microscopic processes and collective motions of atoms. The kinetic constraint is to slow down relaxations of atoms and defects to more stable states. It can also couple to boundary conditions to enhance the metastability.

In multicomponent alloy systems used for the CGT, a kinetic constraint is applied by holding a crystalline phase below the glass transition temperature. At such a temperature, long-range diffusion is restricted, so the atoms must remain in a fixed configuration, no matter how unfavorable it is energetically. If an amorphous phase can be obtained from such a metastable crystalline phase without any substantial development of composition fluctuations on macroscopic scales, we call this type of CGT *polymorphic amorphization.*

The importance of the polymorphism in the CGT has to be stressed here for the following reasons. First, it is a truly metastable phase transition. The constraint on composition fluctuations can lead to the possibility of the CGT driven or altered by frozen-in atomic disorder (see chapter 4). Second, it is the simplest transition that involves only topological configurational change at the CGT. The polymorphic amorphization can be characterized by a well defined metastable phase diagram. The phase boundary connecting a crystalline phase and an amorphous phase is polymorphic melting temperature, T_0, which is an analogue of the melting temperature of a multiple component system at different compositions. T_0 provides a conceptual linkage between equilibrium thermal melting at high temperature and metastable CGT at low temperature [1.2].

Fig. 3.1 is a schematic metastable phase diagram for a binary system constructed from a related equilibrium phase diagram with an eutectic reaction. T_0 is defined in the same way as for melting in a pure system except that the locus of the Gibbs free energies is of a liquid (L) and a solid solution (see Fig. 3.2). The polymorphic melting line can be extended conveniently down to low temperature if metastability can be maintained by satisfying (3.1) for both phases.

The polymorphic CGT is likely to occur below T_g, the glass transition temperature where diffusion is known to be extremely slow, in a crystalline solid solution with excessive solute concentrations (beyond the equilibrium solubility). In this work, we shall limit ourselves to such a system which could exhibit polymorphic amorphization transitions.

In practice, however, achieving this condition (3.1) has been found to be extremely difficult. Other processes are likely to interfere with the metastable phase. Most commonly encountered are formation of equilibrium intermetallics and other undesirable metastable phases. Fundamental parameters determining the stability of these processes, e.g., τ_R, are critically dependent of kinetics of the formation of these phases in metastable systems during the course of the CGT. Usually there is a broad distribution of τ_R's that result from different time scales of these processes, while, on the other hand, there are only a few kinetic constraints one can manipulate to make τ_K satisfying (3.1). To make a homogeneous, "clean" metastable crystalline phase that can transform into an amorphous phase polymorphcally has been a great challenge for experimentalists (for example, see [1.2, 1.24]).

The crystalline solids used in most existing methods of synthesizing amorphous phases have large scale chemical inhomogeneity. Typical examples are diffusion couples [1.13], mechanical deformation induced amorphization [1.12], etc. In addition, the presence of defects created during processing of these materials, particularly

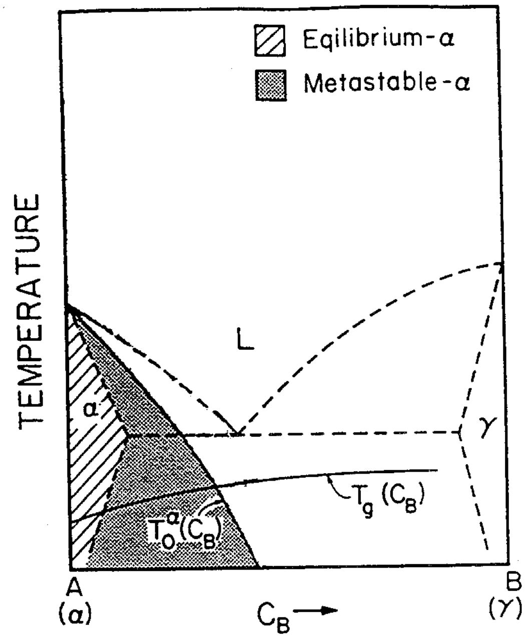

Fig. 3.1 Schematic phase diagram for a metastable binary solid solution constructed from an equilibrium binary phase diagram (dashed line) which has an eutectic crystallization transition. C_B is the solute concentration. α and γ are two equilibrium terminal solid solutions. Beyond the equilibrium solid solubility line, low temperature equilibrium phase is a two-phase mixture composed of α and γ. L refers to equilibrium liquids. $T_0^\alpha(C_B)$ is the polymorphic melting line. $T_g(C_B)$ is glass transition temperature. The cross hatched region shows the equilibrium solid solution and the shaded region shows the metastable solid solution. The CGT likely occurs below $T_g(C_B)$ and beyond $T_0(C_B)$, or in the shaded area.

those of topological nature such as dislocations and grain boundaries that can break the crystalline translational symmetry efficiently, can induce the CGT locally. In all of these experiments, it is indeed observed that the CGT proceeds in a manner strikingly similar to that of a first-order phase transition: nucleation of amorphous

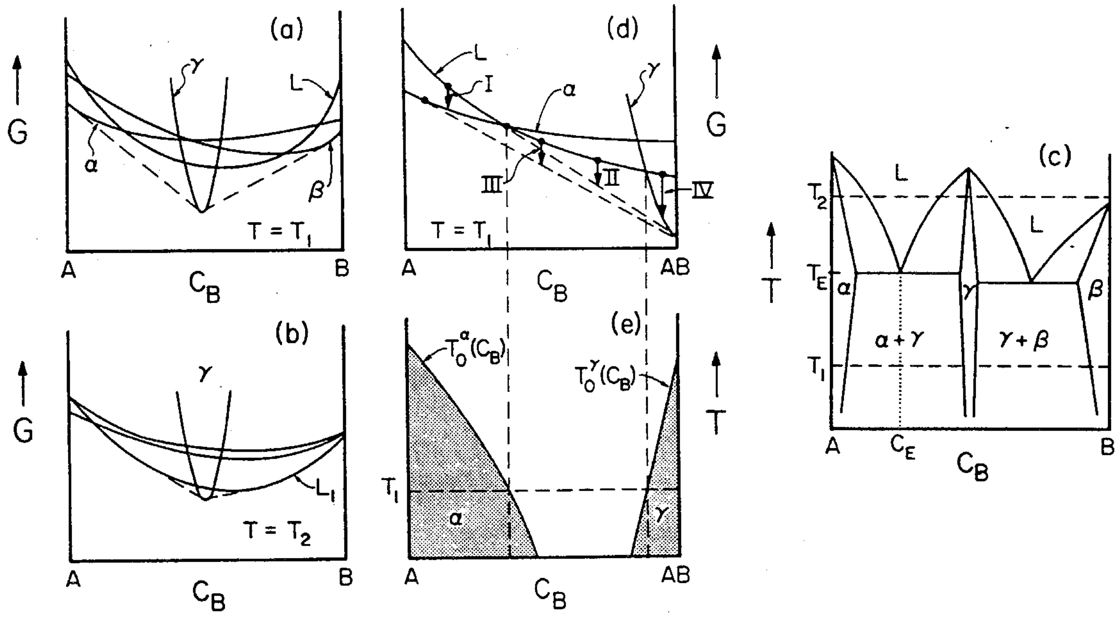

Fig. 3.2 (a) Schematic free energy diagram (temperature T *vs.* composition C_B) of a binary system at a temperature below solidus; (b) free energy diagram at a temperature between the solidus and liquidus; (c) binary phase diagram with two eutectic transitions; L is liquid, α and β are terminal solid solutions, and γ is an intermetallic compound; (d) polymorphic transition (I and IV), primary (II) and eutectic (III) transition from an undercooled liquid; (e) T_0 line for terminal solid solution α, γ and liquid L (from Ref. 1.2).

phase at boundaries of regions of chemical inhomogeneities/defects and subsequent growth of the amorphous phases controlled by either the crystal/amorphous interface or diffusion through both phases [3.3].

To understand intrinsic, microscopic mechanisms of the CGT and thermodynamic properties of metastable solid solutions, we need to use systems that are free of these inhomogeneities and geometrical constrains. There are only a handful of such systems available, one is the rare earth-transition metal intermetallics in which hydrogen can be absorbed quickly and homogeneously, and another is our computer generated solid solution for which a bulk, homogeneous metastable crystalline phase can be easily obtained. Radiation induced amorphization can produce homogeneous metastable crystalline and amorphous phases, but due to the special nature of disordering it is kinetic transition rather than a thermodynamic one [3.4, 3.5].

3.3 Criteria for Lattice Instability

The next question one likes to ask is why and how a stable, homogeneous crystalline metastable phase becomes unstable and transforms to a metastable amorphous phase? Because of the special nature of the CGT that involves topological configurational change of atoms, lattice instability is naturally introduced to relate this transition to lattice response [1.2], in particular, elastic properties.

Instability of a phase can be described in general by Gibbs criterion that sets limits for the stability of a phase (stable or metastable) against perturbations of different kinds [3.6]. Depending on the type of disturbances, Gibbs stability criterion takes different forms,

$$\frac{\partial^2 G}{\partial \epsilon_{ij} \epsilon_{kl}} = C_{ijkl} > 0, \tag{3.2}$$

$$\frac{\partial^2 G}{\partial c^2} = \frac{\partial \mu}{\partial c} > 0, \tag{3.3}$$

$$\frac{\partial^2 G}{\partial T^2} = -\frac{C_P}{T} < 0 \tag{3.4}$$

and

$$\frac{\partial^2 G}{\partial P^2} = -V\kappa_T < 0, \tag{3.5}$$

where G is Gibbs free energy, and c, T, ϵ_{ij}, V and P are composition, temperature, elastic strain tensor, volume and hydrostatic pressure, respectively. The positive definiteness of the thermodynamic response functions, such as chemical potential gradient, $\partial\mu/\partial c$, heat capacity, C_P, elastic constant, C_{ijkl}, and compressibility, κ_T, mark a stability region for a phase against small variations of these thermodynamic variables.

However, it is not adequate to employ the instability approach for phase transitions, because it cannot answer the questions of what the resulting phase is going to be and how a transition proceeds. These questions are, in fact, essential for understanding phase transitions [3.7-8]. Nevertheless, they could offer a quick reference, or criterion, for analysis of phase stability when detailed information is not available. The CGT, as well as melting, happen to fall into this category. Much of the understanding of the CGT up to date has been derived from instability approaches for thermal melting. In the remainder of this section, we shall critically review some of these criteria proposed for both the CGT and melting.

A. Elastic Lattice Instability Criterion

It is one of the most intuitive ways of relating a crystalline phase to an amorphous phase at the CGT [1.2]. When a crystalline phase becomes amorphous, it is no longer stable configurationally and thus the associated structural response, elastic constants, will exhibit certain changes at the transition, or vice versa. Born [3.9] proposed this model for melting in 1939 based on the observation that a liquid can not support acoustic shear waves. The collapse of crystalline order can therefore be represented by the disappearance of, at least, one of the shear elastic constants at melting. The free energy density proposed for such a crystalline phase is composed of elastic energy only, which is expanded in a power series in terms of strain tensor,

$$F = \frac{1}{2} \sum_{i,j,k,l} C_{ijkl} \epsilon_{ij} \epsilon_{kl}, \tag{3.6}$$

to quadratic terms. The expansion coefficients are elastic constants, C_{ijkl}. The stability of crystalline phases requires that the free energy be positive definite. From the definition (3.6), we know that this can be achieved only when the expansion coefficients, elastic constants, are positive definite. For a cubic Bravis lattice, the Born stability criterion can be obtained conveniently by expressing (3.6) in principal (eigen) strain coordinates. Diagonalizing (3.6), we obtain the stability condition for a crystalline solid with cubic symmetry,

$$C_{11} + 2C_{12} = \frac{3}{\kappa} > 0, \tag{3.7}$$

$$C_{11} - C_{12} > 0 \tag{3.8}$$

and

$$C_{44} > 0, \tag{3.9}$$

where C_{11}, C_{12} and C_{44} are three independent elastic constants. κ is compressibility constant. Eqs. (3.7-9) are just a specific expression of Gibbs elastic stability criterion expressed in (3.2). As mentioned early, this approach cannot tell how the elastic constants behave when a crystal gets closer to melting and what happens if the stability condition is violated. At $T = T_{instability}$, the curvature of the free energy, or an elastic constant, becomes zero. The crystalline solid loses the restoring force even against an infinitesimal structural fluctuation., and melting should occur. But with only the quadratic terms included, Born's theory predicts a catastrophic transition that will proceed without a bound. This is why the Born theory is called one phase theory of melting, or elastic instability of melting.

To avoid this problem, or to turn the one phase theory into a two-phase theory, higher order terms have to be included, as suggested by Landau theory of phase transitions [3.8], to stabilize the final phase after the parent phase has collapsed. But it is not clear whether or not the strain can be used as an order parameter in the case of melting, because essentially there are only dynamic (high frequency) shear strains in liquid state. Thus it is impossible to extend Born's stability criterion to a two-phase theory of melting by including higher order strain terms. However, we will show in chapter 4 that in a metastable crystal, a frozen liquid, or an amorphous solid, strains and stresses are perfect order parameters for a Landau theory.

Contrary to the expectation that a solid cannot support shear waves [3.9] at melting, it has been observed experimentally that elastic constants remain finite for most solids when the transition occurs [3.10-11]. A careful analysis by plotting elastic constants versus volume expansion, however, reveals that at melting, at least one of shear elastic constants, when extrapolated from the crystalline phase region and across the crystal/liquid expansion gap, does go to zero at a volume expansion corresponding to a liquid phase [3.10-11]. This result suggests that the *volume expansion* can be used as an indicator for lattice instability of metastable solids [1.2, 1.16]. It simply states that if the volume expansion of a crystalline phase exceeds that of a liquid, it will not be stable elastically.

This criterion derived from lattice instability actually fails on two accounts for understanding of the CGT, and melting in general. First, it may exaggerate the needed volume expansion for the CGT, since experiments have shown that glass differs little from its crystalline counterpart in densities [3.12]. Volume expansion at melting is typically around 5%, while the density change for glass is usually less than 1 $\sim$ 2%. Second, it gives no information on *local* changes in the crystalline phase. The melting transition in general can be regarded as originating from local regions that are full of structural imperfections. Locally, Born's criterion may be met in regions along the crystal/liquid interfaces. But experimentally measured elastic constants are over the entire sample that includes both crystalline and liquid regions, as in a typical first-order transition. So elastic constants can approach zero only when liquid regions percolate through the entire sample. This explains why Born criterion fails to predict behavior of elastic constants at melting. The same author found [3.10-11] that the number of atoms that are in a true liquid state, or executing diffusion motion, with the volume expansion at which a shear elastic constant becomes zero, is only about 10% of the total number of atoms. The fraction of liquid-like region agrees quite well with the critical volume predicted from volume percolation model [3.12].

The critical volume expansion criterion was tested [3.13] recently in a Lennard-Jones monoatomic solid. In this work, the volume of the crystalline solid was artificially expanded uniformly and subsequently held fixed. It was found that the crystalline solid starts developing microcracks at the volume expansion corresponding to the critical expansion. At a higher temperature, the microcracks are replaced by microcavitations. Under both conditions, the topological configuration of the solid bears no resemblance to an amorphous solids.

Despite the inadequacies mentioned above, lattice instability still remains an attractive approach because of its connection between configurational, or structural change and the elastic responses that a system can demonstrates at a transition. In the case of CGT, one expects that changes in volume or density from a crystalline solid to an amorphous solid will be much smaller than that of a liquid, as required by the critical volume expansion criterion if Born stability criterion applies. This is partially due to slow kinetics that constrains the glass-like regions from percolating fast and efficiently. So lattice instability, even if it occurs, will be more gradual and exhibit large precursor effects. Indeed the results in an expanded LJ solid mentioned above [3.13] support this argument.

B. The Generalized Lindemann Criterion

This approach represents another class of approaches that use mean square displacements (MSD) of atoms as an indicator to set a limit for crystalline stability [3.14]. Mean square atomic displacements can be measured from the reduction in intensity of the Bragg diffraction peaks of a crystalline phase. In melting the major part of mean square displacements comes from lattice vibrations of atoms from their equilibrium positions, whereas in the CGT, the static displacements of atoms contributes a large fraction to the total mean square displacements [3.15-17]. The MSD directly measures an average magnitude of disordering resulting from atomic configurational changes. Thus it represents a general characteristic for all structurally disordered processes.

Based on this consideration, the MSD, or in general atomic displacements fields, can be used as an order parameter to represent configurational disordering in transitions between a crystalline and an amorphous phase. As an indicator, or criterion, the MSD is not as useful to represent the topological transition, because it is the mean, average value taken over the entire sample that is used *at* the transition.

So the MSD used in Lindemann's criteria unavoidably suffers from the same problem as that in the critical volume expansion criterion derived from the lattice instability. It is unable to give any local information of the transitions and the manner of how the transition proceeds. For example, as shown later in this thesis, behavior of mean square displacements for a first-order and a continuous topological transition are quite different. The former usually shows a abrupt change very close to the transition, whereas the later exhibits a smooth change with a large precursor effect [3.18].

C. Microscopic Strain and Stress

Microscopic strains resulted from atomic displacements can be defined in general as

$$\epsilon_i = \frac{1}{2}(J_i^t J_i - I), \tag{3.10}$$

where J_i is the Jacobian Matrix

$$J_i = \frac{\partial \mathbf{u}_i}{\partial \mathbf{a}_i}. \tag{3.11}$$

$\mathbf{u}_i$ is atomic displacement vector from *equilibrium positions* of the ith atom, $\mathbf{a}_i$. The microscopic strain defined above is not limited to infinitesimal displacements, as in linear elasticity theory. It includes nonlinear displacements.

Such defined atomic strain and stress defined by equation (2.6) can be shown to be related to macroscopic stress σ and strain ϵ by

$$\sigma = \sum_{i=1}^{N} < \frac{\rho}{\rho_a} J \sigma_i J^t >, \tag{3.12}$$

where ρ and ρ_a are densities of strained and unstrained systems, and

$$\epsilon = \frac{1}{N} \sum_{i}^{N} < \epsilon_i > . \tag{3.13}$$

Microstress and strain have been widely used to relate structural disorder in solids and liquids [3.19-20]. For a solid phase, crystalline or amorphous, when in their stable (equilibrium or metastable) states, any unfavorable configuration of atoms that is different from the equilibrium configurations can introduce nonzero forces that can lead to nonzero stress. When a liquid is quenched rapidly, the atoms have no time to reach a equilibrium position, then the microscopic stress may result. This "frozen-in" microscopic stress was shown to be directly responsible for the liquid to glass transition [3.19-20]. At the liquid to glass transition the shear stress-stress correlation function approaches a finite value. Similar concept was also used to predict the onset of the CGT in intermetallics caused by irradiations [3.21].

As we briefly mentioned previously, nonzero microscopic stress corresponds to a mechanically nonequilibrium state. Relaxation of atoms to reach a local equilibrium under the action of these stresses in general is accessible, except in the case of rapid cooling. Most systems that are unstable mechanically will be relaxed to a metastable or stable state. However, if defects are present, this relaxation will not be accomplished fully, especially at low temperature, then microscopic static stress and strain field will result.

It is clear from the above analysis that microscopic strains should be considered in topological order to disorder transitions in metastable systems. Its close relationship with defects and to elastic properties make it a very useful quantity to analyze the transition. In the next chapter we shall present a simple Landau theory that uses microscopic strains as an order parameter to explain the CGT.

D The Entropy Crisis, or Inverse Kauzmann Paradox

This approach sets a different stability limit for a solid phase by an argument similar to that of Kauzmann's [3.22]. Kauzmann argued that a liquid cannot be supercooled indefinitely because, at some point, the entropy of a solid would be greater than that of a liquid, which is against the common sense. In order to avoid such a paradox, the liquid must decrease its entropy with cooling in order to approach that of a solid. This leads to massive freezing into a glass.

Strictly speaking, Kauzmann's paradox does not violate any thermodynamic law, or stability criterion, except that the extrapolated entropy of the supercooled liquid will become negative if it does not approach that of the solid. The glass transition temperature defined by the entropy crisis therefore is an ideal, thermodynamic glass transition temperature, or isentropic glass transition temperature.

The same concept was used in a rather different situation [3.23], superheating, which is inverse from that of Kauzmann's. It was argued that entropy of a superheated solid cannot be greater than that of a liquid. The temperature that defines the equality of entropies of a solid and a liquid is an "intrinsic, ultimate" stability limit of a superheated crystal [3.23]. This argument was elaborated and extended to multicomponent alloy systems at low temperature where a crystalline phase transforms polymorphically, or is superheated to "melt" into a glass at a nonequilibrium composition.

In order to achieve this entropy crisis, or to raise the entropy of a solid close to/above that of a liquid, defects have to be considered. The vibrational entropy, represented by increasing heat capacity, is not enough. However, the number of point defects needed is much larger than any experimentally observed value [3.23]. Furthermore, as we will show later, the collective defects play a more important role than the point defects in destabilizing crystallinity. The point defects are seldom found in disordered metastable crystals, even very close to the CGT. It is grain boundaries and dislocation networks, which, ironically, have less contributions to entropy than point defects, that can effectively destabilize crystallinity.

To summarize, stability arguments, presented as various criteria that are either directly related to thermodynamic quantities (Gibbs criterion, Born lattice stability, Kauzmann paradox) or other physical properties (generalized Lindemann's criterion and microscopic stress/strain), can only be used as a technique for rough estimation of the occurrence of a phase transition. Detailed information must be sought by other means that relate to the thermodynamic properties of the two phases, and link microscopic properties to observed phenomena. However, these physical quantities, especially those that are directly related to topological transitions, such as microscopic stress/strain, the MSD of atoms, are extremely useful for our understanding of melting and the CGT.

Because the averaged properties are used, stability criteria in general will lead to exaggerated values for phase transitions, i.e., higher transition temperature, larger magnitude of disordering, stronger correlations of ordered phases, etc.. Also detailed precursor effects, if there are any, will not be correctly presented by the stability criteria because they are closely related to local effects. Despite all the drawbacks associated with instability criteria, they can still be very useful as a quick reference for predicting phase stability in cases where no other detailed information is available.

3.4 The CGT in a Binary Lennard-Jones Solid Solution

As we mentioned early, in order to probe the "would-be" intrinsic mechanisms of the CGT and thermodynamic properties of both crystalline and amorphous phases, it is desirable to have a system that is *chemically homogeneous* and contains *no extrinsic defects.* A genuine system of this kind, however, is rarely obtainable experimentally (see [1.2, 1.24] for details). Rare earth metal hydrides mentioned early have shown early promise [3.24-26], but detailed work later [3.27] showed that in Fe_2Er-hydride neither of these requirements for polymorphic amorphization is met. The biggest problem is the short-range ordering resulting from strong rare earth metal-metal atom interactions [3.27]. A hydride made from Zr_3Al did, on the other hand, exhibit a transition in regions free of chemical inhomogeneity and defects [3.25]. In the remainder of this chapter, we shall present results for the CGT in a model system that meets these demands, even on microscopic scales.

A binary solid solution is the simplest system that can be made glassy with cooling rates accessible to most experimental techniques. A monoatomic system can become glassy, but its stability critically depends on its impurity content. An extrapolation of substrate temperatures *vs.* solute composition in NbSi indicated that substrate temperature needs to go to zero in order to form a monoatomic metallic glasses [3.28]. Thus amorphous phases are unstable thermodynamically. Atoms in the amorphous phase of pure metals are simply kinetically frozen into a disordered phase due to lack of mobility at such low (often cryogenic) temperatures.

The easy glass forming ability of multicomponent alloy systems has been attributed to constraints on kinetics that can prevent nucleation and growth in an undercooled liquid. Empirical relationships have been sought to correlate glass formability to certain material properties, such as enthalpy of mixing, *atomic size ratio*, or atomic size difference of solute and solvent atoms in binary mixture. The later has been considered as a crucial factor [3.29-31]. Atomic size mismatch can affect the *topological packing* of an alloy directly through altering its coordination numbers. A large atomic size ratio can also lead to *anomalous, asymmetric diffusion* for one of the species, which kinetically favors undercooling and thus glass formation [1.2]. In crystalline solids, solute solubility was thought to be related to atomic size differences between solute and solvent by *strain energy* created by size mismatch. Under such conditions, the maximum solubility of a solute in a binary solid solution is reached when solute and solvent atoms have a 15 at% size mismatch (Hume-Rothery rule) [3.32], or 85% size ratio, which in fact agrees quite well with experiments for a large number of binary alloys [3.33].

Despite different routes taken in synthesizing amorphous alloys from crystalline solids, the basic principle remains more or less the same [1.2]. Most of these methods can be reduced to a simple solid solution model. For instance, hydriding of rare-earth intermetallics can be considered as a solid solution consisting of hydrogen located interstitially with the compound; a solid-state reaction produces a solid solution by interdiffusion at the interfacial layer of two pure metals; while mechanical attrition makes solid solution by forming defects and by interdiffusion between different constituents; and even irradiation induced amorphization can be regarded as producing a metastable solid solutions by disordering the ordered intermetallics. The essential point for all these processes is to make a metastable solid solution that has the same chemical composition as that of an amorphous phase. So the metastable solid solution model presented here can be expected to be a general model for the CGT.

The interatomic interaction used in this work is the Lennard-Jones (LJ) potential,

$$\phi_{\alpha\beta}(r_{ij}) = -4\epsilon_{\alpha\beta}\left[\left(\frac{\sigma_{\alpha\beta}}{r_{ij}}\right)^{12} - \left(\frac{\sigma_{\alpha\beta}}{r_{ij}}\right)^{6}\right], \tag{3.14}$$

where $\epsilon_{\alpha\beta}$ and $\sigma_{\alpha\beta}$ are parameters that are proportional to the potential depth and atomic radius of each interaction between two atoms. α and β denote two types of atoms, A and B.

The LJ potential is particularly suited to inert gas elements such as argon which have closed outer shells for their valence electrons. For metallic elements, and in particular, for transition metals, interatomic interactions are relatively complicated due to involvement of s, p and d electrons [3.34]. However, all interatomic potentials constructed so far have the same basic characteristics. They have the following features: a strong repulsive region close to the ion core and an attractive part at distances of a few nearest neighbor shells. The long-range behavior of a interatomic potential can vary due to many reasons. For example, Friedel oscillation [3.35] caused by incomplete electron screening of ion potentials can lead to a long-range oscillating tail. Details of these subtle features are fortunately less important for situations where collective effects of atoms in phase transitions are predominant. So the LJ potential is satisfactory for the purposes of investigation of thermodynamic and kinetic properties at the CGT. However, care has to be taken if local properties, such as short-range chemical ordering, phase separation and detailed atomic configurations of defects, must be considered. It is known, for instance, that the potential well depths of the LJ potentials (3.14), $\epsilon_{AA}, \epsilon_{AB}$ and ϵ_{BB}, can effect short-range ordering in binary liquid mixtures [3.36]. A strong attractive interaction between solvent A and solute B atoms will favor an arrangement of more B atoms surrounding A atoms. To avoid this undesirable situation in the binary LJ solid solution undergoing the CGT, we set all three parameters equal,

$$\epsilon_{AA} = \epsilon_{AB} = \epsilon_{BB} = \epsilon. \tag{3.15}$$

The case of using unsymmetric potential depths will be presented elsewhere for investigation of the possibility of dislocation pair unbinding mediated melting [1.9, 1.16]. A stronger solute-solute repulsion, or a shallow potential depth, ϵ_{BB}, will raise the barrier for dislocation clustering, thus forcing dislocations to unbind into singlets at melting.

In our simulation atomic size difference can be expressed conveniently by LJ parameters, σ_{AA} and σ_{BB}, as

$$\alpha = \frac{R_{BB}}{R_{BB}} = \frac{\sigma_{BB}}{\sigma_{AA}}, \tag{3.16}$$

where R_{AA} and R_{BB} are radii of atom A and B. At constant temperature and pressure, there are only two parameters required to characterize the binary alloy, the atomic size mismatch, $(1 - \alpha)$, and the solute concentration,

$$x_B = \frac{N_B}{N} = \frac{N_B}{N_A + N_B}, \tag{3.17}$$

where N_B, N_A and N are numbers of A and B atoms and the total number of atoms respectively. The only intrinsic defects are found to be those that are induced directly by atomic size mismatch.

In our simulation, solid solutions were generated by randomly dispersing small solute atoms on an fcc lattice which was originally occupied by large solvent atoms. The reason to do this is because disturbances caused by small atoms are relatively small, so one can have a large composition window to observe the transition.

Usually a simulation consists of two parts. The first part, usually $10^5 \sim 10^6$ time steps, was used for equilibrating the system. The second part, which usually lasts for $\sim 10^6$ time steps, was used to determine thermodynamic averages.

To quantitatively estimate the degree of supersaturation of the metastable solid solutions, one needs to know equilibrium solubilities. For the LJ binary system, the equilibrium phase diagrams crucially depend on the atomic size ratios [3.37]. In principle, equilibrium solubilities should be calculated from Gibbs free energies of two equilibrium phases at the given temperature using tangent rules. However, the required intensive computation prevents us from doing so in a limited time. Instead we used results of a binary hard sphere solid solution calculated from a density functional theory [3.37] to estimate the equilibrium solubility of the LJ binary solid solution having approximately the same atomic size ratio between solute and solvent atoms as that in the hard sphere model [3.37]. The equilibrium solubility of the hard sphere binary solid solution at roughly 50% of its melting temperature is less than 3 at.%. Considering the softness of the LJ potential (3.15), a larger equilibrium solubility for the LJ binary solid solution is expected, but no more than 5 at.%. On the other hand, most binary metallic solid solutions that have roughly the same atomic size ratio (for example, Fe-Be solid solutions), were shown to have equilibrium solubilities less than this value [3.32-33]. When solute concentrations go beyond equilibrium solubilities, the system is said to be supersaturated. The solution become thermodynamically metastable because its free energy is higher than that of the equilibrium phase(s) determined by tangent rule (see Fig. 3.2).

Fig. 3.3 shows a phase diagram of such a random LJ solid solution at constant T and P in a two-parameter space (α, x_B) for a fcc binary solid solution made of 500 atoms. In our simulation, it was found that above a critical atomic size ratio, α_c, the binary solid solution can be continuously saturated. Below this critical value, the solution ceases to exist at a maximum supersaturation, x_c, where the CGT occurs. Depending on the atomic size ratio, this critical, or maximum, metastable solubility can vary substantially. However, it is doubtful that a solid solution can still exist for very low atomic size ratios, since intermetallic compounds will likely prevail at such large size differences [3.33]. It is interesting to notice that critical atomic size ratios required to induce the CGT in a solid solution is very close to that required for forming the Laves phase [3.33]. In fact, the Laves phase has been found to be one of the most frequently observed competing phases in glass formation in the CGT [1.24].

To prevent diffusion from occurring, the temperature was set at 0.3 (in reduced LJ units) for all samples simulated. This is slightly below the glass transition temperature ($T_g = 0.4$), and roughly one half of the melting temperature ($T_m = 0.78$) of a pure LJ system. When the temperature is too low, it results in slow relaxation and thus longer simulation time.

At the temperature, and zero external pressure, the solid solution behaves differently in two regions separated by a critical value α_c, which is close to 0.83 for the given temperature, pressure and interatomic potentials (see Fig. 3.3). With smaller size mismatch, it forms a continuous metastable solid solution with almost perfect cubic symmetry, but in a narrow region close to α_c the solution becomes distorted from cubic to tetragonal. Such a structural change could be caused by large shear strain fluctuations. However, a possibility of an artifact caused by small sample size cannot be ruled out either. Further tests with different sample size are

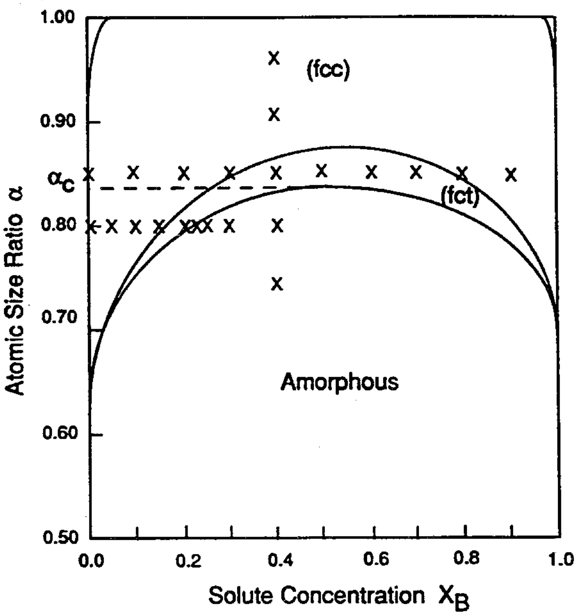

Fig. 3.3 Schematic metastable phase digram of LJ binary solid solution in parameter space (α, x) at constant pressure temperature (T=0.3) and pressure (P=0.0). The total number of atoms is 500. The LJ potential cutoff distance is 2.45σ. × marks the phase calculated using molecular dynamics. The areas at the two upper corners are the equilibrium terminal solid solution.

needed. In the following we shall focus on another region of the phase diagram which corresponds to larger atomic size mismatch ($< \alpha_c$). The CGT always occurs at a finite supersaturation x_c in this region.

The radial distributions functions (RDF) (Fig. 3.4) show systematic changes of the structure of the solid solution with $\alpha = 0.80$, as more solute atoms are added. The first and second nearest neighbor coordination numbers for various pairs (e.g., AA, AB and BB) which are proportional to the areas under the peaks in the RDF's, have the same mean density as the overall solute composition. Thus no local chemical ordering has developed. Broadening of all the peaks of various coordination shells for the pure LJ crystal ($x_B = 0$) is due entirely to thermal vibrations of atoms at this temperature. Additional broadening of these peaks and their decreasing intensities at nonzero solute concentrations ($\mathrm{x}_B > 0$) are attributed to disordering induced by solute atoms. The same behavior can be observed for partial RDF's for AA, AB and BB atoms, but the broadening is more spread out and the intensities are much lower.

Below the critical size ratio, a quantitatively different RDF starts emerging at approximately a 20% solute concentration. Peaks corresponding to the second, fourth and fifth, etc. nearest neighbors disappear and two broad humps develop at distances beyond the nearest neighbor peaks. More striking is the split second peak, in particular, of the partial RDF's. Such a split peak is commonly observed in most metallic amorphous phases.

The structural changes can also be revealed in more detail by examing the local translational order parameter defined in (2.23) with a slight modification,

$$\rho_G = \frac{1}{N}\sum_{i=1}^{N} exp(-i\mathbf{G}\cdot\mathbf{r}_i), \tag{3.18}$$

where the shortest reciprocal lattice vector along [111] direction, which corresponds to the densest packed atomic planes, is chosen for **G**. Fig. 3.5 shows the translational parameter defined above as a function of solute concentration. It shows that the change in the translational symmetry is discontinuous; from $x_B = 0.20$ to $x_B = 0.225$ ρ_G drops abruptly from 0.82 to 0.12.

Accompanying with the structural change are structural fluctuations which are represented by the MD cell parameter,

$$< (\delta h)^2 > = < h^2 > - < h >^2 . \tag{3.19}$$

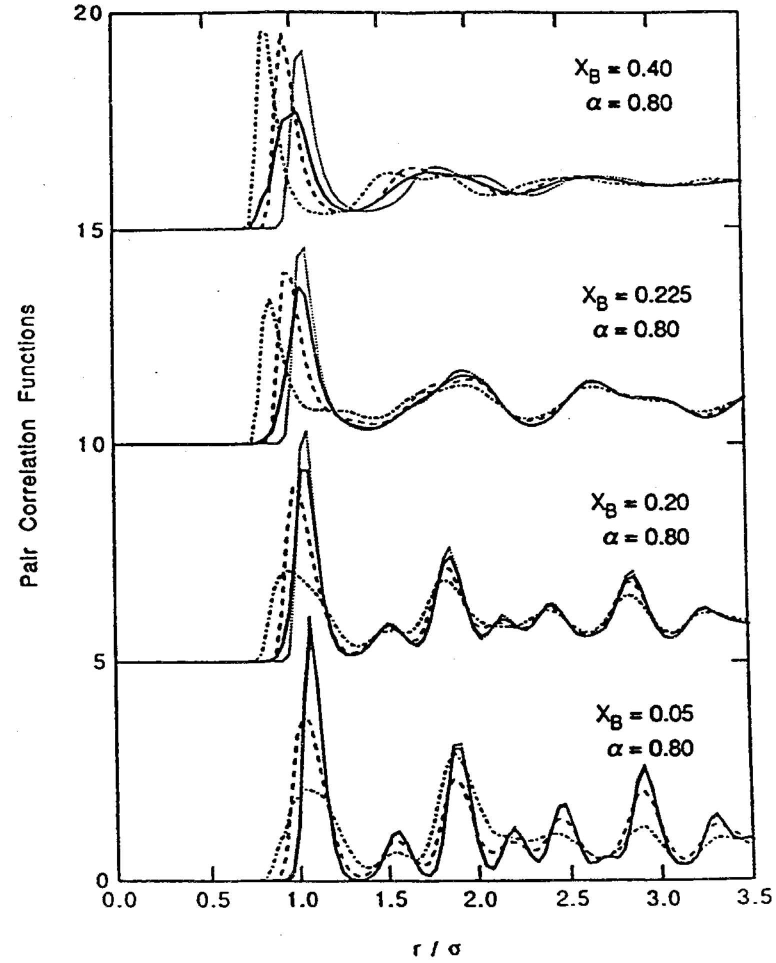

Fig. 3.4 Partial and the total pair correlation functions of the fcc LJ binary solid solutions at different supersaturations at temperature $T = 0.3$ and pressure $P = 0.0$. The atomic size ratio between solute and solvent is 0.80, which is slightly below the critical ratio ($\alpha_c = 0.83$). Solid line is for the total RDF; dashed line for partial RDF of AB atoms; dotted line for partial RDF of AA atoms; dot-dashed line for partial RDF of BB atoms. Distance is normalized by the LJ parameter σ.

This quantity is directly related to strain fluctuations through the following relation,

$$\delta\epsilon = \frac{1}{2} h_0^{-t} \delta G h_0^{-1}, \tag{3.20}$$

which in turn is related to elastic constants defined by equation (2.18). The strain fluctuations can be seen more clearly in elastic constants in the principal strain coordinate. Fig 3.6 shows the three independent isothermal elastic constants. Here $(C_{11} + C_{12})/3$ is the bulk modulus, and $C' = (C_{11} - C_{12})/2$ is the tetragonal shear elastic modulus which represents responses of deformation along the [001] direction. C_{44} is a rhombohedral shear modulus corresponding to strain along the [111] direction. From the figures one can see that the largest structural fluctuation is along the [001] directions as the system gets close to the CGT. In fact, the tetragonal shear elastic constant shows an extremely large precursor effect even far away from the CGT. Experimentally measured elastic constants usually show a linear decrease with increasing temperature, or with volume expansion in ordinary melting. The softest elastic constant are different for different systems, but the most frequently observed one is tetragonal shear elastic constant [3.10-11] in crystals with cubic Bravis lattice. In our case, C_{44} appears "lagging behind" showing a linear decay with increase of solute concentration at low solute concentrations. Very close to the CGT, it decreases abruptly. Structural fluctuations are large on the metastable crystal side, but become stabilized on the amorphous side. The two shear elastic constants approach the same value as the solid becomes an isotropic glass. A continuously decreasing C' and its extremely small value close to the CGT suggest that the CGT in the solid solution is closely related to the (elastic) lattice (shear) instability and the transition proceeds in a manner similar to a continuous phase transition. Although our work has provided much more detailed information, unfortunately the

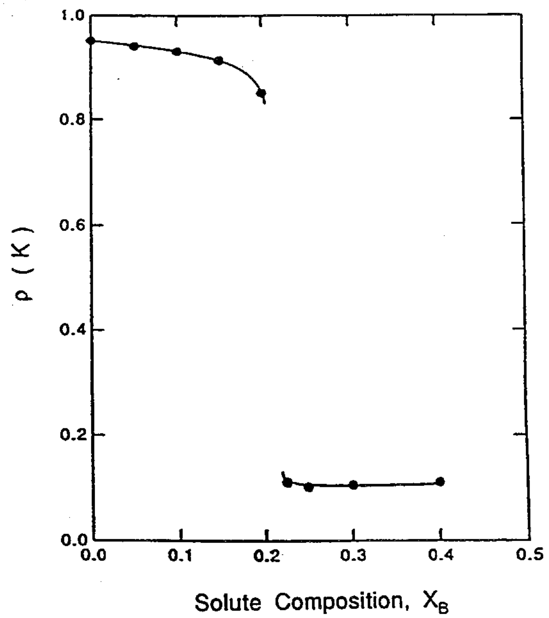

Fig. 3.5 Translational order parameter (Bragg peak intensity) along **G** = [111] direction for the binary LJ solid solution as a function of solute composition at $T = 0.3$ and $P = 0.0$. The atomic size ratio is 0.80. The solid lines are drawn to guide eyes.

crucial part of it has not been available at the CGT, due to the finite size/time used in the simulation. At solute concentrations very close to the CGT, large structural fluctuations prohibit us to get a convergent C' and C_{44}.

Our results presented above can be summarized briefly as follows. First, the structural transition from crystalline to amorphous is through *shear*, although what structural unit is involved is not clear yet; and the different behavior of C' and C_{44} suggest that tetragonal shearing is predominant. Second, shearing can occur on different scales, as suggested by increasing lattice distortions of the system as a whole along the [001] direction as solute concentration increases and formation of small patches of crystalline clusters with each one deformed along a different variant close to the CGT (also see chapter 5 for details). Third, the continuous and significant softening of C' indicate a gradually growing correlation between "frozen-in" strains, as predicted by the basic fluctuation-response theory (chapter 4 for details), which is in contrast to that of a typical first-order transition.

The above observations are in fact consistent with other thermodynamic properties we obtained from simulations. Fig. 3.7 is molar enthalpy and molar volume of the binary solid solution versus concentration. The molar volume (its inverse is density) decreases linearly at dilute concentrations (Vegar's law), but a slight change of curvature close to the CGT can be seen. The same is true for the molar volume of the amorphous phase. There is a small jump of volume at the CGT from the crystalline phase to the amorphous phase, but the magnitude is very small ($< 1\%$). The molar enthalpy also increases linearly at the dilute limit and then bends down slightly when it gets closer to the CGT. On the amorphous side it appears to be saturated: further increase of the solute concentration leads to only a slight change.

It is difficult to obtain thermodynamic properties right at the CGT boundary, especially the Gibbs free energy and entropies. But we can use the available results to estimate those quantities close to the CGT. The entropy change of a binary solid solution under constant pressure can be expressed in general as

$$\begin{aligned}\Delta S &= \left(\frac{\partial S}{\partial T}\right)_V \Delta T + \left(\frac{\partial S}{\partial V}\right)_T \Delta V + \sum_{i=A,B} \left(\frac{\partial S}{\partial x_i}\right)_{v,T} \Delta x_i \\ &= \frac{C_V}{T}\Delta T + \frac{\alpha}{\kappa_T}\Delta V - \sum_{i=A,B} \left(\frac{\partial \mu}{\partial T}\right)_{V,T} \Delta x_i, \end{aligned} \tag{3.21}$$

where C_V, α, κ_T and μ are constant volume molar heat capacity, isothermal volume expansion and compressibility and chemical potential respectively. At constant

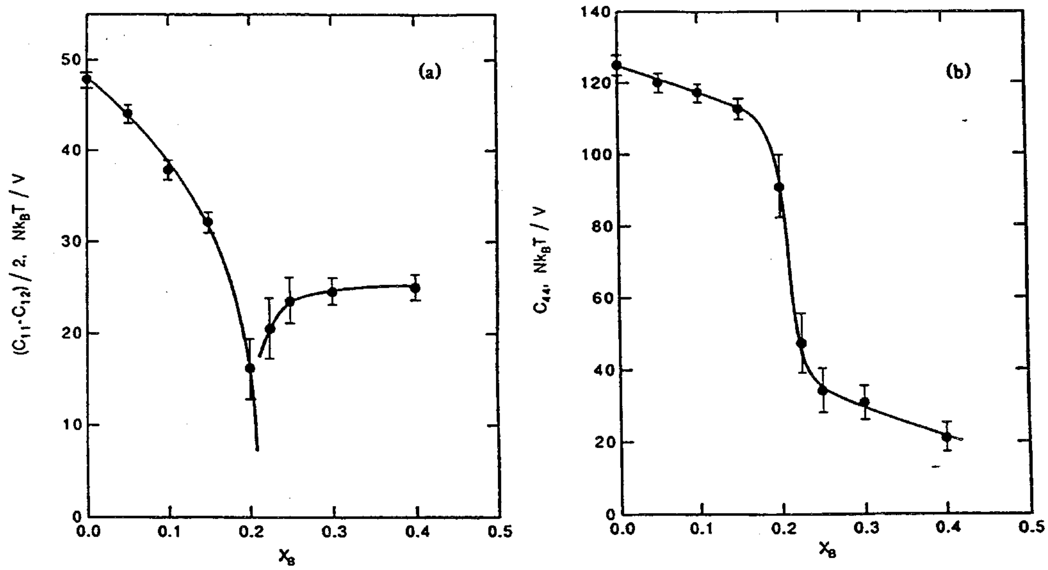

Fig. 3.6 (a) Isothermal tetragonal shear elastic constant, C'; (b) rhombohedral shear elastic constant, C_{44}, of the LJ binary solid solution with atomic size ratio 0.80, at temperature $T = 0.30$ and pressure $P = 0.0$. Note the large fluctuations close to the CGT.

temperature (Δ T = 0) and under polymorphic constraint ($\Delta x_B = 0$), the entropy change is related to volume change only,

$$\Delta S = \frac{\alpha}{\kappa_T} \Delta V. \tag{3.22}$$

The molar volume change at the CGT is less than 1% from the crystalline solid solution to the amorphous phase. Such a small volume change can be anticipated from the behavior of the shear moduli and the small change of the bulk modulus. Shear deformation preserves volume and thus is easy to achieve. The coefficient in (3.22), the ratio between isothermal volume expansion and compressibility at the CGT, is on the order of ~ 10 in both three- and two-dimensional systems. Thus

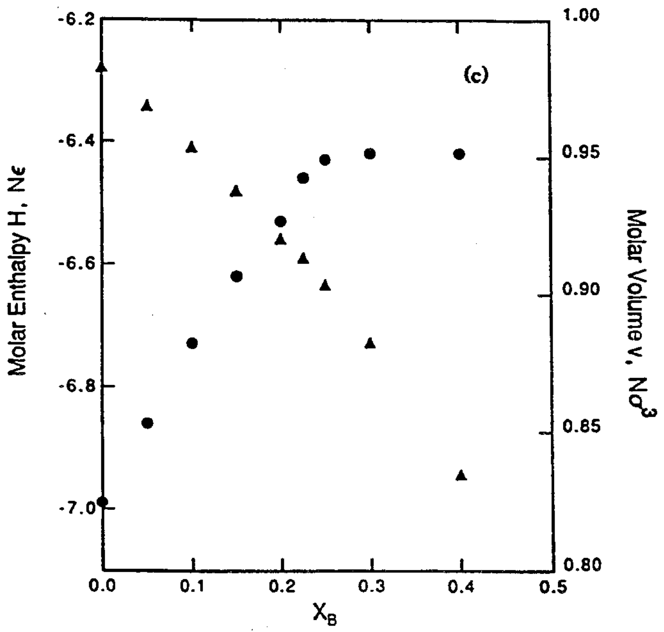

Fig. 3.7 Molar enthalpy (•) and molar volume (△) of LJ binary solid solution with atomic size ratio 0.80, at temperature $T = 0.30$ and pressure $P = 0.0$.

the change of the entropy is approximately 0.15 ~ 0.20 $\mathrm{Nk_B}$. As such, we set the entropy change equal to zero,

$$\Delta S \approx 0, \tag{3.23}$$

at the CGT. This result, combined with enthalpy change ($\Delta \mathrm{H} \approx 0$) at the CGT leads to an expected result for Gibbs free energy at the transition,

$$\Delta G = \Delta H + T\Delta S \approx \Delta H \approx 0. \tag{3.24}$$

In a binary system, the free energy is a function of composition and temperature only, G (x, T). At a given temperature, (3.24) defines phase boundaries of the polymorphic transition, or $T_0(x)$ line. From the above results, one can see that the crystal to glass transition under polymorphic conditions could have *no latent heat* and *no abrupt density change.* This is in sharp contrast to ordinary melting where a latent heat and volume change are observed. For example, for pure metals, ΔS is roughly a constant $\simeq \mathrm{Nk_B} = \mathrm{R}$ (8.14 J $\mathrm{mol^{-1}\ K^{-1}}$, Richard rule), and the density change is $\sim$ 5% [3.38].

3.5 Comparison With Experiments

It is clear from the MD simulations that the CGT is indeed a phase transition (albeit from one metastable phase to another) and is well defined by all the thermodynamic properties ($\Delta G = 0$). With dramatic softening of shear elastic constants and extremely small changes of density, enthalpy and entropy cross the $\mathrm{T_0}$ line, the crystalline phase is apparently approaching a stability limit set by a diminishing "restoring force" to retain crystallinity. The large precursor effect of the shear elastic moduli indicates that such the transition occurs not in an abrupt but rather a gradual and continuous manner. However, none of these results has been observed unambiguously and consistently in experiments so far. Some recent experiments nevertheless have demonstrated some interesting features resembling those presented in this work [3.39-40]. In the following, we will compare these results with ours.

Okamoto, et al. performed an experiment using Brillouin scattering to measure shear sound velocity of a polycrystalline intermetallics $\mathrm{Zr_3Al}$ irradiated with 1Mev $\mathrm{Kr^+}$ [3.39]. In this experiment they found that transverse sound velocity decreases with increasing radiation dose, or displacement per atom (dpa), in a similar fashion as that calculated by MD simulations (see Fig. 3.8). At the onset of the transition, the shear sound velocity plunged almost 50% from that of the initial ordered crystalline sample. As the dpa increases further past the transition, the

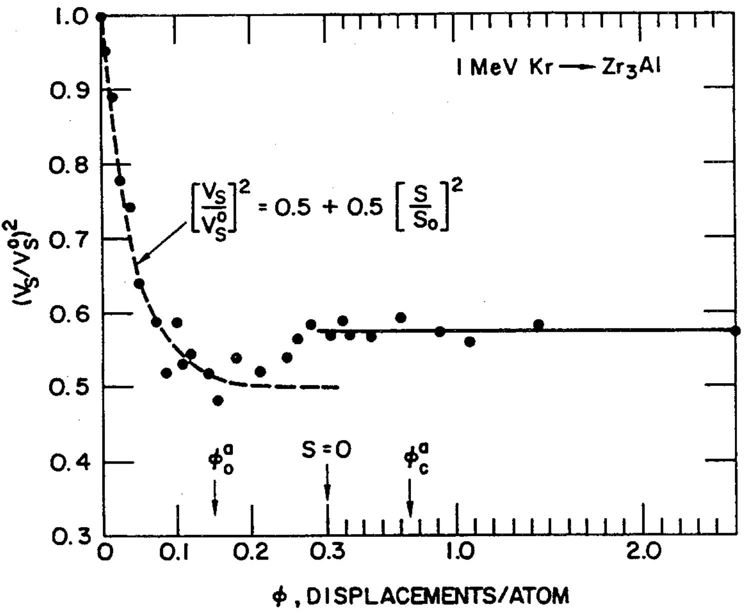

Fig. 3.8 Measured transverse sound velocity (V_s/V_s^0, normalized by the shear sound velocity of an unirradiated sample) *vs.* displacement per atom for an irradiated Zr_3Al. The ratio is proportional to that of shear elastic constants. S is the long-range order parameter. ϕ_0^a and ϕ_c^a denote dpa at the onset and completion of amorphization. Note the large fluctuations in the data close to ϕ_0^a.

shear velocity starts leveling off. Note that the CGT occurs in an very wide range of radiation dose (0.1 ~ 0.3), and large errors in the measurements also occur in this range.

In the same system, chemical disordering which is represented by the long-range order parameter S, obtained from electron diffractions from the irradiated samples, shows a dramatic decrease in the long range chemical order. This implies that the compound is severely disordered chemically and formed a random solid solution, along with topological disordering that occurs either simultaneously or subsequently.

Another experiment was done by Ettl et al. [3.40] on $Zr_{1-x}Al_x$ solid solutions prepared by mechanical alloying of Zr and Al. Because the solute concentration is increased gradually, their results offer a direct comparison with ours. In their experiments, effective elastic constants M were obtained from low temperature ($1.5 \sim 9.0K$) calorimetry measurements of Debye temperature. Debye temperature is related to M by the following equation [1.2],

$$M = (k_B \Theta_D / \hbar q_D)^2 \rho, \tag{3.25}$$

where Θ_D and q_D are Debye temperature and wave vector, both of which can be directly obtained from heat capacity. The shear modulus μ is obtained from the following equation, assuming a slow variation of the bulk modulus K with changing composition,

$$M = const(B^{-3/2} + \mu^{-3/2})^{2/3}. \tag{3.26}$$

Fig. 3.6 shows their measured shear elastic constants of the mechanically supersaturated Zr-base solid solution as a function of solute concentration (room temperature equilibrium solubility of Al in Zr is < 1.0 at.%). Softening of elastic shear modulus can be clearly seen. The deepest cusp also occurs at a composition that corresponds to the onset of the CGT.

It should be pointed out that there are certain differences in the systems used in the experiments and ours. The samples used in the experiments are polycrystalline and also have different structures. The $Zr_{1-x}Al_x$ solid solution has a closed packed hexagonal structure and the intermetallics Zr_3Al has a $L1_2$ structure with

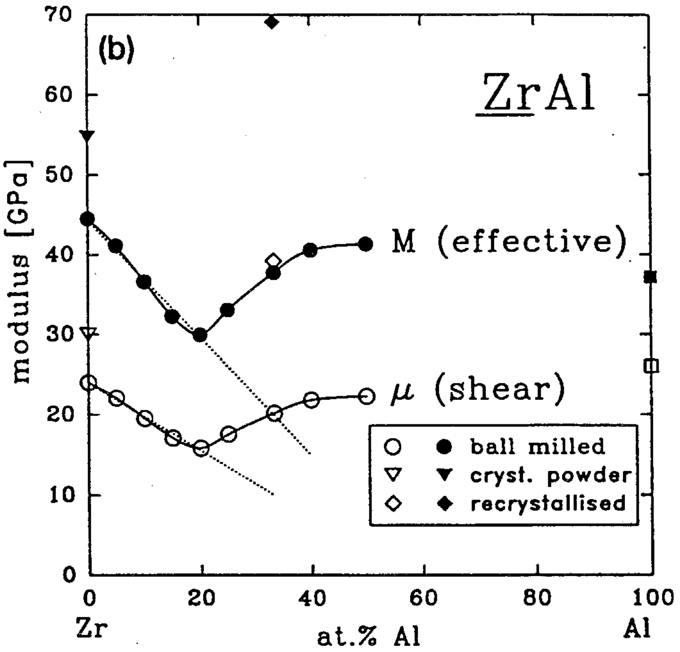

Fig. 3.9 Measured effective elastic modulus, $M(\bullet)$, and shear modolus, $\mu(\circ)$ of ZrAl solid solution *vs.* Al composition. M and μ are obtained from eqs. (3.25) and (3.26). For experimental details, see Ref. [3.40].

Zr atoms sitting on face center positions and Al on corners of an fcc lattice. The experiments actually measured average shear elastic constants. In the case of the $Zr_{1-x}Al_x$ solid solution, there are a total of 5 independent elastic constants and four of them are shear elastic constants; in the irradiated Zr_3Al, there are two shear moduli. These experiments, therefore, were unable to identify the softest shear mode(s) that is primarily responsible for lattice instability. However, the behavior of the shear elastic constants as demonstrated, is quite encouraging.

References

3.1 O. Penrose and J. L. Lebowitz, *Fluctuation Phenomena*, edited by E. W. Montroll and L. J. Lebowitz, Chapter 5, (North Holland, Amsterdam, 1979)

3.2 J. P. Hirth and J. Lothe, *Theory of Dislocations*, 2nd edition, (John Wiley & Sons, New York, 1982).

3.3 R. W. Cahn and W. L. Johnson, J. Mater. Res., **1**, 724, (1986).

3.4 *Phase Transitions During Irradiation*, edited by F.V. Nolfi (Applied Science, Egglewood, NJ, 1983).

3.5 P. R. Okamoto and M. Meshii, *Science of Advanced Materials*, pp 33, (ASM International, Materials Park, OH, 1990).

3.6 H. B. Callen, *Thermodynamics and an Introduction to Thermostatics*, 2nd Ed., pp. 203-214, (John Willey & Sons, New York, 1985).

3.7 H. E. Stanley, *Introduction to Phase Transitions and Critical Phenomena*, (Oxford University Press, Oxford, 1971).

3.8 L. D. Landau and E. M. Lifshitz, *Statistical Physics*, 2nd Edition, (Pergamon Press, Oxford, 1980).

3.9 M. Born, J.Chem. Phys., **7**, 591, (1939).

3.10 J. L. Tallon, Phil. Mag., **39 A**, 151, (1979).

3.11 J. L. Tallon, Phil. Mag., **39 A**, 151, (1979); J. L. Tallon and W. H. Robinson, Phil. Mag., **36**, 741 (1977); J. L. Tallon, Nature, **342**, 658, (1989).

3.12 R. Zallen, *The Physics of Amorphous Solids* (John & Willey, New York, 1983).

3.13 J. Wang, S. Yip, S. Phillpot and D. Wolf, J. Alloys and Compounds, **194**, 407 (1993).

3.14 F. A. Lindemann, Z. Phys., **11**, 609, (1910).

3.15 R. Devantahan, N. Q. Lam, P. R. Okamoto and M. Meshii, MRS Symposia Proceeding No. *291*, pp. 653, (MRS, Pittsburgh, 1993).

3.16 J. Koike, Phys. Rev. B, **47**, 7700, (1993).

3.17 C. E. Krill III, J. Li, C. Ettl, K. Samwer, W. B. Yellon and W. L. Johnson, J. Noncrystal. Solids, **156-158**, 506, (1993).

3.18 J. A. Reissland, *The Physics of Phonons* (John Willey & Sons, London, 1973).

3.19 T. Egami and D. Srolovitz, J. Phys. F **12**, 2141, (1982); T. Egami and V. Vitek, Amorphous Materials: Models of Structure and Properties, edited by V. Vitek, (TMS-AIME, Warrendale, PA, 1983), pp 127.

3.20 T. Egami, V. Vitek and S. P.Chen, Phys. Rev. B, **37**, 2440, (1988); S. P. Chen, T. Egami and V. Vitek, J. Noncrystal. Solids, **75**, 449, (1988).

3.21 D. Kulp, T, Egami and V. Vitek, J. Noncrystalline Solids, **156**, 510, (1993).

3.22 W. Kauzmann, Chem. Rev., **43**, 219, (1948).

3.23 H. J. Fecht and W. L. Johnson, Nature, **334**, 50, (1988).

3.24 X. L. Yeh, K. Samwer and W. L. Johnson, Appl. Phys. Lett., **42**, 242 (1983).

3.25 W. J. Meng, J. Faber, P. R. Okamoto, L. E. Rhen, B. J. Kestel and R. L. Hitterman, J. Appl. Phys., **67**, 1312, (1990).

3.26 H. J. Fecht, Z. Fu and W. L. Johnson, Phys. Rev. Lett., **64**, 1753, (1990).

3.27 C. E. Krill, J. Li, W. B. Yellon and W. L. Johnson, Phys. Rev. B, **48**, 3689, (1993).

3.28 W. L. Johnson, C. C. Tsuei, S. I. Raider and R. B. Laibowitz, J. Appl. Phys., **50**, 4240 (1979).

3.29 B. C. Giessen, *Proc. 4th Int. Conf. on Rapidly Quenched Metals*, edited by T. Masumoto and K. Suzuki, (Japan Institute of Metals, Sendai, 1982), **1**, pp.

213.

3.30 F. Sommer, M. Fripan and B. Predel, *Proc. 4th Int. Conf. on Rapidly Quenched Metals*, edited by T. Masumoto and K. Suzuki, (Japan Institute of Metals, Sendai, 1982), **1**, pp. 209.

3.31 T. Egami and Y. Waseda, J. Noncrystal. Solids, **64**, b113, (1984).

3.32 W. Hume-Rothery and G. V. Raynor, *The Structure of Metals and Alloys*, (The Institute of Metals, London, 1954).

3.33 J. W. Christian, *The Theory of Transformations in Metals and Alloys*, 2nd edition, (Pergamon Press, Oxford, 1985)

3.34 W. A. Harrison, *Electronic Structure and the Properties of Solids*, (Freeman, San Francisco, 1980).

3.35 J. A. Alonso, and N. H. March, *Electrons in Metals and Alloys*, (Academic Press, London, 1989).

3.36 R. D. Mountain, Mol. Phys., **59**, 857 (1986); K. Nakanishi, H. Narusawa and K. Toukubo, J. Chem. Phys., **72**, 3089 (1980).

3.37 A. R. Denton, and N. W. Ashcroft, Phys. Rev. B, **43**, 3161 (1991) and references therein.

3.38 A. R. Ubbelohde, *Melting and Crystal Structure*, (Clarendon Press, Oxford, 1965).

3.39 P. R. Okamoto, L. E. Rehn, J. Pearson, R. Bhadra, and M. Grimsditch, J. Less-Common Metals, **140)**, 231, (1988).

3.40 C. Ettl, and K. Samwer, J. Noncrystal. Solids, **156**, 502, (1993).

Chapter 4

Landau Theory of Crystal to Glass Transition

4.1 Introduction

The central question we intend to address in this chapter is whether a normal first-order phase transition, such as polymorphic melting, could become continuous, and under what circumstances does the crossover become possible. Sharp, divergent properties such as heat capacity in a continuous phase transition can be smeared out if growth of the coherence length is blocked by frozen-in impurities [4.1]. This problem has not received much attention for first-order transitions, although a few attempts have been made [4.2]. The reason is related to the nonuniversal properties exhibited at first-order transitions where scaling relations in general are not applicable. Impurities and finite size effects would not have any substantial effects on the correlation length at a first-order transition that is intrinsically finite, thus making this problem less attractive. Nevertheless, rounding or smearing out of the transition can occur in metastable systems that otherwise undergo a first-order transition. The underlying mechanism, however, is not related to "blocking" of the correlation lengths, as in the case of a continuous transition, instead it is due to the altered behavior of order parameters under constraints imposed by slow kinetics. So the abrupt change of thermodynamic properties usually seen at a first-order transition can be smeared out. If such effects become large, a first-order transition can lose its characteristics and appear continuous [4.2]. In this chapter, we shall explore this possibility in the CGT using a phenomenological Landau theory.

In the next section, we will discuss experimental limitations and restrictions on investigation of the nature of the CGT in general. We will use a diffusion couple as an example. In section 4.3 we will discuss how to chose order parameters for a Landau theory that describes a metastable crystalline solid to glass transition. The role of random, "frozen-in" stress and strain will be emphasized. We will present a simple Landau theory for the polymorphic melting in section 4.4 and subsequently discuss the possibility of crossover from a first-order polymorphic melting transition to a continuous one and necessary conditions needed to do so. Since the Landau theory is a phenomenological approach, without losing generality, certain assumptions are made in order to proceed with analysis. However, these restrictions can be easily removed, so the result obtained from this theory is general.

4.2 Could the CGT be Continuous?

The CGT observed experimentally can be characterized as *kinetically controlled*, because large chemical inhomogeneities, finite size confinement and extrinsic defects are always present in samples used for experimental measurements. In this section, we shall take the solid-state reaction induced amorphization in an interdiffusion couple as an example to demonstrate this.

Fig. 4.1 is a typical setup of a diffusion couple used for solid state reactions (SSR). Two pieces of pure metals are placed in close contact, either by thin film growth techniques [1.13, 4.3] or mechanical adhesion [4.4]. At room temperature or elevated temperature, a layer of amorphous phase forms in between. Accompanying the growth of the amorphous layer usually is a gradual formation of voids and ultimately some stable intermetallics along the interfaces adjacent to the amorphous layer. It has been found that such properties as the *heat of mixing* of solid solution and amorphous phases, *asymmetric diffusivity* of one of the elements and *crystalline* *defects* are crucial factors to the formation of the amorphous phase [1.2].

The artificial constraint on chemical composition and geometry confines the transition to a narrow region of an interface. The low ambient temperature imposed in order to prevent long-range diffusion (to avoid stable phase formation), will further obscure the transition. Next we will examine the effects from *geometrical confinement, chemical inhomogeneity* and *defects* on the CGT separately.

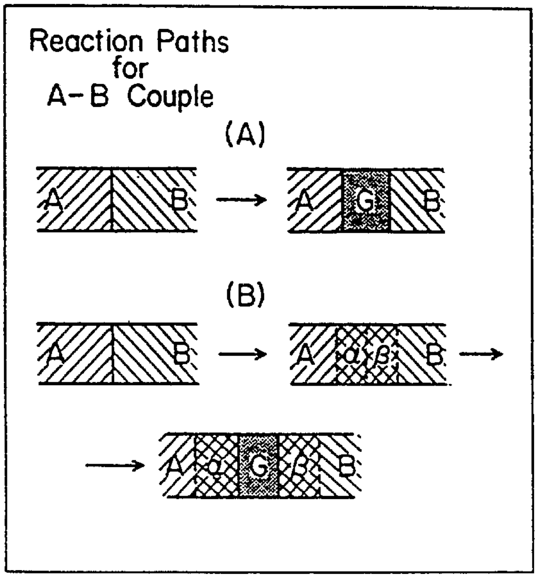

Fig. 4.1 Illustration of two alternative solid state reaction sequences which lead to glass interlayer growth. Case A corresponds to direct formation of amorphous phase at the original interface. Case B corresponds to substantial mutual dissolution of the parent metals and formation of amorphous phase at the interface between two solid solutions (from Ref. 1.2).

A. Finite size

A continuous phase transition differs from a first-order one essentially in the fact that the systems undergoing these transitions have totally different behavior in terms of their correlation functions of order parameters, or collective behavior of atoms, at the transitions. A phase undergoing a continuous transition has a diverging correlation length and large fluctuations of thermodynamic properties associated with it, whereas a first-order transition has only a finite correlation length and finite response. But if a transforming system is constrained to be a "finite size" as in the diffusion couple, the correlation as well as response will be limited, thus making it impossible to tell the difference between an intrinsic continuous transition and a first-order one.

B. Chemical Inhomogeneity

In a solid solution, the instability happens only when the two elements mixes in a critical proportion, $x \geq x_c$ and $\alpha \leq \alpha_c$. However, in the diffusion couple, there is a huge initial composition difference cross the interface between two elements that restricts solute composition to reach required "supersaturation" x_c, in order to initiate the instability. Low temperature will further worsen the situation by limiting diffusions during subsequent formation of new amorphous phase. The critical condition (x_c, α_c) to form a homogeneous amorphous phase from a metastable crystalline solid is met only at a very narrow region along the interface. The macroscopic chemical inhomogeneity is strongly maintained by kinetic constraints on diffusion throughout the entire process of the amorphization reaction.

If the enthalpy of mixing of the two elements is negative for forming a solid solution, such mixing will occur naturally. Atoms could diffuse across the interface and mix into a solid solution. But the large composition gradient can jeopardize the metastability by forming more stable intermetallic compounds if both types of atoms diffuse equally quickly under the large driving force. In order to form metastable solid solution with *supersaturation*, one atom, often the small atom, can diffuse. Thus the required critical composition can be reached by "saturating" the small atom in the matrix of the larger atoms. This has in fact been observed in many diffusion couples formed by early-late transition metals such as Ni-Zr [1.2]. But the formation of the amorphous phase by the collapse of crystalline lattice is still restricted subsequently on further diffusion to reach the critical condition in order to propagate the amorphous front.

If the enthalpy of mixing for forming the solid solution is positive, the instability can occur only in a very narrow region at the crystal/crystal interface and the amorphous layer so formed must propagate subsequently with greater difficulty caused by the absence of diffusion.

C. Defects

In addition to the finite size and chemical effects discussed above, structural imperfections can also influence the CGT critically. Crystalline defects can function as special sites for transporting atoms to satisfy the instability condition (x_c, α_c) along the crystal/crystal interface to initiate the transition, or at the amorphous/crystal front for subsequent growth. In addition, they act directly as nucleation sites for the topological order to disorder transition. Such extrinsic defects can induce the CGT locally and inhomogeneously. Indeed, it was found that no solid state amorphization occurred in a Ni-Zr diffusion couple formed on a single crystal Zr substrate with an atomically smooth interface [4.5].

Despite the difficulties, recent experiments have provided some interesting results that lead to certain characteristics of a possible continuous CGT. It was found that the energy barrier to start the amorphous layer at the interface in certain diffusion couples appeared to be very small in the early stage amorphization [1.2], which indicates a small nucleation barrier for the formation of the amorphous phase [4.6]. And if the layer thickness of pure metals in multilayers is reduced to critical values ranging from 10 to 20 Å, amorphization appears to occur almost spontaneously [4.7]. However, these results are far from conclusive because the scale on which these observations were made are close to the limit of experimental resolution.

Direct observation of the formation of a homogeneous amorphous phase was reported during the process of hydrogen absorption induced amorphization [4.8]. This should be anticipated based on the fact that hydrogen diffuses fast enough to nullify the kinetic constraint to reach the condition (x_c, α_c) to initiate a new amorphous phase and for subsequent growth. However, the presence of crystalline defects, mainly grain boundaries in the polycrystalline sample, leads to a competing mode of amorphization. Thus heterogeneous nucleation of amorphous phases at these defects still prevails [4.8].

4.3 Order Parameters for Landau Theory

As we mentioned earlier, if an homogeneous metastable crystalline phase transforms polymorphically to an homogeneous amorphous phase, phase equilibrium conditions applied to equilibrium phases are also applicable to the metastable phase transition. However, if the free energy versus temperature and composition behaves as depicted in Fig. 3.2 (a) for a binary solid solution, the CGT would occur discontinuously. Across the locus $(T_0(x) = 0)$ where

$$\Delta G(T_0, x) = 0, \tag{4.1}$$

the derivatives of the free energy with respect to composition, *the chemical potentials of the crystalline and amorphous phase are different at this point*, that is,

$$\mu_A^{\text{crystal}}(T_0, x) \neq \mu_A^{\text{amorphous}}(T_0, x) \tag{4.2}$$

and

$$\mu_B^{\text{crystal}}(T_0, x) \neq \mu_B^{\text{amorphous}}(T_0, x). \tag{4.3}$$

This becomes the driving force for atomic diffusion. So the equilibrium phase would be a mixture of both crystalline and amorphous phases or other equilibrium intermetallics (γ). However, the kinetic constraint will restrict such mass transportation from occurring at low temperature. So the thermodynamic functions in the metastable system will be expressed as functions of relevant thermodynamic variables under *constant chemical potential differences.* This difference is called chemical potential affinity [4.9]. So the chemical potential is no longer a thermodynamic variable to satisfy the equality in Eqs. (4.2) and (4.3) at the transition, rather a constraint that restricts the system in a particular portion of the phase space.

One of the profound consequencies of this kinetic constraint is to cause local atomic displacements, or local arrangements and the formation of defects; and most importantly, to retain, or freeze the atomic configurations. As we discussed earlier, the nonhomogeneous, random stain field associated with these defects, topological and nontopological, is retained too. It is this "frozen-in" displacement and strain field that can give rise to the excessive free energy for the system to transform to the amorphous phase. If the kinetic constraint weakens, such as by increasing temperature, the defects begin to move to lower the energy. These defects can coalesce, cluster or even be annihilated. The strain field therefore becomes weak and less influential. In fact, it is this property that makes melting first-order and the CGT either first-order or continuous depending on system's temperature.

The long wavelength, random, and "frozen-in" strain not only gives rise to elastic energy in the system, but can also affect the atomic displacements. These two effects are crucial for the CGT and thus will be taken into account explicitly (see next two sections). The effects, or the static, random strain on the metastable system and the CGT vary depending on the solute concentration, atomic size ratio and temperature. The strain-strain correlation function can provide both the strength and correlation length of the static, random strain field. By examining the variation of elastic constants and symmetry order correlation functions (see next chapter), one determine the effects. For instance, at the critical supersaturation, x_c, α_c, the static, random strain become strongly correlated, which leads to vanishing elastic constants. So atomic displacements at this critical point are completely dominated by the strain fluctuations in the system that has no elastic rigidity, thus the CGT occurs spontaneously.

As we discussed in section 3.3, the atomic displacement, $D(\mathbf{r})$, represents topological disordering and is a natural *order parameter* to represent the states of the system and thus to describe the transition. But a distinction has to be made for cases of melting and the CGT. We shall come to this point later. The atomic displacement which includes dynamic and static contributions, is analogous to spin vectors in magnetic phase transition, except that it is a vector with a *variable length.* Lindemann's criterion [3.14] is then a simple statement that at a first-order melting transition, the mean order parameter has a finite jump.

To summarize, the relaxation of microscopic stress resulted from unfavorable atomic configuration of two mismatched atoms leads to random, local, static atomic displacement, which is a natural order parameter to describe the topological order to disorder transition. The static, random strain, which results from the presence of "frozen-in" defects is then the secondary order parameter for the transition.

Now we return to answer the question of why this choice for order parameters does not suit melting. As we stressed above, the *static* nature of the local, random, microscopic displacement and strain is an essential criterion for determining the validity of using these order parameters. The atomic displacement becomes meaningless at sufficiently high temperature when diffusion starts. Thus one cannot use it as an order parameter to describe a phase transition where both phases have to be considered. However, this limitation is no longer applied if diffusion is absent, which is precisely the situation corresponding to polymorphic melting. Therefore, strictly speaking, the order parameter approach is only valid when there is no diffusion, or under constant chemical affinity.

The assumption made for an order parameter approach will break down when diffusion starts, or the chemical affinity changes. Fast relaxation, represented by long-range diffusion, can make the local variations of of the atomic displacement and strain field quickly spread out or smooth out. Except for spontaneous, homogeneous, dynamic atomic displacements and strain, there is essentially no local, random, static displacements and strain fields in a hot crystal or a liquid. In fact, this result has been known ever since molecular dynamics was invented [4.10]. The displacement field fluctuates with frequencies typical of several hundred femto seconds [4.11], which implies that the strain field is also dynamic in nature. For this reason, we can conclude that the static atomic displacement and strain field can not be used as an order parameter for thermal melting.

It is interesting to point out, based on the above argument, that the glass formed by rapid quenching from a liquid will not have a strong strain field, instead it will be stressed, if cooling rate is faster than the stress relaxation time. Such a result could have some profound consequencies on mechanical and transport properties of metallic glasses [4.12-13].

4.4 Landau Theory of the CGT

In the following, we shall present a simple phenomenological model, a Landau theory to describe the CGT using the order parameters discussed above. Before we proceed with the theory, we should like to make the following assumptions.

First, the primary order parameter used in this model to describe the first-order transition is the atomic displacements, $\mathbf{D}(\mathbf{r})$. This choice of order parameter is a natural one to describe the CGT. For convenience, we will use the mean square atomic displacements (MSAD),

$$D_c = \frac{1}{N_c}\sum_{i=1}^{N_c} | < \mathbf{D}_i >^2 |^{1/2} = |R^2|^{1/2}, \tag{4.4}$$

where $\mathbf{D}_i$ is the atomic displacement of the ith atom and N_c is the number of atoms in a finite region. In general, D_c is a coarse grained MAD. In the present model, we use $D(\mathbf{r})$ in the place of D_c, where $\mathbf{r}$ denotes the positions of the coarse grained displacement field. If $N_c = N_{system}$, R^2 is the mean square displacement (MSD) used in the Lindemann's criterion. $D(\mathbf{r})$ usually includes two parts, one from dynamic vibration and another from static atomic displacements, $\mathbf{D}_i(\mathbf{r}) = \mathbf{D}_i(\mathbf{r})_d + \mathbf{D}_i(\mathbf{r})_s$. The MSD is then

$$R^2 = R_d^2 + R_s^2, \tag{4.5}$$

where the cross product of $\mathbf{D}_d \cdot \mathbf{D}_s$ is absent due to randomness of the displacements. Dynamic displacement is defined as

$$R_d^2 = \frac{1}{N} \sum_{i=1}^{N} < (\mathbf{r}_i - < \mathbf{r}_i >)^2 >, \tag{4.6}$$

and static displacement is defined as

$$R_s^2 = \frac{1}{N} \sum_{i=1}^{N} < (\mathbf{r}_i - \mathbf{r}_i^0)^2 >, \tag{4.7}$$

where $< \mathbf{r}_i >$ is the average atomic position and $\mathbf{r}_i^0$ is an underlying lattice position. $< \cdots >$ denotes the time average. At the temperature at which the CGT occurs, the dynamic part is very small compared to the static part.

The SMSD becomes meaningless in liquid state and a crystal close to melting where atomic diffusion sets in. In the solid state, when diffusion is absent, it behaves well on both sides of the crystal to glass transition, although changing the thermal expansion coefficient at different solute concentrations can lead to a small, but noticeable increase well before the transition occurs. It can be easily corrected if a better behaved MSD is desired. Therefore, it can describe first order polymorphic melting.

We also assume that the random, static strain field is small and has long wavelength, so it can also be coarse grained. In general, the strain field also includes the dynamic part due to thermal vibrations of atoms at the temperature,

$$\epsilon = \epsilon_{static} + \epsilon_{dynamic},$$

but it is relatively small compared with the static one in the case of the CGT.

Second, only scalar order parameters are used, $D(\mathbf{r})$ and $\epsilon(\mathbf{r})$, which of course is an oversimplification, but will make our analysis simpler. However, if *atomic* *displacement vector* and all the possible components of *strain tensor* must be considered, we can treat each eigenvector of the SMAD as an independent primary order parameter that can couple to the corresponding component of the strain tensor diagonalized in this eigendisplacement coordinate. Since it is sufficient to have only one strain order parameter in order to trigger the CGT. Without losing generality, we shall not treat the mutiple order parameter Landau theory. In the present model, the primary order parameter is a scalar, the SMAD along the tetragonal principal shear axis, and therefore the secondary order parameter is the tetragonal shear strain tensor component. The elastic constant is thus the tetragonal shear elastic constant, C'.

Third, we assume that the normal first-order transition is not symmetry related, that is, the Landau free energy does not include the cubic term in terms of the primary order parameter D. This assumption is actually valid based on the fact that the primary order parameter is a random variable $\mathbf{D}(\mathbf{r})$, a random atomic displacement vector, for instance. So its average, or coarse grained value is zero,

$$\int d\mathbf{r} < \mathbf{D}(\mathbf{r}) >= 0, \tag{4.8}$$

but its mean square amplitude is not,

$$\int d\mathbf{r} < D^2(\mathbf{r}) >\neq 0, \tag{4.9}$$

where $< \cdots >$ denotes thermodynamic average and the integral is over the entire sample.

For the present model, we assume that the strain field is small in its magnitude. So only the terms of the strain order parameter up to the second order are used in the Landau theory.

Therefore, a Landau free energy that describes such a normal, first order transition can be expanded in a Taylor series in the primary order parameter, $D(\mathbf{r})$, in the following form,

$$F[T, x, D(\mathbf{r})] = F_0(T, x) + \int d\mathbf{r} f[T, x, D(\mathbf{r})], \tag{4.10}$$

where f is the Landau free energy density function that depends on the spatially varying order parameter $D(\mathbf{r})$,

$$\begin{aligned} & f[T, x, D(\mathbf{r})] = \\ & a(T, x)D(\mathbf{r})^2 + b(T, x)D(\mathbf{r})^4 + c(T, x)D(\mathbf{r})^6 + \cdots + \\ & \frac{1}{2}d(T, x)\left|\vec{\nabla}D(\mathbf{r})\right|^2 + \cdots, \end{aligned} \tag{4.11}$$

where the inhomogeneity in the order parameter is presented by a gradient term explicitly. T and x are temperature and composition respectively. $a(T, x), b(T, x), c(T, x)$ and $d(T, x)$ are expansion coefficients. For stability reasons, $c(T, x)$ is assumed to be always positive, $c(T, x) > 0$. $b(T, x)$ is a decreasing function with increasing T and x and it becomes negative at polymorphic melting.

To minimize the Landau free energy functional as presented in (4.10), we performed a functional variation of F with respect to the order parameter, $D(\mathbf{r})$,

$$\begin{aligned} \delta F = \int d\mathbf{r}\delta D(\mathbf{r}) \Big[& 2a(T, x)D(\mathbf{r}) + 4b(T, x)D(\mathbf{r})^3 + \\ & 6c(T, x)D(\mathbf{r})^5 + \cdots + \\ & d(T, x)\vec{\nabla}\delta D(\mathbf{r}) \cdot \vec{\nabla}D(\mathbf{r}) + \cdots \Big]. \end{aligned} \tag{4.12}$$

Under the boundary condition, $\delta D = 0$, minimization of free energy with respect to order parameter leads to

$$\frac{\delta F}{\delta D(\mathbf{r})} = h(\mathbf{r})$$

$$= 2a(T,x)D(\mathbf{r}) + 4b(T,x)D(\mathbf{r})^3 +$$
$$6c(T,x)D(\mathbf{r})^5 + \cdots -$$
$$d(T,x)\vec{\nabla}^2 D(\mathbf{r}) + \cdots, \tag{4.13}$$

where $h(\mathbf{r})$ is the conjugate field of the order parameter D (it is not necessarily the force on atoms).

Assuming the conjugate filed is zero, $h(\mathbf{r}) = 0$, and neglecting the fluctuation term, $\vec{\nabla} D(\mathbf{r}) = 0$, at the moment, then (4.13) will leads to a first-order transition at $T = T_0$ and $x = x_0$, when the expansion coefficient $b(T,x)$ is negative, whereas $a(T,x)$ is still positive. The order parameter at the polymorphic melting transition define by $T_0(x)$ is,

$T > T_0$ or $x > x_0$ (diffusionless supercooled liquid or glass)

$$D_0^2 = -\frac{b}{2c} \tag{4.14}$$

which has a finite jump at T_0, and

$T < T_0$ or $x < x_0$ (metastable crystalline solid solution)

$$D_0 = 0. \tag{4.15}$$

At the transition, the relation $a(T,x) = b(T,x)^2/4c(T,x)$, determines the $T_0(x)$ line, or the polymorphic phase diagram of a binary system at high temperature when strain field is not in effect.

Next we shall consider the case where the free energy will then depend not only on local atomic displacements $D(\mathbf{r})$, but also on the strain.

$$F_{\text{elastic}} = \frac{1}{2} C_0(T,x)\epsilon(\mathbf{r})^2, \tag{4.16}$$

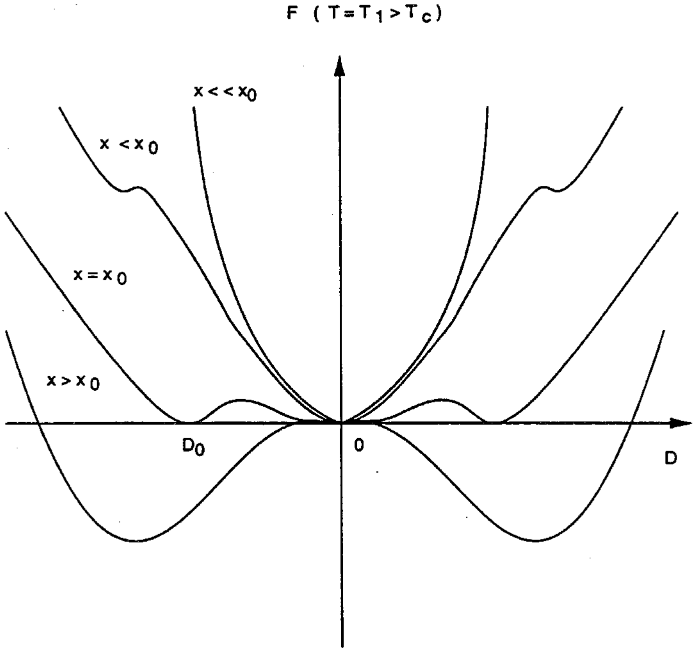

Fig. 4.2 Local Landau free energy for a nonsymmetry driven first-order transition at high temperature ($T = T_1 > T_c$, where T_c is the critical temperature. x_0 is the composition on the polymorphic melting phase boundary $T_0(x_0)$. (see Fig. 4.6 for further explanations).

with the bare, or nonrenormalized elastic constant, C_0, which equals the elastic constants without the SAMD and the presence of static strain ($D_d = 0$ and $\epsilon_{static} = 0$).

Another part is the interaction term that couples the primary order parameter, D, and the second order parameter, the strain field,

$$F_{\text{int}} = e(T,x)D\epsilon(\mathbf{r}). \tag{4.17}$$

Only the linear terms for both order parameters is included. $e(T,x)$ is the coupling parameter. The interaction term reflects the fact that the strain can affect atomic displacements during "relaxation" or a rearrangement process occurring inside the system. It represents the effects of the defects on the atomic displacements. This term is invariant because the fluctuations of D can follow the fluctuations of the strain field. This is true in general for all static displacements. With these two terms included, the new Landau free energy becomes

$$\begin{aligned} f[T,x,D,\epsilon] =& a(T,x)D^2 + b(T,x)D^4 + c(T,x)D^6 + \cdots + \\ & \frac{1}{2}d(T,x)\left|\vec{\nabla} D\right|^2 + \\ & e(T,x)\epsilon D + \frac{1}{2}C_0(T,x)\epsilon^2 + \cdots + \frac{1}{2}g(T,x)|\vec{\nabla}\epsilon|^2, \end{aligned} \tag{4.18}$$

where, for convenience, $\mathbf{r}$ is omitted. The last term is the contribution from the spatial variance of strain field.

Variation of the free energy functional with respect to strain order parameter

$$\delta F = \int d\mathbf{r}\left[\delta\epsilon(eD + C_0\epsilon) + \cdots - g\vec{\nabla}\delta\epsilon \cdot \vec{\nabla}\epsilon\right], \tag{4.19}$$

will lead to the stress field,

$$\left.\frac{\delta F}{\delta \epsilon}\right|_D = \sigma = e(T,x)D + C_0(T,x)\epsilon + g\,\nabla^2\,\epsilon. \tag{4.20}$$

assuming $\delta\epsilon(\mathbf{r}) = 0$ at the boundary.

Let's next consider a homogeneous case where the conjugate local stress is zero and omitting spatial dependence of strain, $\vec{\nabla}\epsilon = 0$, two order parameters are related by

$$\epsilon = -\frac{e(T,x)}{C_0(T,x)}D, \tag{4.21}$$

which implies that atomic displacements are indeed effected by the strain field. Since D and ϵ are "in-phase", or the displacements follow the strain field, the linear term is therefore invariant under inversion symmetry and nonzero when averaged over random configurations (see (4.8)).

Substituting (4.21) into (4.18) to replace strain, one obtains the renormalized Landau free energy,

$$\begin{aligned}\tilde{f}[T,x,D] =&\tilde{a}(T,x)D^2 + b(T,x)D^4 + c(T,x)D^6 + \cdots + \\ &\frac{1}{2}\tilde{d}(T,x)|\vec{\nabla}D|^2,\end{aligned} \tag{4.22}$$

with a renormalized expansion coefficient for the quadratic term,

$$\tilde{a}(T,x) = a(T,x) - \frac{e(T,x)^2}{2C_0(T,x)}. \tag{4.23}$$

and a renormalized coefficient for the gradient term,

$$\tilde{d}(T,x) = d(T,x) + \frac{e(T,x)^2}{C_0(T,x)^2}. \tag{4.24}$$

Equation (4.22) is the central expression for Landau free energy. From now on, we will deal with only the local Landau free energy, (4.22), without the order parameter gradient term present. Without losing generality, the order parameters are coarse grained over a local region. The inhomogeneous Landau theory with the gradient term and present will be treated at the end of this section to investigate how correlation lengths behave close to different transitions. Next, we shall present the thermodynamic properties derived from the Landau theory.

A. Critical Point, Crossover

The coefficient $a(T,x)$ as defined by (4.23) is reduced by the presence of the random strain field through the strain-displacement interactions. The shift of the quadratic term coefficient from $a(T,x)$ to $\tilde{a}(T,x)$ changes not only the $T_0(x)$ line

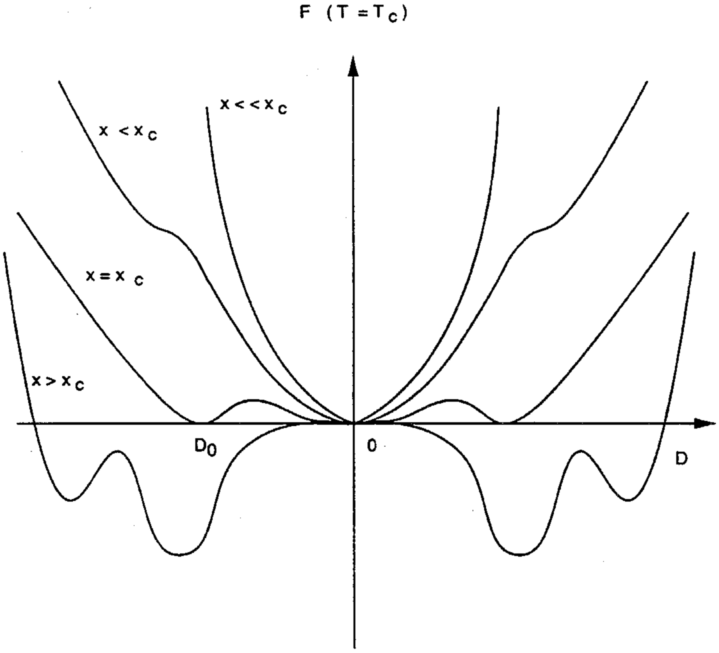

Fig. 4.3 Local Landau free energy for a nonsymmetry driven first-order transition at temperature ($T = T_c$), (see Fig. 4.6 for further explanation). Random strain field is included. The instability occurs when $\tilde{a} = 0$ and $b = 0$ where a second order transition preempts the first-order transition.

but also the nature of the first-order transition at the critical point which we discuss next (see Fig. 4.3).

The shift of $T_0(x)$ line is determined by

$$\tilde{a}(T,x) = a(T,x) - \frac{e(T,x)^2}{2C_0(T,x)} = \frac{b(T,x)^2}{4c(T,x)} \tag{4.25}$$

Fig. 4.4 shows the shift of the first-order transition to lower temperature and lower concentration, (T_0', x_0'). The change of the order parameter can be determined from the following equation

$$\tilde{D}_0 = -\left.\frac{b(T,x)}{2c(T,x)}\right|_{T_0', x_0'}, \tag{4.26}$$

with $b(T,x)$ now determined by (4.24). The first-order transition is smeared over a range $\Delta x = (x_0 - x_0')$ at the temperature $T_1 > T_c$ (see Fig. 4.4).

The first-order polymorphic melting transition becomes continuous if the renormalized coefficient can be reduced such that when $b(T,x) \to 0$, $\tilde{a}(T,x) \to 0$, simultaneously. The state point defined by this condition is a critical point, $(T = T_c, x = x_c)$ (see Fig. 4.3) where a line of first-order transition becomes terminated in a continuous one. At this point, the order parameter becomes completely smeared out. The discontinuities of the first-order thermodynamic properties, such as entropy and chemical potential are also smeared out.

B. Entropy

The entropy change is finite at a first-order polymorphic melting transition,

$$\begin{aligned}\Delta S\Big|_{(T,x)} &= S^+ - S^- = -\left(\frac{\partial \tilde{f}^+}{\partial T} - \frac{\partial \tilde{f}^-}{\partial T}\right) \\ &= -\frac{b}{2c}\tilde{a}_T + O(b^2), \end{aligned} \tag{4.27}$$

where $\tilde{f}^+$, $\tilde{f}^-$, S^+ and S^- are renormalized free energies, entropies of metastable liquid and crystalline phases respectively. $\tilde{a}_T$ is the partial derivative of $\tilde{a}$ with respect to T. As the critical point is approached, $b(T,x) \to 0$, then entropy vanishes. So there is no latent heat associated with the transition.

C. Chemical Potential

The chemical potential change, or chemical affinity, at each composition can also be obtained by differentiating the Landau free energy with respect to composition, then

$$\Delta\mu\Big|_{(T,x)} = \mu^+ - \mu^- = \frac{\partial \tilde{f}^+}{\partial x} - \frac{\partial \tilde{f}^-}{\partial x}$$

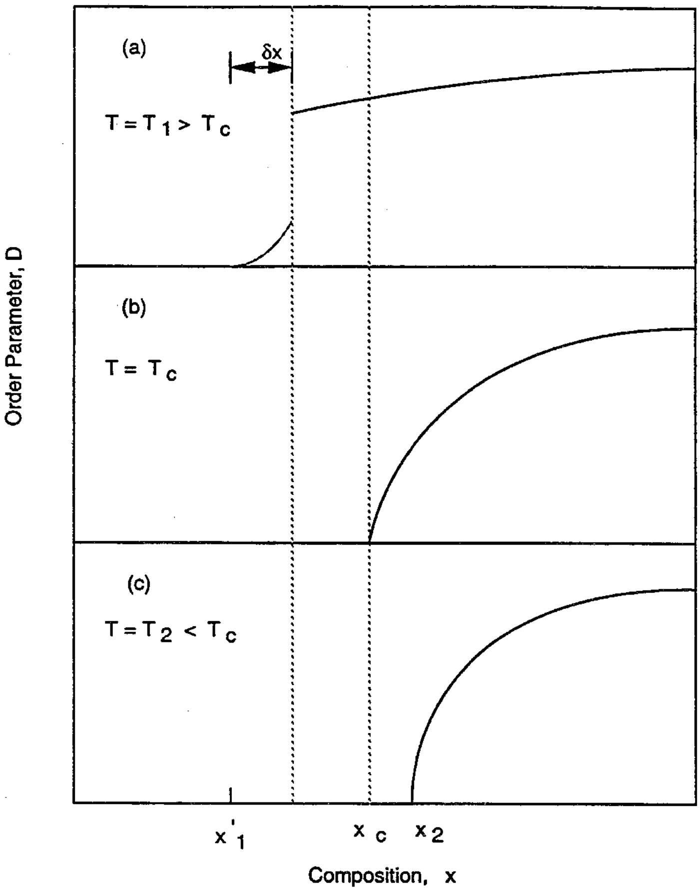

Fig. 4.4 Order parameter *vs.* solute composition x at different temperatures. (a) The shift of x_0 at $T = T_1 > T_c$ is δx; (b) this smearing effect suppresses the first-order transition completely when (T_c, x_c) is approached; (c) at lower temperature, the CGT is described by line OC defined in Fig. 4.6.

$$= \frac{b}{2c}\tilde{a}_x + O(b^2), \tag{4.28}$$

where $\tilde{a}_x = \partial\tilde{a}/\partial x$. The chemical potential difference, or the chemical affinity, is finite for the first-order transition, but becomes zero at the critical point. So the potential for driving atoms to diffuse vanishes.

D. Elastic Constants

Next we shall devote our attention to investigate the behavior of elastic constant close to the critical point. C_0 is the bare, or unnormalized elastic constant when random, static displacement and strain field are absent.

An elastic constant in general can be obtained from the second derivative of the Landau free energy with respect to strain,

$$C = \frac{\delta^2 \tilde{F}}{\delta \epsilon^2}, \tag{4.29}$$

where $\tilde{F} = F[D(\epsilon), \epsilon]$ is used. In order to obtain the equilibrium elastic constant, we need to minimize the Landau free energy with respect to the primary order parameter, from which the relation between strain ϵ and the order parameter D can be obtained.

$$\left.\frac{\delta F}{\delta D}\right|_{\sigma} = 0, \tag{4.30}$$

which gives

$$eD[\epsilon] = -\left[2aD + 4bD^3 + 6cD^5\right]. \tag{4.31}$$

From the above relation we obtain

$$\frac{\partial D[\epsilon]}{\partial \epsilon} = -\frac{e}{2a + 12bD^2 + 30cD^4} = -e\chi_0, \tag{4.31$'$}$$

where χ_0 is the unnormalized primary order parameter susceptibility defined as

$$\chi_0 = \left(\frac{\delta^2 F}{\delta D^2}\right)^{-1}. \tag{4.32}$$

Therefore, an elastic constant at T and x is

$$C(T,x) = C_0(T,x) - e(T,x)^2 \chi_0(T,x). \tag{4.33}$$

At the critical point, the unnormalized susceptibility equals

$$\chi_0\Big|_{(T_c,x_c)} = \frac{C_0}{e^2}, \tag{4.34}$$

when $\tilde{a} = 0$ as given by equation (4.23) and $D = 0$ at the critical point, so the elastic constant becomes zero. Fig. 4.5 shows the elastic constant $C(T, x)$ *vs.* solute composition x as predicted using eq. (4.33).

E. Correlation Lengths and Fluctuations

So far, we have been dealing with only a homogeneous Landau theory with order parameters that are coarse grained. Therefore, this treatment can give us only local information about a phase transition of a homogeneous system. For instance, smearing of the first order transition, the shift of transition temperature and composition, are occurring only in a finite region defined by the correlation length of the disordered phase. In order to gain insight of how inhomogeneity and fluctuations in both order parameters affect the transition, we shall treat the inhomogeneous Landau theory given in (4.22) to obtain correlation lengths of order parameters at the topological order and disorder transition. Inhomogeneous order parameter can be written as

$$D(r) = D_0 + \varphi(r), \tag{4.35}$$

where D_0 is the coarse grained, homogeneous order parameter, independent of positions $\mathbf{r}$ and $\varphi(r)$ is fluctuation of order parameter. We also assume that the stress associated with the random, static strain field is fully relaxed (the relation (4.21) holds).

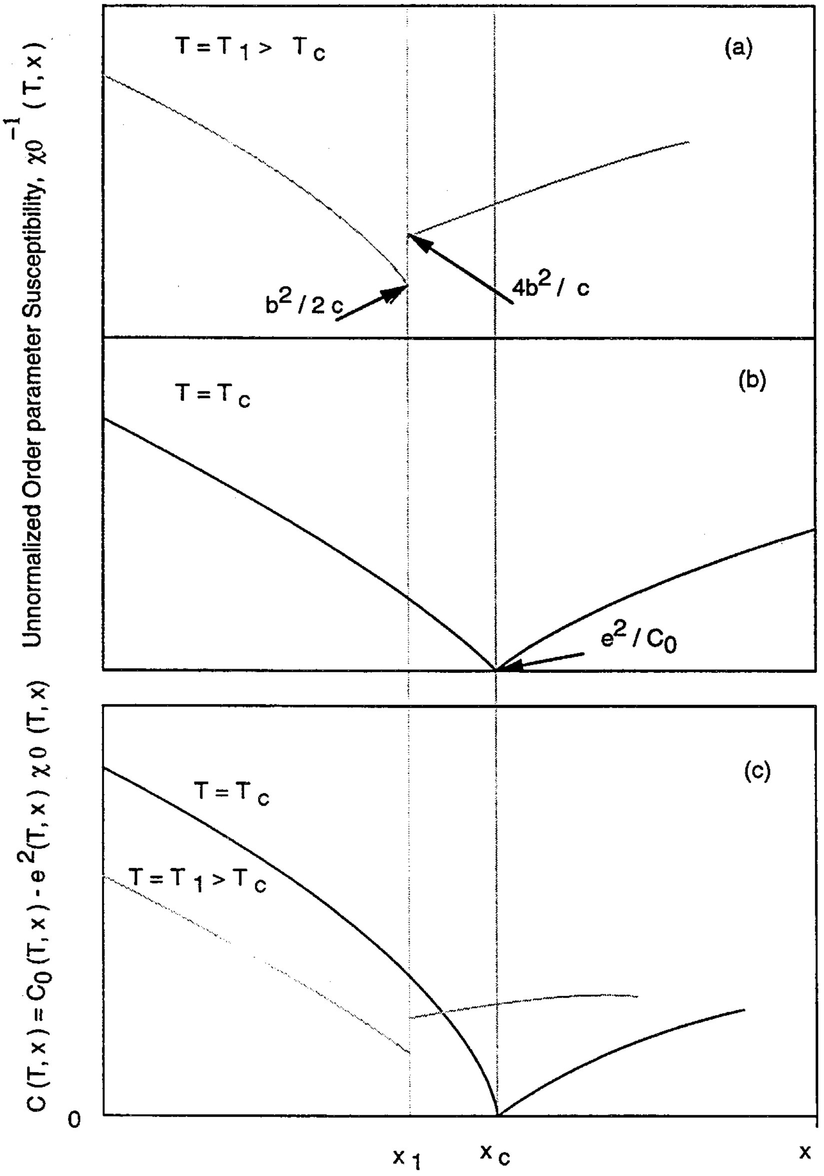

Fig. 4.5 Elastic constants versus composition at higher temperature $T = T_1 > T_c$ and at the critical temperature T_c. The finite jump at $T > T_c$ is due to a finite jump of χ_0 for a first-order transition (a). The elastic constant becomes zero at T_c where $\chi_0 = C_0/e^2$ (b).

To simplify our analysis, we will confine ourselves only to the region close to the critical point. By doing so, we can make the assumption that the order parameter fluctuations, $\varphi(r)$, are relatively small and thus can be linearized.

At $T > T_c$ the transition is shifted to lower temperature and composition, but is still first-order, and the homogeneous order parameter is given by (4.26) and the expansion coefficients by (4.25). If the system is isotropic, $\mathbf{r}$ is replaced by r. Keeping only the linear terms in $\varphi(r)$, we get

$$D(r)^2 \simeq D_0^2 + 2D_0\varphi(r), \tag{4.36}$$

$$D(r)^3 \simeq D_0^3 + 3D_0\varphi(r), \tag{4.37}$$

etc..

Variation of the nonuniform Landau free energy (4.22) gives

$$\delta F = \int d^3r \Big[\delta D(r)\Big(2\tilde{a}(T,x)D(r) + 4b(T,x)D(r)^3 + \\ 6c(T,x)D(r)^5\Big) + \cdots + \tilde{d}(T,x)\delta D(r) \cdot \vec{\nabla} D(r)\Big]. \tag{4.38}$$

Integrating the last term by parts and using boundary condition $\delta D(r) = 0$, (4.38) becomes

$$\delta F = \int d^3r\delta D(r)\Big[2\tilde{a}(T,x)D(r) + 4b(T,x)D(r)^3 + \\ 6c(T,x)D(r)^5 + \cdots - \tilde{d}(T,x)\vec{\nabla}^2 D(r)\Big]. \tag{4.39}$$

The conjugate field equals

$$h(r) = \frac{\delta F}{\delta D(r)} = 2\tilde{a}D(r) + 4bD(r)^3 - \tilde{d}\,\nabla^2\, D(r). \tag{4.40}$$

Substitute (4.36), (4.37) and (4.25) in to (4.40), we obtain the following equation for the order parameter fluctuations,

$T < T_c$

$$\nabla^2\varphi(r) - \frac{2\tilde{a}}{\tilde{d}}\varphi(r) = -\frac{1}{\tilde{d}}h(r), \tag{4.41}$$

and

$T > T_c$

$$\nabla^2\varphi(r) - \frac{2b^2}{c\tilde{d}}\varphi(r) = -\frac{1}{\tilde{d}}h(r), \tag{4.42}$$

The above equation can be solved easily using Green's functions, with $h(r)$ replaced by $h_0\delta(r)$. Then

$$\varphi(r) = \frac{h_0}{4\pi\tilde{d}}\frac{1}{r}e^{-r/\xi}, \tag{4.43}$$

where for

$T < T_c$

$$\xi = \left[\frac{\tilde{d}}{2\tilde{a}}\right]^{1/2}, \tag{4.44}$$

and for

$T > T_c$

$$\xi = \left[\frac{c\tilde{d}}{2b^2}\right]^{1/2}. \tag{4.45}$$

For a first-order transition, the correlation length is finite. This in fact can be seen from (4.45). Both b and $\tilde{a}$ are finite so is the correlation length. However, the correlation lengths become divergent when the critical point is approached, where both b and $\tilde{a}$ become zero simultaneously. It implies that as the CGT is approached at $T \leq T_c$ by increasing composition x, the disorder fluctuations become stronger and spread farther. It is also interesting to note that the coupling to a random strain field leads to a larger $\tilde{d} = d + e^2/C_0^2 d$, thus resulting in a longer correlation length even for the first-order transition.

F. Phase Diagrams

From the above discussion and results, we can roughly estimate the phase diagram of the metastable polymorphic transition using the Landau theory presented above. In order to obtain a detailed phase diagram, specific assumptions for the expansion coefficients have to be made in order to proceed with the analysis. The choice of these parameters varys depending on different material parameters in the supercooled regime of a liquid, or superheated regime of a crystal. Unfortunately they are not widely available. Therefore, we only discuss some important features of the metastable phase diagram for polymorphic melting.

The condition $\tilde{a}(T, x) = 0$ determines the phase diagram for the continuous transition at $T < T_c$. The slope of this phase boundary is thus

$$\left.\frac{\partial T}{\partial x}\right|_{continuous} = -\frac{\frac{\partial \tilde{a}}{\partial x}}{\frac{\partial \tilde{a}}{\partial T}} = -\frac{\tilde{a}_x}{\tilde{a}_T}, \tag{4.46}$$

where the subscripts denote partial derivatives. Whereas the phase boundary of the polymorphic melting at $T > T_c$ can be determined similarly using relation (4.25) obtained at the normalized first-order transition. Then

$$\left.\frac{\partial T}{\partial x}\right|_{discontinuous} = -\frac{\tilde{a}_x c + \tilde{a} c_x - \frac{3}{8} b b_x}{\tilde{a}_T c + \tilde{a} c_T - \frac{3}{8} b b_T}. \tag{4.47}$$

At the critical point, both $\tilde{a}(T, x)$ and $b(T, x)$ approach zero, so (4.47) reduces to (4.46). Therefore, crossover from a first-order to a continuous one is smooth and continuous.

From eqs. (4.46) and (4.47) we can get a glimpse of the phase digram, (T, x), if the functional forms of the Landau expansion coefficients are explicitly known. But a complication arises in determining the derivative (4.47) when the transition becomes continuous, because the derivative is proportional to the ratio between the chemical potential difference (4.28) and entropy change (4.27), to the order of $O(b^2)$, which approach zero simultaneously at T_c. So (4.47) is not determined at the (T_c, x_c).

Using the condition of continuity and eqs. (4.27) and (4.28), at $T \leq T_c$, we can write

$$\left.\frac{\partial T}{\partial x}\right|_{\text{continuous}} = -\frac{\tilde{a}_x}{\tilde{a}_T} \simeq \frac{\Delta\mu}{\Delta S} = \left.\frac{\Delta\mu_x}{\Delta S_x}\right|_{(T,x)\to(T_c,x_c)}, \tag{4.48}$$

where higher order derivatives of $\tilde{a}(T, x)$ are used (L'Hôspital's rule) as the critical point is approached. In fact, (4.45) suggests that a precise phase diagram for the crystal to glass transition in the vicinity of T_c depends on the rate of change of chemical potential and entropy with respect to change in composition.

$\Delta\mu_x$ is related to the second derivative of Landau free energy by

$$\left.\Delta\mu_x\right|_T = \frac{\partial^2 \Delta F}{\partial x^2}, \tag{4.49}$$

which is always positive definite (see Gibbs stability criterion, equation (3.3)), except for a system that exhibits spinodal decomposition. Such chemically unstable situation involves two competing processes, chemical spinodal mixing and the CGT. We will not discuss this case at the moment. For chemically stable systems, the phase digram of a continuous CGT in such a system is solely determined by ΔS_x, or $-\Delta\mu_T$ which is obtained using Maxwell relations. Then (4.48) becomes

$$\frac{\partial T}{\partial x} \simeq -\frac{\Delta\mu_x}{\Delta\mu_T}, \tag{4.50}$$

in the vicinity of (T_c, x_c).

This relation reflects the importance of the kinetic constraint on the binary system and on the metastable phase transition. As we discussed before, the polymorphic transition is characterized by a nonzero chemical potential $\Delta\mu$. Without it, the transition would proceed with equilibrium phase transitions, most likely, phase separation. In this case, $\Delta\mu = 0$ and the $\partial T/\partial x$ becomes zero, and thus the phase transition degenerates to normal phase coexistence. From (4.49), it can be seen that the nonzero chemical potential, $\Delta\mu$, and its change with respect to both temperature and composition, $\Delta\mu_T$ and $\Delta\mu_x$, ultimately determine the phase diagram in the vicinity of the critical point.

According to the manner of how $\Delta\mu_T$ changes, the CGT can take three possible turns at $T < T_c$, as illustrated in Fig. 4.6. For cases where $\Delta\mu_T$ is negative or zero, the phase diagram is characterized by

$$\frac{\partial T}{\partial x} \to \infty, \tag{4.51}$$

at the critical point. For the former, the phase boundary bends back for $T < T_c$ and $x < x_c$ (line OA in Fig. 4.6), which corresponds to a situation of re-entrant melting [4.14] where a glass, or supercooled liquid can form upon *cooling*. Whereas for the latter, $T_0(x)$ becomes a vertical line at $x = x_c$ (line OB in Fig. 4.6). If the entropy increases with increasing temperature, or $\Delta\mu_T$ is positive, the phase boundary will extend over to higher concentrations (line OC or OD in Fig. 4.6). But its detailed shape is again determined by higher order derivatives of $\Delta\mu$ with respect to T and x.

Finally, we ask the question: does T_c correspond to the glass transition temperature? In order to answer this question, one needs to have a theory that includes liquids and glasses, or supercooled liquids. Unfortunately the Landau theory presented above includes only crystalline solids and a supercooled, diffusionless liquid or glasses, so a direct answer cannot be provided.

However, one can get an answer based on the assumption that an amorphous phase formed by CGT from a crystal is the same as that formed from a supercooled liquid. So on the metastable phase diagram shown in Fig. 3.1 and Fig. 4.6, a $T_g(x)$ has to coincide with $T_c(x)$ where three phases, a diffusionless liquid, a crystal and a glass, coexist. Since the ideal T_g is determined under the condition $\Delta S = 0$, it will coincide with the ideal glass transition temperature, T_K, or Kauzmann temperature if liquid to glass transition occurs as predicted by Kauzmann's entropy crisis [3.22]. At this temperature, the entropy difference between a supercooled liquid and a glass is zero, as it is between a metastable crystal and a glass.

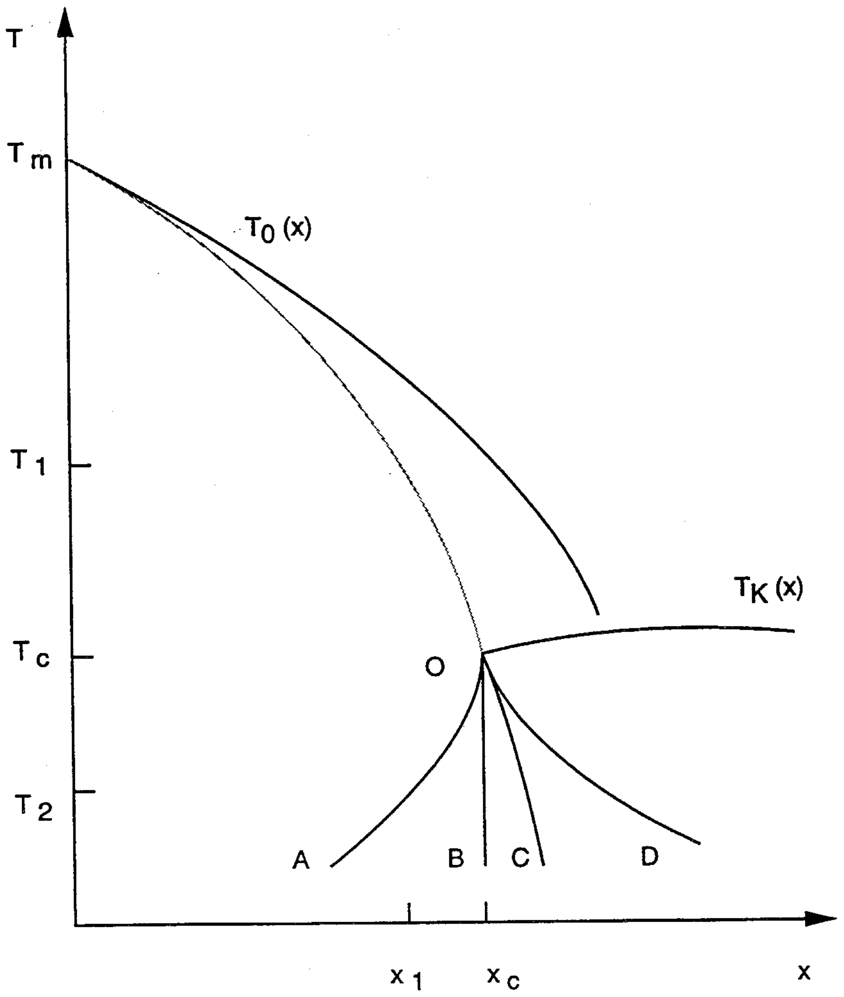

Fig. 4.6 Metastable phase diagram for the binary solid solution undergoing the CGT. Note the differences compared with Fig. 3.2. (T_c, x_c) is the critical point. Solid line at higher temperature defines the original polymorphic melting transition and the dotted line is polymorphic melting corrected by including random strain field. T_K is Kauzmann's temperature, or ideal glass transition temperature, which is a lower bound on the glass transition temperature obtained from rapid solidification experiments.

References

4.1 A. B. Harris, J. Phys. C, **7**, 1671, (1974).

4.2 Y. Imry and M. Wortis, Phys. Rev. B, **19**, 3580, (1979).

4.3 B. M. Bruce, J. Less-Common Metals, **140**, 57 (1988); B. M. Bruce and T. C. Hufnagel, J. Less-Common Metals, **194**, 221 (1993).

4.4 M. Atzmon. J. R. Veerhoven, E. R. Gibson and W. L. Johnson, Appl. Phys. Lett., **45**, 1052, (1984).

4.5 J. F. M. Westendorp, Ph.D. Thesis, University of Uthrecht, Netherlands (1986); S. Schneider, R. Bush, W. Bolse and K. Samwer, J. Non-crystal. Solids, **156**, 608 91993).

4.6 C. V. Thompson and F. Spaepen, Acta Metall., **31**, 2021, (1983).

4.7 B. M. Clemens, J. Less-Common Metals, **140**, 57, (1988); B. M. Clemens and T. C. Hufnagel, J. Alloys and Compounds, *194*, 221 (1993).

4.8 W. J. Meng, J. Faber, P. R. Okamoto, L. E. Rehn, B. J. Kestel and R. L. Hitterman, J. Appl. Phys., **67**, 1312 (1990).

4.9 H. J. Fecht, P. J. Desré and W. L. Johnson, Phil. Mag. B, **59**, 577, (1989).

4.10 B. J. Alder and T. E. Wainwright, Phys. Rev., **127**, 359 (1962).

4.11 J. Tobochinik and G. V. Chester, Phys. Rev. B, **25**, 6778 (1982).-

4.12 J. Zarzycki, *Glasses and the Vitreous State*, (Cambridge University Press, Cambridge, 1982).

4.13 annealing brittlement.

4.14 A. L. Greer, J. Less-Common Metals, **140**, 327 (1988).

Chapter 5

Crystal to Glass Transition and Melting in Two Dimensions

5.1 Introduction

In chapter 3, the crystal to glass transition in a clean, bulk and homogeneous binary solid solution was investigated. Structural and thermodynamic properties obtained from molecular dynamics simulations suggest that the transition can be described by thermodynamics and can be linked to an instability represented by diminishing shear elastic constants, entropy and density. Such a phenomenon was interpreted using a Landau theory to bridge the gap between microscopic entities, the atomic displacement field and strain field, and the topological transition. This Landau theory also provides information at the possible critical CGT where computer simulations have not yielded precise results. As shown by these results, the random, static strain field caused by defects is retained due to slow kinetics of the relaxation of chemical (polymorphic constraint) potential on microscopic scales. The inhomogeneous atomic displacements represented primarily by the random strain fields can effectively smear out the polymorphic transition. When the static, random strain reaches the critical fluctuation, the long-range coupling, which gives rise to cooperative behavior of atoms, becomes a short-range one and as a results, the system loses the elastic shear rigidity. Therefore, the atoms, or groups of atoms within this short correlation length, can be driven and displaced randomly, thus leading to a continuous polymorphic melting: the CGT.

The purpose of this chapter is to provide the direct microscopic evidence that supports this scenario and to link the phenomenon to microscopic structural defects that are ultimately responsible for the topological disordering. Structures, atomic configurations, and especially, a variety of defects are among the features that we are mostly interested in. Topological disordering is reflected in the behavior of both the translational and the orientational symmetry of the system. From subtle changes in symmetry, the role of defects, in particular, those of a topological nature, can be clearly comprehended. Atomic configuration evolution as well as the behavior of these defects are of particular importance to reveal the microscopic mechanisms for the CGT which we proposed above.

As we mentioned, computational effort can be greatly reduced in two-dimensional systems. Therefore, we can afford to make simulations with larger systems and run longer times. Another distinct feature of a two-dimensional system which its three-dimensional counterpart lacks, is its visualizability. With appropriate mapping techniques, a variety of atomic defects, microstructures and atomic configurations can be directly observed in two-dimensional systems, whereas it would be very difficult in the three-dimensional case.

Dynamic properties can also be easily obtained in two-dimensional systems using molecular dynamics. From dynamic as well as static correlation functions of different physical quantities, we can obtain the characteristic spatial and temporal scales for configurational, defect, and kinetic changes of the system undergoing the CGT.

Melting theory is far more advanced in two dimensions than in three dimensions. This provides an opportunity to directly compare it with the CGT, even in microscopic details. The unique mechanism of disordering crystallinity at low temperature such as in the CGT, leads to a possibility of realizing the so called defect unbinding mechanism of melting [5.1], which is the only existing analytical model for melting so far, but has been the subject of much controversy. Through comparison with our simulation results, we expect to gain insight for the understanding of melting and the CGT.

5.2 Computational Method

The molecular dynamics simulation technique used here is essentially the same as we presented in 2.3, except for a few modifications which we shall discuss next. First, we used a Lennard-Jones potential that has a smooth cutoff achieved by using a switch function [5.2],

$$\phi(r_{ij}) = -4\epsilon_{\alpha\beta}\left[(\frac{\sigma_{\alpha\beta}}{r_{ij}})^{12} - (\frac{\sigma_{\alpha\beta}}{r_{ij}})^{6}\right]S(r_{ij}), \tag{5.1}$$

where α and β denote two types of atoms, A and B. $S(r_{ij})$ is the switch function which is defined as

$$S(r) = \begin{cases} 1, & r \le r_l \\ 1 - \frac{(r-r_l)^2(3r_c-r_l-2r)}{(r_c-r_l)^3}, & r_l < r < r_c \\ 0, & r \ge r_c \end{cases}$$

where r_c and r_l are cutoff distance and the distance at which $S(r)$ joins $\phi(r)$ smoothly (Fig. 5.1). This modification of potential could guarantee the minimum of errors caused by cutoffs during long simulations.

Second, different sizes of a binary solid solution were tried in order to determine the finite size effect. We did find that there is a minimum size below which the random solution does not look random, even though solute atoms on the lattice are still dispersed using a random number generator. The reason is simple. Because a true random distribution can be realized only when a sample is large. A

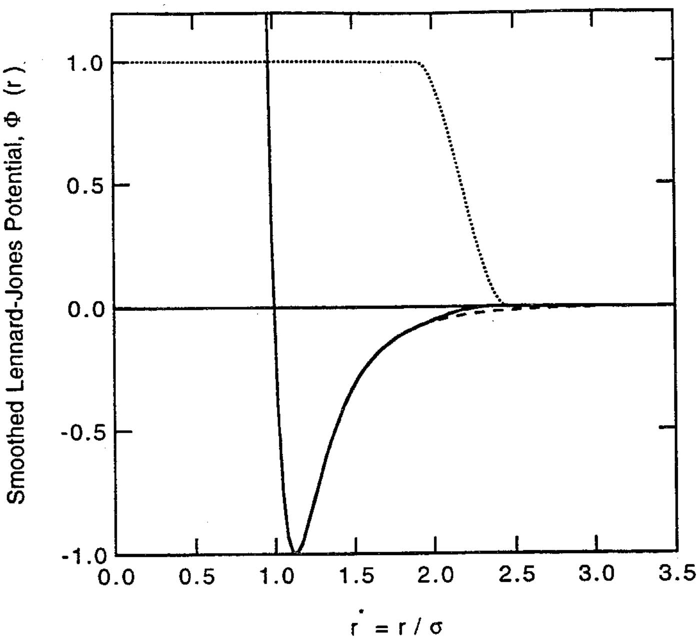

Fig. 5.1 Smoothed Lennard-Jones Potential. The dashed line is the original LJ potential, the broken line is the switch function and the solid line is the smoothed LJ potential. The cutoff distance is 2.45σ for interactions between A-A, A-B and B-B atoms.

small sample size cannot guarantee this. This finite size effect is entirely different from the one due to thermal fluctuations close to critical transitions. To reduce the size effects on randomness, in addition to use larger sample size, we normally prepare several samples with different initial solute distributions. The final results are obtained by averaging over all these samples (2.29) which have different initial configurations. This has been found to be satisfactory, even quite close to the CGT.

A normal MD simulation usually consists of $10^5 \sim 10^6$ MD steps (one MD step is approximately 1.1×10^{-14} second, or 11 femto seconds, for the LJ parameters of crystalline argon) to equilibrate the system, and followed by another $10^6 \sim 10^7$

steps, which is roughly 50 nanoseconds, to obtain thermodynamic averages. The simulation time need to obtain convergent thermodynamic averages has been found to increase when the system gets close to the transition. So in the vicinity of the transition, we normally increase both the equilibrating time and the time to obtain averages. However, at a critical solute concentration very close to the CGT, the time and size needed to achieve a satisfactory convergence appear diverging.

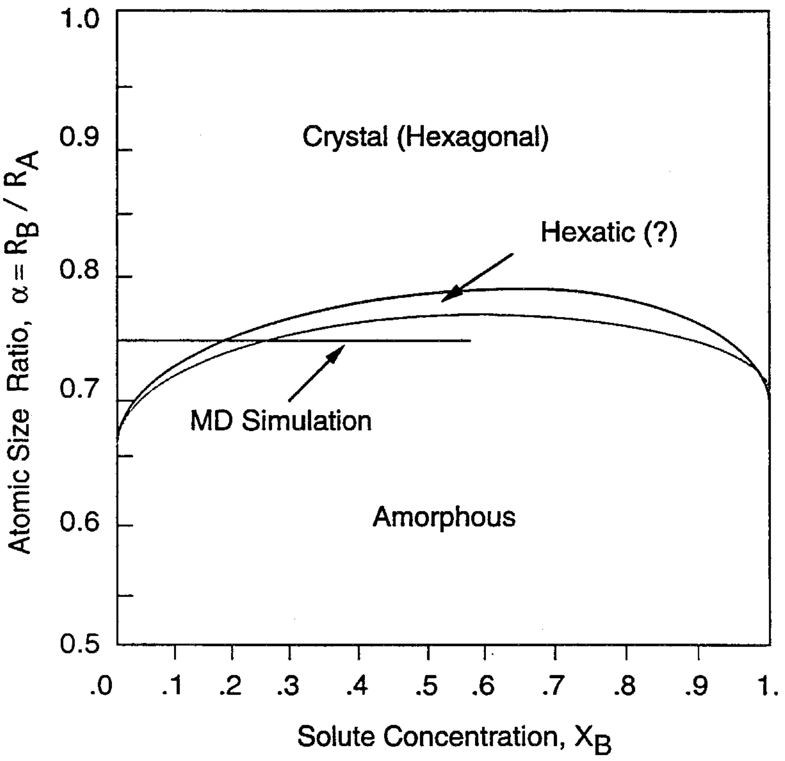

Fig. 5.2 Phase diagram for two-dimensional binary substitutional solid solution with hexagonal crystal structure at $T = 0.20$ and $P = 0.00$. The atomic size ratio $\alpha = 0.75$. The so-called hexatic phase is characterized by quasi-long range orientational order and short-range translational order. Its microstructure suggests that it is composed of "crystalline-like" clusters and glassy regions. (see text for details).

As in the three-dimensional case, we performed the simulation under constant temperature and pressure. The atomic sizes and concentration are varied. A phase diagram of the metastable phases found for two-dimensional binary solid solutions is quantitatively similar to that of the three-dimensional one (Fig. 5.2). In the following sections, we shall present detailed results obtained from these simulations.

5.3 Atomic Configuration and Structural Change

The lattice structure used in the two-dimensional binary solid solution is hexagonal. It is the only close packed structure in two dimensions. There is a distinct difference between two-dimensional and three-dimensional packings in terms of the relation between their local and global packing, or symmetry. Local symmetry of a three-dimensional crystal prefers either tetrahedral or icosahedral symmetry. This local symmetry, usually adopted by forming clusters of the local symmetry, is energetically favored [5.3-4], but does not lead to long-range crystalline translational symmetry. The preferred local symmetry in two dimensions is triangular. This naturally leads to the closed packed hexagonal symmetry for crystalline phases. Because of this difference, glass formability in a two-dimensional monoatomic system is extremely difficult. However, such a preferred local triangular symmetry can be broken by introduction of different types of atoms, as in solid solutions, which have different atomic sizes. So the isomorphism of local and global symmetry can be eliminated.

Similarly as in three dimensions, a random binary array of two different atoms with different atomic sizes is generated by randomly dispersing solute atoms onto hexagonal lattice sites originally occupied by solvent atoms. The crystal to glass transition therefore will crucially depend on the atomic size difference and the solute concentration.

The melting temperature for the two-dimensional pure LJ hexagonal solid with interatomic interaction given by (5.1) was found to be about 0.41 $\sim$ 0.43 (in reduced LJ units) and the glass transition temperature is around 0.25 $\sim$ 0.28, which is close to one half of the melting temperature. Our simulation is performed at temperatures below the glass transition temperature. The phase diagram shown in Fig. 5.2 is for a binary array at $T = 0.20$. At such a low temperature, long-range diffusion is absent (see details in section 5.5), so the polymorphic constraint is strictly maintained. Solute atoms will not move far from the lattice sites where they were dispersed initially. The atomic size ratio between the smaller solute atom and the bigger solvent atoms was varied from 1.0 to 0.70. It was found that a critical atomic size ratio, α_c, is needed to induce the CGT in two dimensions. Its value is relatively smaller, or the size mismatch is larger, than that of its three-dimensional counterpart. For example, $\alpha_c = 0.75$ at $T = 0.20$ for two-dimensional binary array, while it is only 0.83 for the three-dimensional fcc solid solution, both of which are at temperature approximately equal to $0.5T_m$. The critical concentrations of solute atoms at this temperatures is roughly the same, that is, 19 $\sim$ 25 at.% for both cases.

These results seem to contradict the general prediction made for two-dimensional crystalline solids [5.5, 5.6, 5.7] that they are unstable thermodynamically, because thermal fluctuations can effectively destroy long-range translational symmetry. However, the spatial scales at which a crystalline solid loses its translational symmetry was shown to be on the order of $ln(N)$ [5.8], where N is the total number of unit cells in a two-dimensional crystal. In order to have a mean square displacement comparable to lattice spacing, which usually is a few angstroms at melting (as in Lindemann's criterion [3.14]), the area of the two-dimensional crystalline solid has to reach the order of $\sim 10^{27}$ cm^2 [5.9]. Therefore, two-dimensional crystalline solids do exist, but their translational symmetry is no longer a constant over distances; rather their correlation functions decay algebraically [5.5, 5.6, 5.7]. For glass formability, it is the total number of degrees of freedom of the atoms that is more important. In three dimensions, atoms have more freedom to execute displacements from their equilibrium lattice positions than in two dimensions. Therefore, it is easier to form a glass in three dimensions.

Another factor effecting the glass formability is related to the isomorphism of local and long-range symmetry in two dimensions as we discussed early. In order to break the local triangular packing, the atomic size mismatch of the two different atoms must be larger than that in three dimensions where such an effort is essentially unnecessary [5.3].

Fig. 5.3 (a)-(e) show the radial distribution functions of the two dimensional binary array made of two types of atoms with atomic size ratio $\alpha = 0.75$. The RDF's have the same behavior as those observed in three dimensions: namely, the broadening of each crystalline peak and a decrease of intensities as solute concentrations increase. At roughly 20 at.% solute concentration, the RDF's transformed to that of a rapidly quenched glass. The peaks beyond the second and third ones are essentially smeared out and become flat.

As the solute concentration increases, small but noticeable peaks appear at the position of the total RDF's that corresponds to those of the first peak of the partial RDF's of A-B and B-B atoms. This is caused essentially by the lack of mobilities of atoms at such a low temperature. Upon heating slightly, they will disappear. They do not have any effect on the local chemical and structural order. Indeed, one can get a quantitative result by examining the probability distribution of nearest neighbor atoms as shown in Fig. 5.4 (a) and (b). As shown in Fig. 5.4 (a), the mean of the distribution of solute atoms B around a solvent A atom always agrees with the average nearest neighbor numbers for the given solute concentration. Deviations from this usually result in either clustering (the mean is less than the solute composition, or more solvent atoms around a solvent atom) or short-range order (the mean is greater than the solute composition, or more solute atoms around a solvent atom). So the distribution of solute atoms is macroscopically homogeneous.

The partial RDF's (Fig. 5.3(b)-(e)) contain more subtle details of structural change. Even when the system becomes amorphous ($x > 0.199$), the partial RDF's still show a well resolved double maximum at the second peak. But the peaks at distances beyond the second nearest neighbors become more broadened and approach unity as the solute concentration increases further. The spatial scale of the ordered regions is approximately close to the third or fourth nearest neighbor distance, even in the amorphous phase. This finding is also supported by more detailed, quantitative results from various correlation functions (see 5.4).

Detailed atomic configurations at each stage of the structural evolution can be seen in Figs. 5.5. Systematic changes of atomic configurations at different solute concentrations are apparent. We shall briefly summarize several outstanding features observed from these configuration changes. These features support the arguments we put forward in chapter 4 for construction of the Landau theory. In the present two-dimensional model, we can obtain direct evidence by visual inspection.

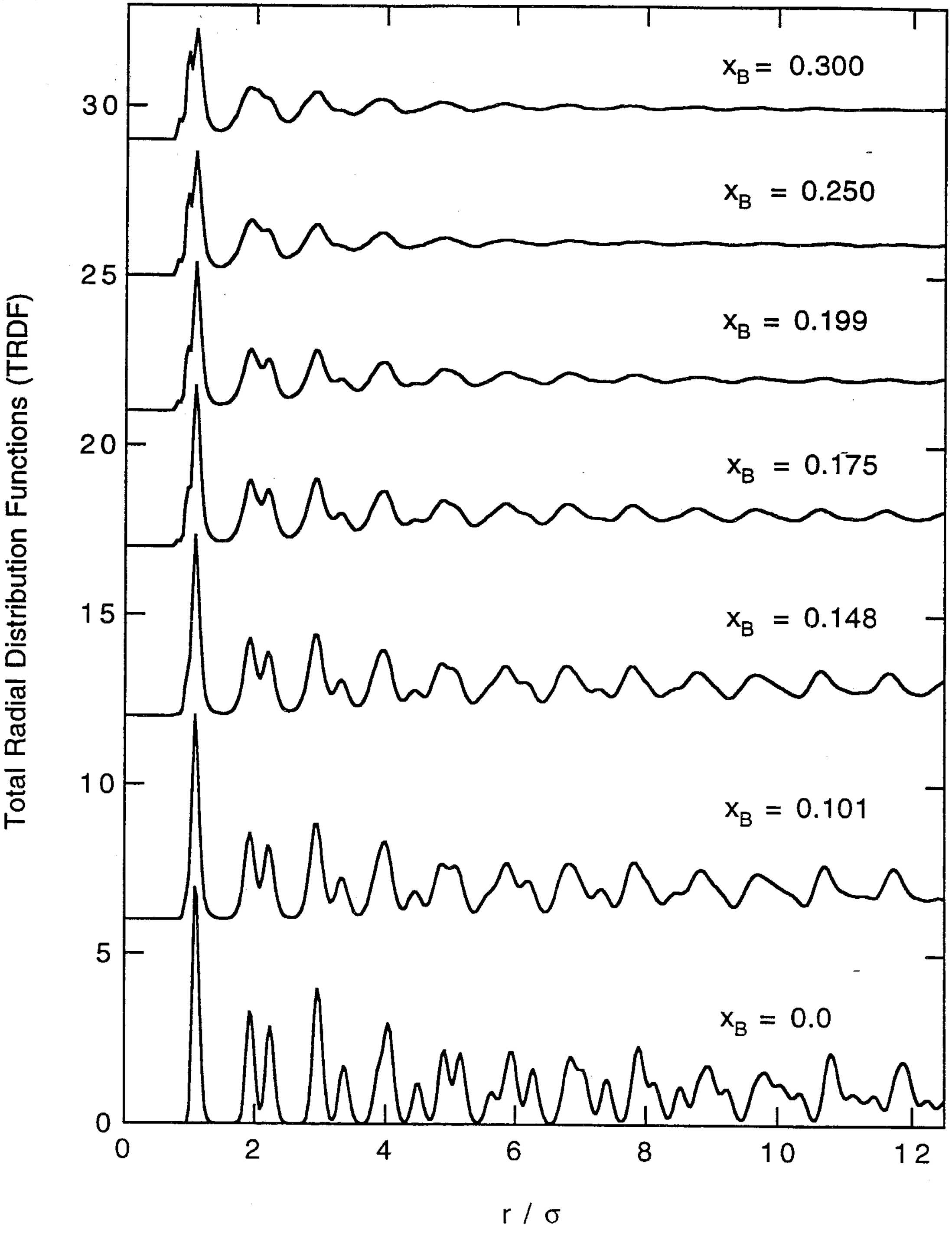

Fig. 5.3 (a) The total radial distribution functions for the two-dimensional solid solutions at $T = 0.20$, $P = 0.0$ and $\alpha = 0.75$.

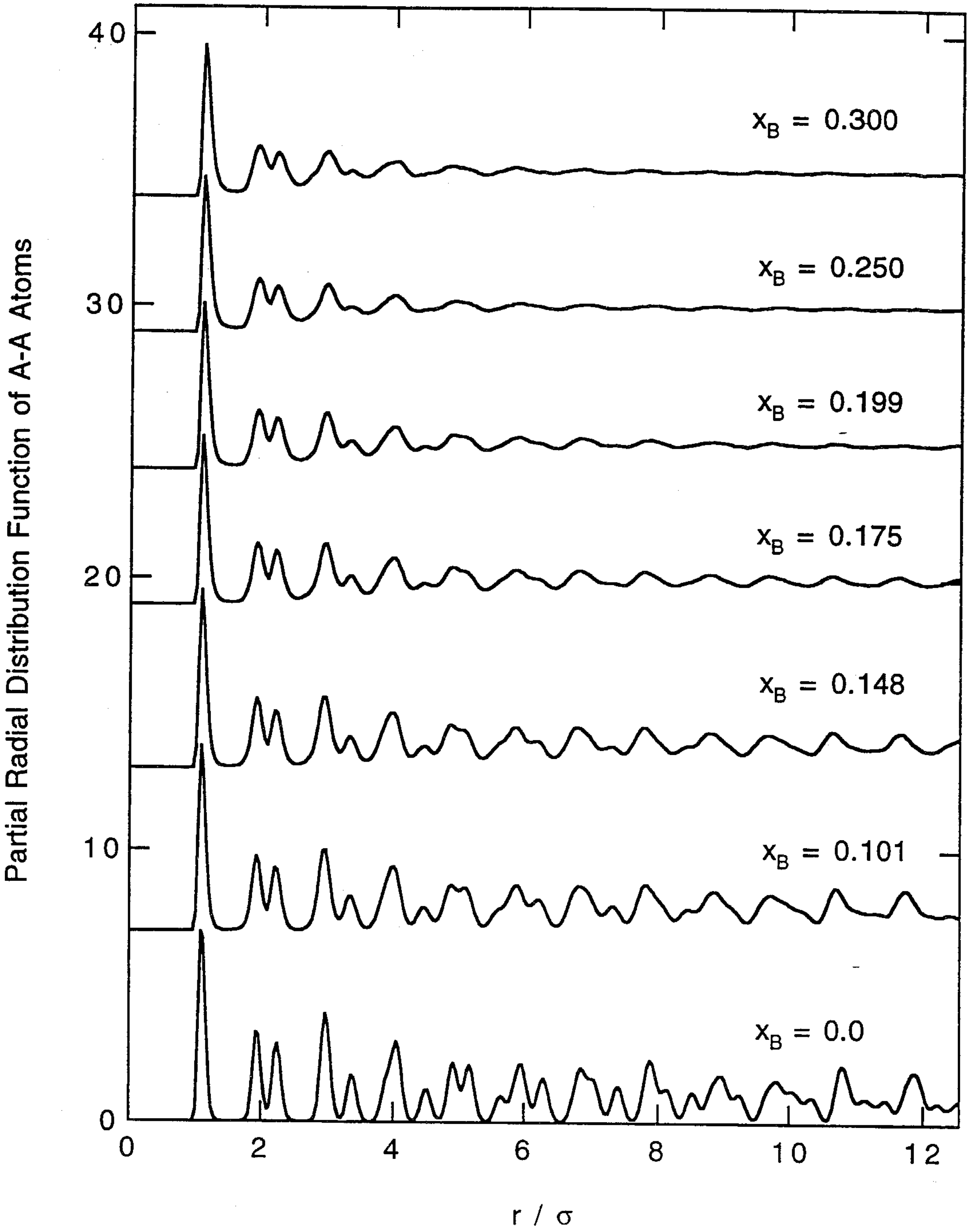

Fig. 5.3 (b) Partial radial distribution functions of solvent-solvent (A-A) atoms for the two-dimensional solid solution at $T = 0.20$, $P = 0.0$ and $\alpha = 0.75$.

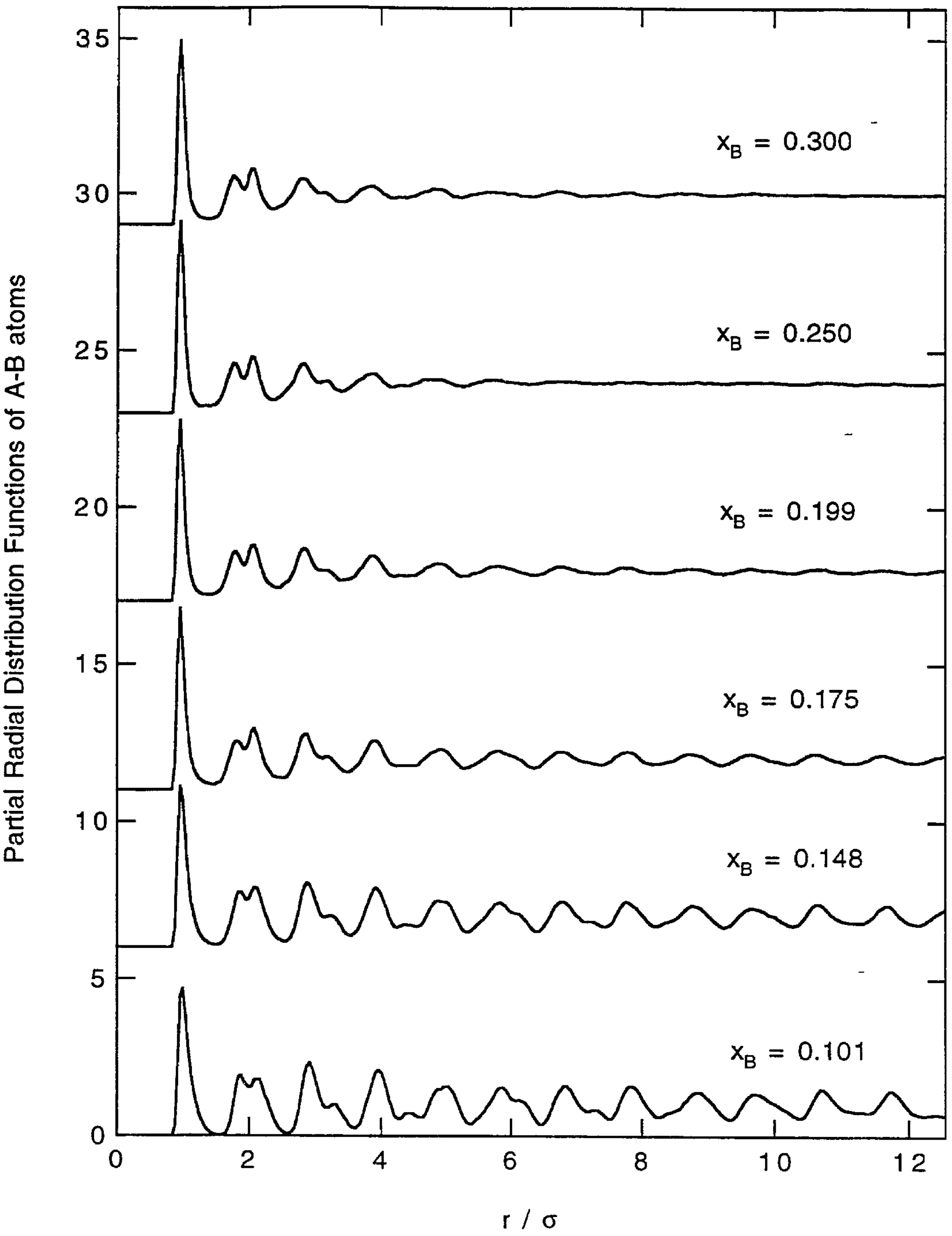

Fig. 5.3 (c) Partial radial distribution functions of solvent-solute (A-B) atoms for the two-dimensional solid solution at $T = 0.20$, $P = 0.0$ and $\alpha = 0.75$.

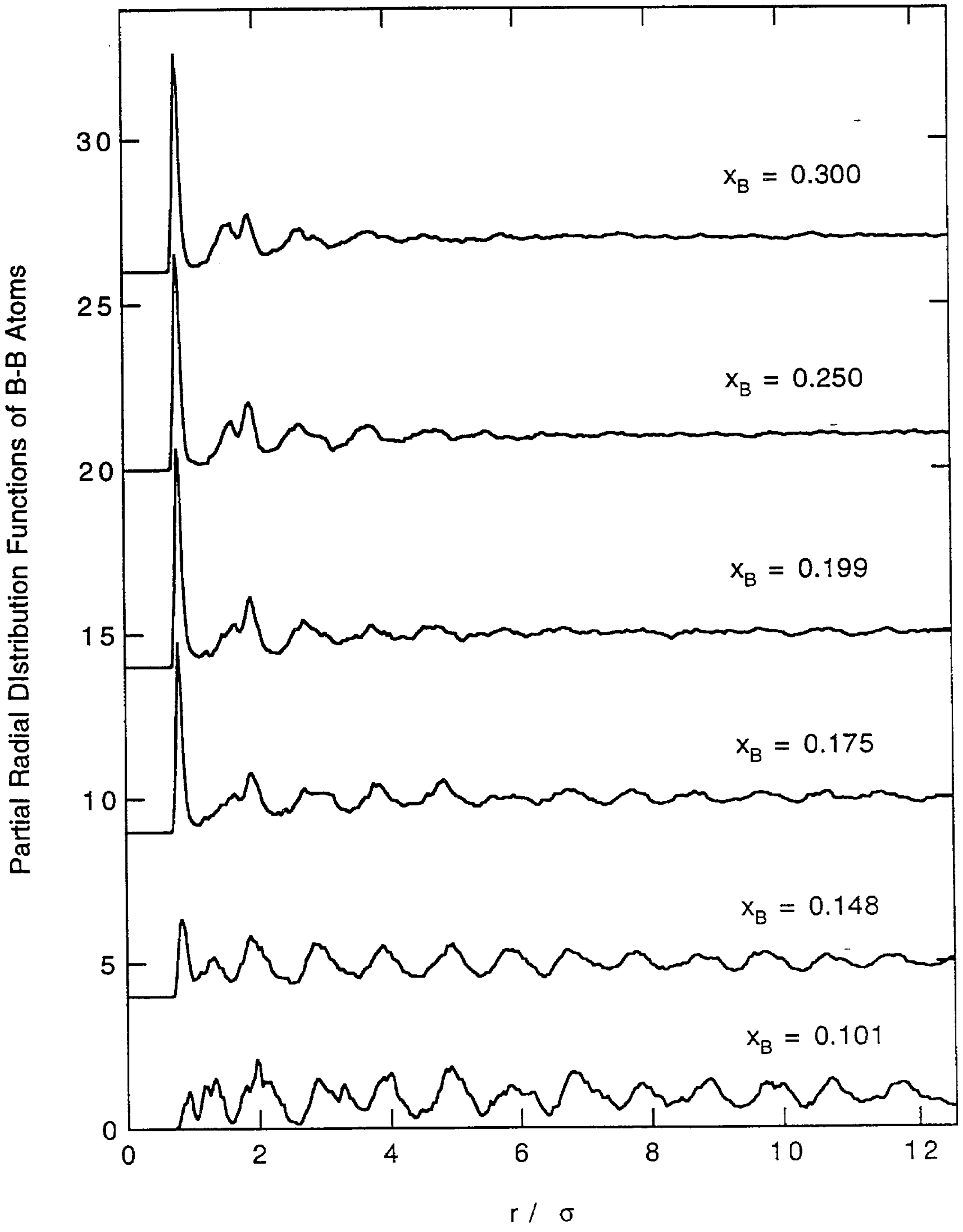

Fig. 5.3 (d) Partial radial distribution functions of solute-solute (B-B) atoms for the two-dimensional solid solution at $T = 0.20$, $P = 0.0$ and $\alpha = 0.75$.

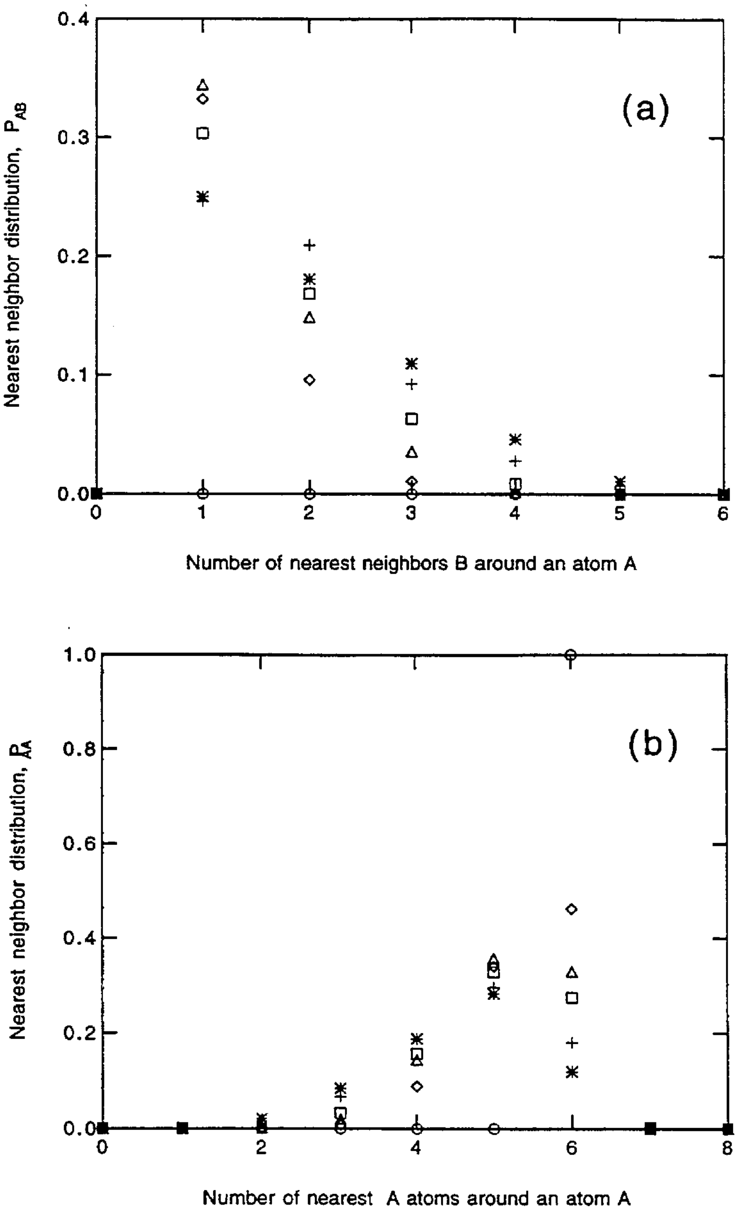

Fig. 5.4 **(a)** Probability distribution of B atoms around an A atom; **(b)** Probability distribution of A atoms around an A atom, for a two-dimensional hexagonal binary solid solution at $T = 0.20$, $P = 0.0$ and $\alpha = 0.75$. Circle: $x = 0.0$, diamond: $x = 0.101$, triangle: $x = 0.148$, square: $x = 0.176$, cross: $x = 0.25$ and asterisk: $x = 0.30$.

Detailed, quantitative results will be given in the next section.

(1) Topological disordering, represented by atomic displacements as defined in Eqs. (4.4 -7), is caused by local relaxation of size-mismatched atoms. The displacements occur gradually and have small amplitudes.

(2) Such displacements are very localized before the CGT occurs. Once they form, they will be limited to the regions, usually within the nearest neighbor shells, and will not spread substantially as the time goes on.

(3) The sizes of disordered regions largely depend on the average solute composition. But even for a fixed composition, it varies from a few atomic spacings to relatively large clusters of hundred atoms. Such disordered regions have different geometrical shapes, but most frequently they adapt the shape resembling networks of rivers.

(4) Ordered regions are separated by these disordered networks and are preserved even in the amorphous phase which form at very high solute concentrations. Their sizes and relative orientations will change gradually. These "crystalline-like" cluster regions will eventually decrease in number and lose their orientational correlations in the amorphous phase.

(5) There are more solute atoms in the disordered regions.

(6) The "interface" between the ordered and disordered regions is not clearly distinguishable, especially in the samples with compositions close to that of the CGT. In fact, the more solute atoms are added, the more blurred these boundaries become.

At low solute concentrations, these disordered regions look like "grain" boundaries that separate ordered regions, but when more solute atoms are added, these regions get bigger. Very close to the CGT and in the amorphous phase, these microconfigurations can no longer be defined as "imperfections" such as grain boundaries.

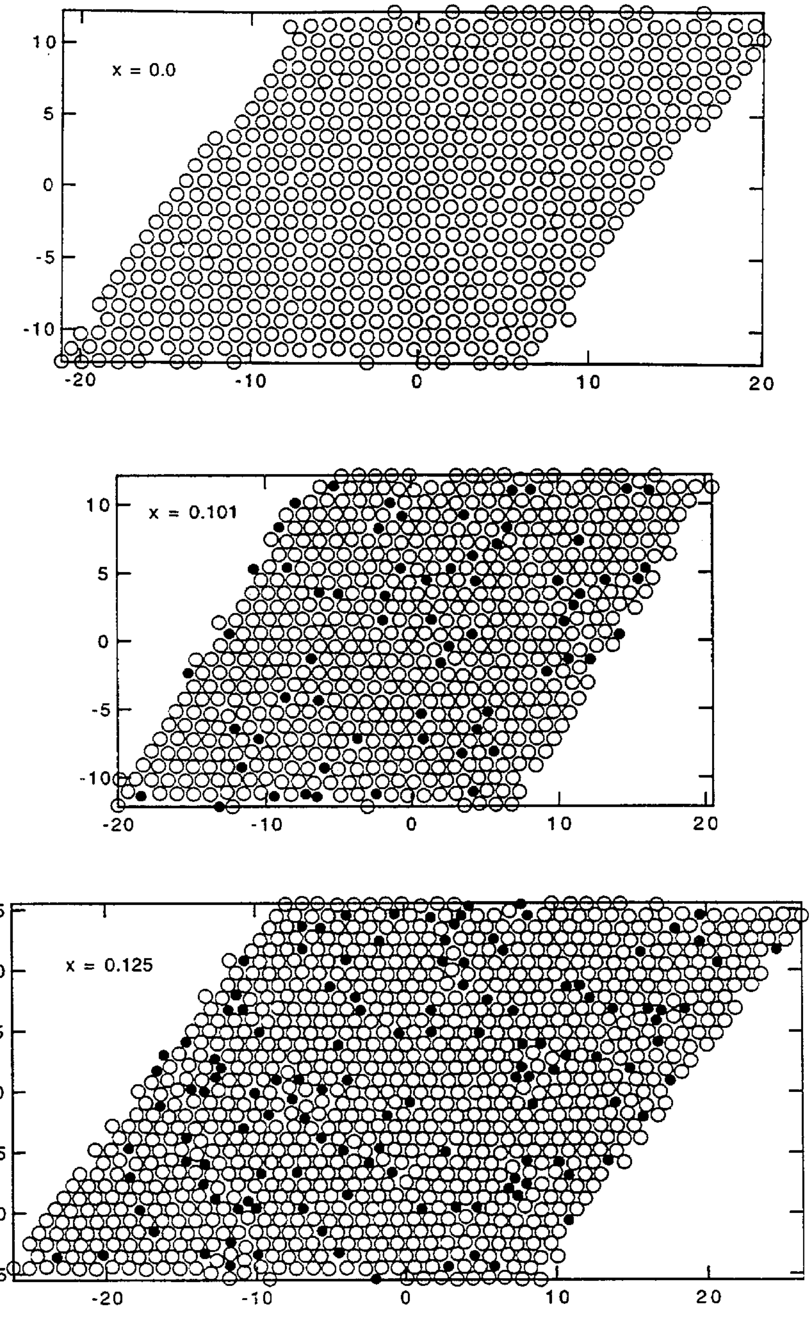

Fig. 5.5 Snapshots of equilibrium atomic configurations of the two-dimensional solid solutions. Circle (o) denotes solvent atom and filled circle (•) represents solute atoms. The atomic size ratio is 0.75.

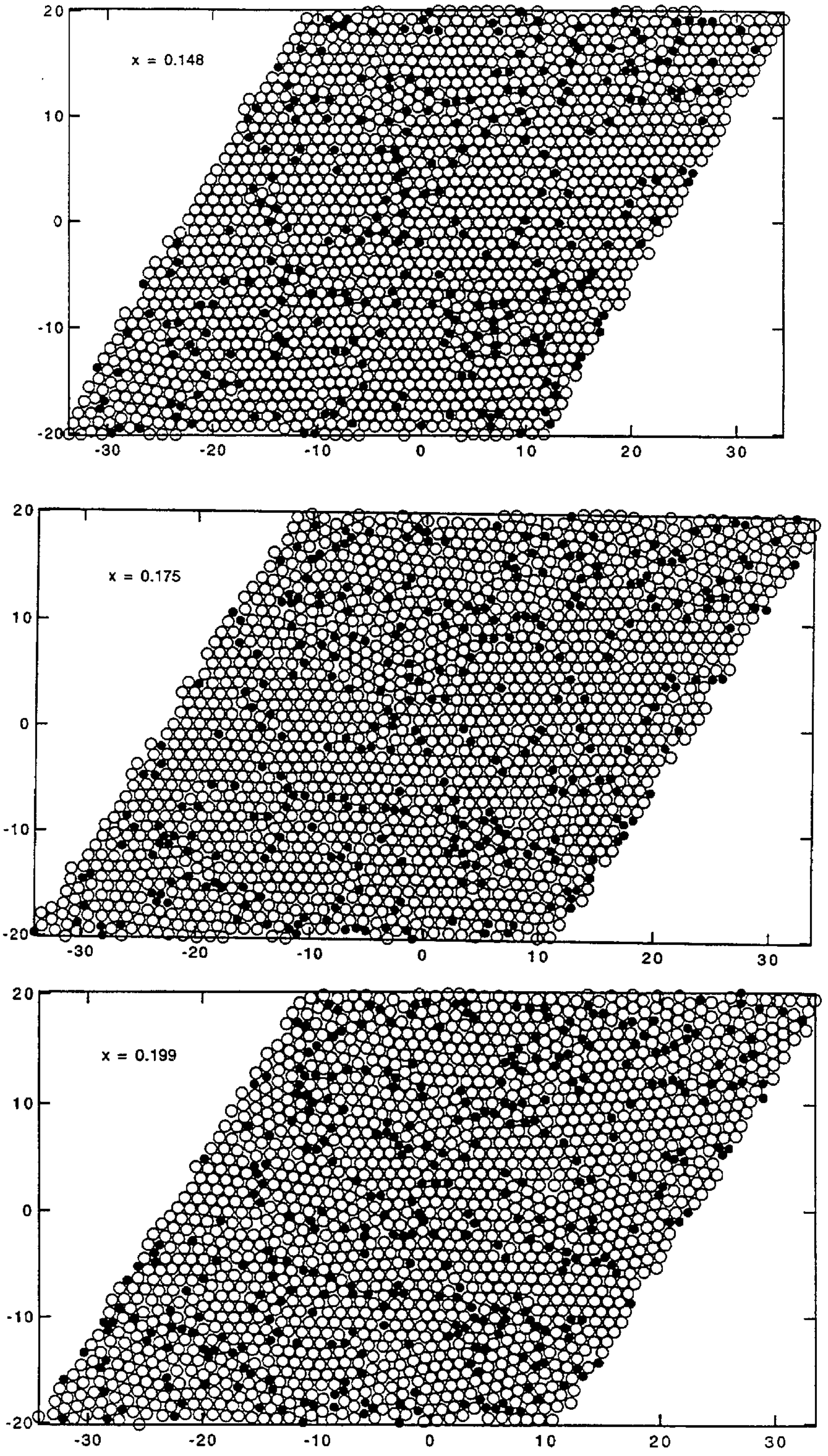

Fig. 5.5 (continued) Snapshots of equilibrium atomic configurations.

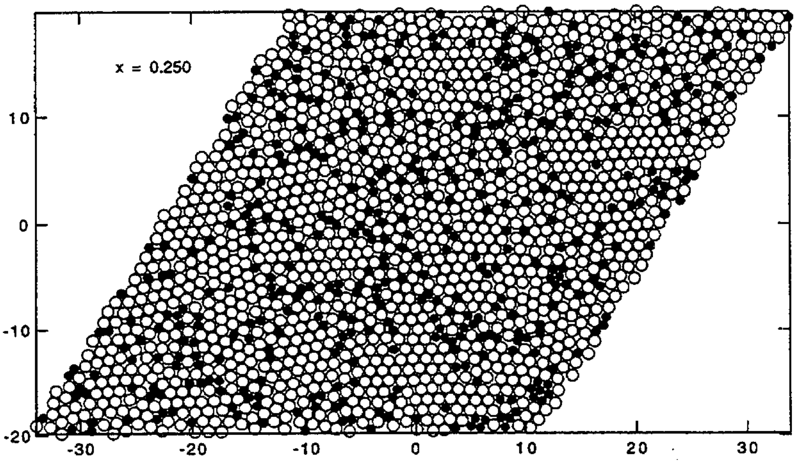

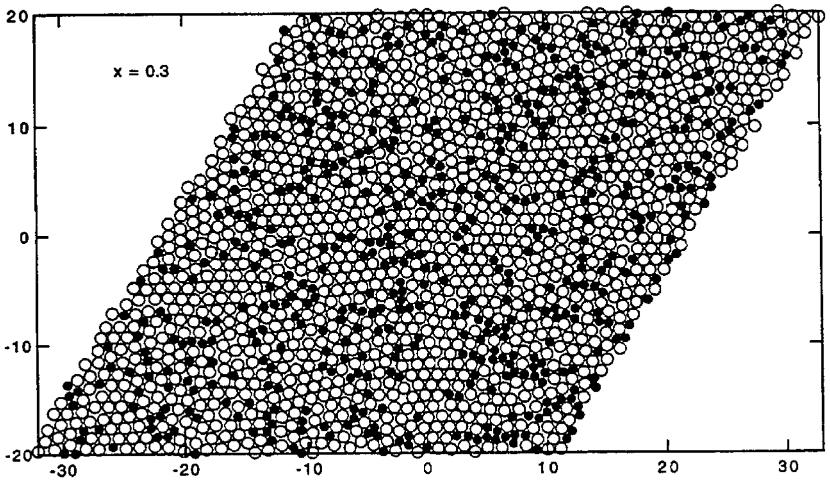

Fig. 5.5(continued) Snapshots of equilibrium atomic configurations.

but instead, they are an essential part of the landscape. Note such boundaries are not sharp, especially at the later stages of disordering. As the solute concentration increases, more and more disordered regions appear and at the same time the boundaries of the disordered/ordered regions become more diffuse. Finally when disordered regions begin to percolate throughout the entire sample, the CGT occurs. It is interesting to note that the entire process proceeds in a smooth and gradual manner, which is in striking similarity to that of a system undergoing a continuous phase transition [5.10].

These intriguing features can be analyzed in more quantitative ways to reveal more detailed information about the microscopic structural changes. In particular, the role that defects play in the topological order to disorder transition can be perceived more clearly with the help of such analysis. These results provide useful information on how and why the local relaxation and disordering occurs around the mismatched atoms. This will be the task of several of the following sections.

5.4 Defects, Translational and Orientational Symmetry

In chapter 4, we mentioned that it is the local atomic relaxation from mechanically unstable configurations caused by two different atomic sizes that directly results in the topological order to disorder transition. The local atomic configurational rearrangement involves the coordination number change. They can lead to formation of topological defects. These topological defects can be characterized by topological defect configurations using the technique discussed in chapter 2. Thus the analysis of defects and its effect on long-range translational and orientational symmetry can provide us with detailed microscopic information on how the CGT occurs. In this section we shall present the configurations of various topological *defects, and discuss their relations with the symmetry changes.*

As pointed out by Nelson et al. [5.11], a crystalline phase is characterized by not only the long-range translational symmetry, but also orientational symmetry. These two different aspects of long-range order in crystalline phases are closely related. Disruption of translational symmetry in general will not disturb the orientational symmetry. If long-range orientational symmetry is broken, so is the translational symmetry. Such an argument had motivated Nelson et al. [5.11] to propose a new phase that is characterized by long-range orientational symmetry and short-range translational symmetry. They called it "hexatic phase" adopted since it is formed from a hexagonal lattice. For a two-dimensional solid, these symmetries can be quantitatively expressed by translational and orientational order correlation functions defined in (2.3-8). From the behavior of these correlation functions with distance, information about the degree of disordering, spatial scale of the correlations of the ordered phase and relationship between disordering and defects can be analyzed quantitatively.

A perfect two-dimensional crystalline solid has quasi-long-range translational symmetry. Its correlation function decays algebraically [5.11],

$$C_{\vec{G}}(r) = <\rho_{\vec{G}}(r)\rho_{\vec{G}}(0)> \sim r^{-\eta}, \tag{5.2}$$

where η is the exponent for the power-law decaying function. $1/4 \leq \eta(T_m) \leq 1/3$ at the melting temperature T_m. From the relation (2.25), the Bragg diffraction peak of the shortest reciprocal vector $\vec{G}$ of such a two-dimensional crystal is no longer a delta function, but exhibits a power-law decay. The orientational symmetry, on the other hand, is long-ranged. Its correlation function, as defined in (2.27), is a constant.

Long-range translational and rotational symmetry defined by (2.23) and (2.26) and their correlation functions defined by (2.24) and (2.27), are extremely sensitive to crystalline defects, especially to those of a topological nature that can effectively disrupt the long-range symmetry [5.11]. Point defects can destroy neither long-range translational nor orientational symmetry, unless they form certain types of extended complexities such as dislocations. Topological defects, such as dislocations, disclinations and grain boundaries, can disrupt both kinds of long-range symmetry effectively, but the sensitivity of each type of long-range order varies with different defects.

In two dimensions, an edge dislocation is defined as a defect represented by a missing or an extra row of atoms (see 2.6 for details). The elastic energy associated with the dislocation disorder is long-ranged [2.21, 3.1], so two dislocations with opposite Burgers vectors are usually paired up to reduce this energy. At low temperature, dislocation pairs are the most frequently encountered topological defects. Other types of topological defects such as disclinations can also disrupt translational symmetry by rotating different parts of a crystalline phase with respect to others, but because the formation energy is much higher than that of dislocations, they seldom occur and do not affect crystallinity at relatively low temperature.

As the disordering progresses, defect density will increase and the defect configuration will change too. Ignoring defect-defect interactions, one would expect that the dislocation-pairs become unstable against thermal agitation. If the activation energy is higher than the binding energy, the pairs eventually break into two singlets. Once this occurs, the long-range translational order will be destroyed completely, but the long-range orientational order will be intact. This phase is thus *characterized by long-range orientational order and short-range translational order.* It is termed the "hexatic" phase. The Burgers vector associated with each dislocation can cause a phase shift in the translational order parameter across the extra or missing atomic plane. In general the Burgers vector is not an integral number of the lattice spacings, so the phase shift will lead to a decrease of the translational order correlation.

In order to have a topologically disordered phase with neither long-range translational symmetry nor long-range orientational symmetry, further disordering is needed. If the excitation energy is large, the single dislocations in the intermediate "hexatic" phase can be broken down further into the single disclinations which form the dislocation. Once again this can occur only when there are no other competing processes, or no defect interactions present.

In fact, this simple argument led Kosterlitz and Thouless, [5.12] and later, Nelson and Halperin [5.11], to propose a theory of melting in two dimensions. They assume that two-dimensional melting is caused by dislocation-pair unbinding into single dislocations at melting, T_m, where long-range translational order is destroyed, but orientational order is left intact. This will result in the intermediate phase, the hexatic phase. At a higher temperature, $T_i(> T_m)$, single disclinations will be generated from these single dislocations, thus destroying the orientational order. Only at this second stage ($T \geq T_i$) does the system becomes a true isotropic liquid.

At the intermediate stage ($T_m < T < T_i$) where the translational order is short-range, but the orientational order is quasi-long-range. The orientational order correlation function behaves in a power-law fashion,

$$C_m(r) = < \psi_m(r)\psi_m(0) > \sim r^{-\xi}, \tag{5.3}$$

where ξ is the exponent for the power-law decay of $C_m(r)$. $\xi(T_i) = 1/4$ at T_i when single disclinations form. As we learned in 2.6, a disclination is the defect that consists of a group of extra, or missing, atoms that form a 60° angle wedge. Across such the defect, the nearest neighbor atomic bond will be rotated. The disclination is primarily responsible for destruction of the long-range orientational order, but it can also reduce the long-range translational order. When the single disclinations proliferate, the orientational order will be destroyed. Thus in a true liquid state, or an amorphous state, both correlation functions decay exponentially.

In fact, interactions between these topological defects cannot be neglected. As we show later, they can be effective even with the very moderate density of defects. They must be taken into consideration in the topological order to disorder transition. The collective motion and correlation between the elementary defects (dislocations, disclinations, dislocation pairs, and disclination pairs, etc.) can play a dominant role in disrupting both long range order.

One type of the collective defect is the grain boundary-like network. Relative crystalline orientations are different in adjacent "crystalline-like" regions across such a boundary. A grain boundary-like, or collective defect, can not only destroy translational order but also orientational order (see Fig. 2.3). The degree of disordering across a grain boundary depends on the density and the orientations of the dislocation arrays that make the boundary. In most cases, the collective defects are more energetically favored than the elementary defects, thus making them extremely important in destabilization of crystalline order.

There is an important difference between collective defects and a true grain boundary. A grain boundary defined as a crystalline imperfection is characterized as a *localized* defect with relatively *low density*. However, when it becomes delocalized and occupies a large portion of the total volume or area comparable to that of the crystalline regions, it can no longer be regarded simply as a grain boundary. In addition, the collective defects are not connected below certain solute concentrations, while a grain boundary is always connected, forming a closed loop in two dimensions. By no means, therefore, can the collective defects be regarded as grain boundaries. They are *microscopic* defects characterized by chemical (solute concentration) as well as configurational (atomic displacement) inhomogeneities on microscopic scales.

Nevertheless, the role elementary and collective defects play in destruction of the long-range symmetry in the melting transition are equally important in our analysis of the CGT because the defects, though not generated from thermal excitations, are responsible for the transition [5.12]. Because of the low temperature constraint, one could observe the different stages of the transition and the different behaviors of symmetry correlations, and the different defect configurations. In the remainder of this section, we shall correlate the behavior of the order correlation functions with defects present in the two-dimensional binary solid solutions.

Fig. 5.6 and 5.7 show the translational and the orientational order correlation functions of the binary solid solution at different solute concentrations. It can be seen clearly that in the pure LJ hexagonal phase, where $x = 0$, the translational order correlation function decays algebraically. The correlation length is thus quasi-infinitely long. For comparison, see Fig. 5.7 where the orientational correlation function for the pure LJ crystalline phase is a constant. At this low temperature, there are no imperfections present in this system. The algebraic decay of the translational order correlation function is simply caused by thermal vibration.

Further increase of the solute concentration results in two different behaviors of the correlation functions (see Fig. 5.6 (b)). In the composition range, $0.0 < x < 0.199$, the translational order correlation function decays algebraically with distance and the correlation length over which the atoms still maintains their translational order is quasi-long ranged. At $x \geq 0.199$, the atoms have lost their long-range translational correlation. The correlation length of the solid solutions at this composition range is approximately on the scale of the third and fourth nearest neighbor distance, which agrees quite well with the crystalline sizes presented in Fig. 5.5.

The orientational order correlation function behaves rather differently (see Fig. 5.7(b)). At the composition range, $0.0 < x < 0.199$, it decays algebraically and is quasi-long-range. At higher compositions ($0.199 < x < 0.30$) where the translational order correlation function becomes short ranged, it still maintain a persistent, nonzero value at distance. This behavior of the orientational correlation function persists until the solute composition reaches $x \geq 0.30$. Beyond this point, the long-range orientational correlation becomes short-ranged with a correlation length of the same scale as that of the translational correlations in the amorphous phase.

We can observe this behavior also from the local, average translational order parameter (TOP) and orientational order parameter (OOP). They are defined as follows.

$$TOP = \frac{1}{N}\sum_{i}^{N} \rho_{\vec{G}}(r_i), \tag{5.4}$$

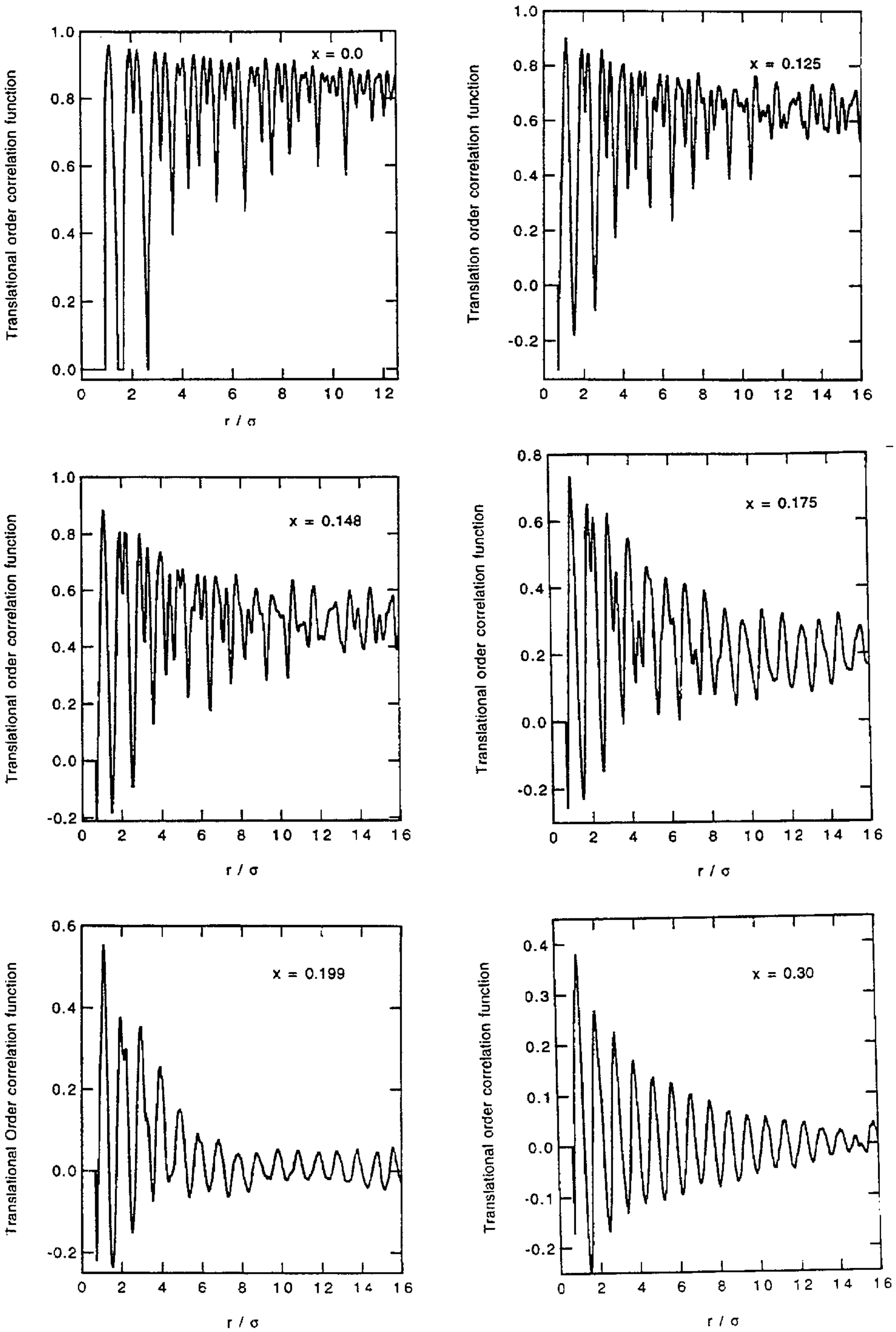

Fig. 5.6 (a) Translational order correlation functions of the two-dimensional solid solutions.

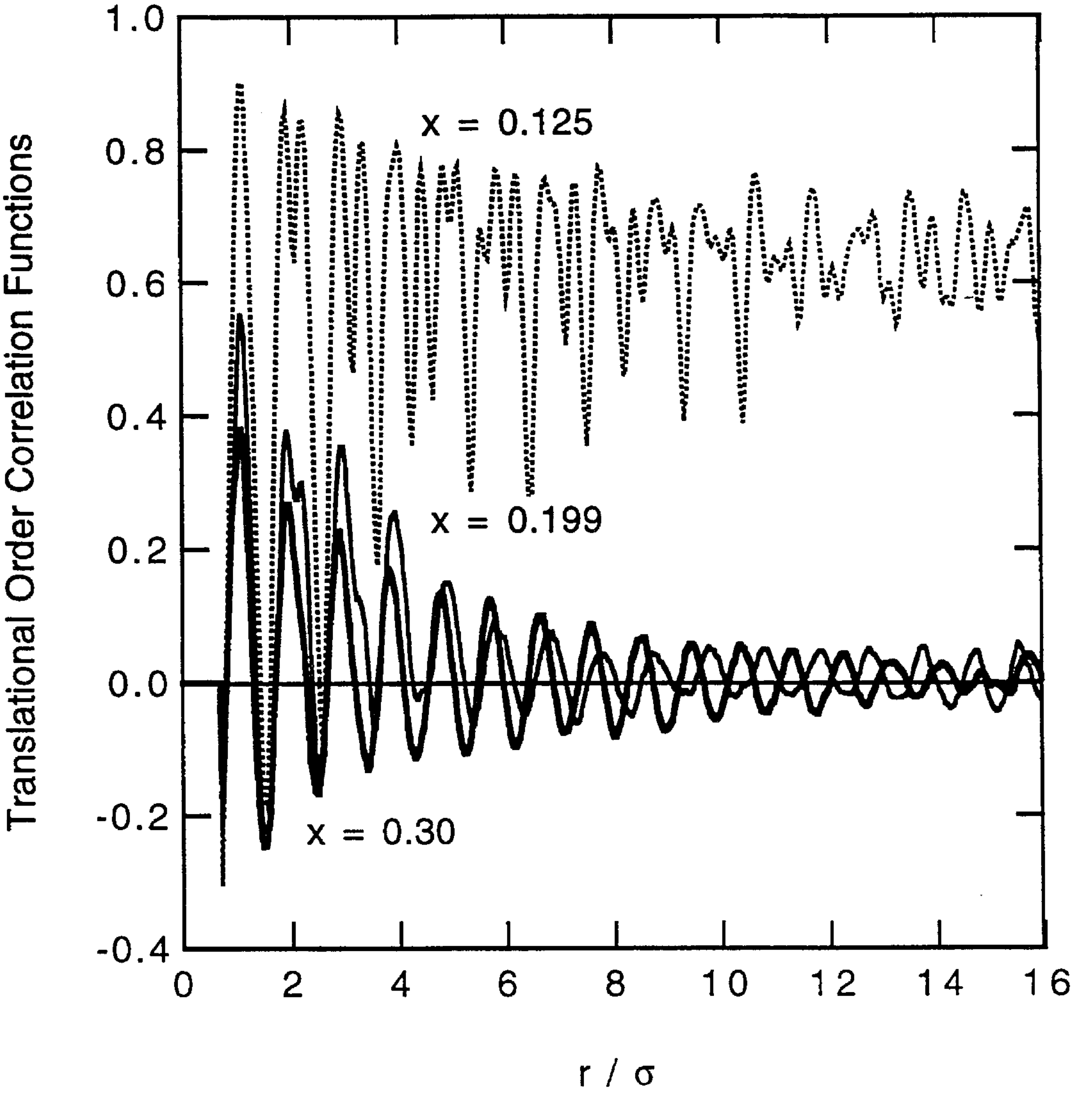

Fig. 5.6 (b) Translational order correlation functions of the crystalline phase (dashed line), intermediate phase (solid line) and amorphous phase (thick line).

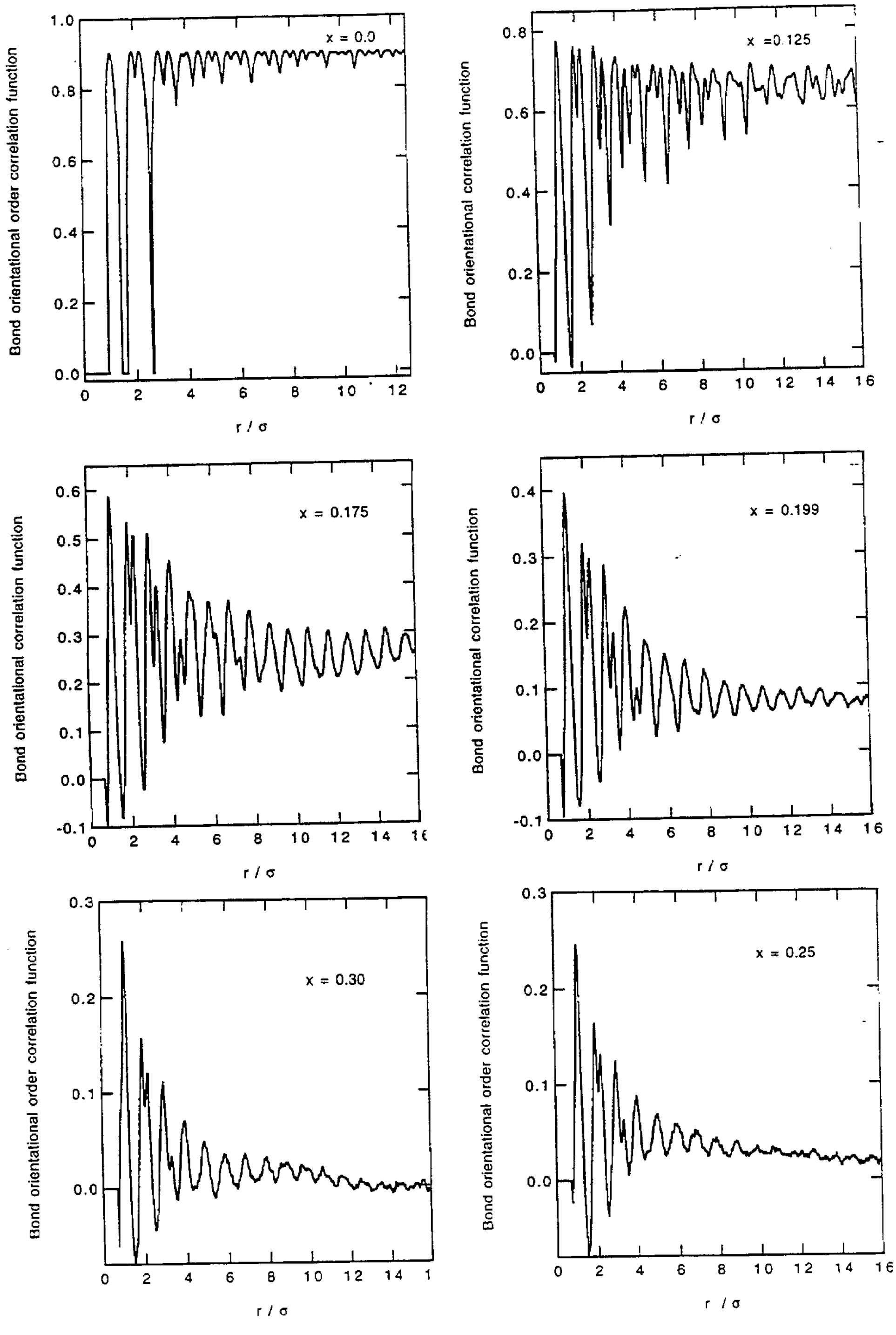

Fig. 5.7 (a) Bond orientational order correlation functions of the two-dimensional solid solutions.

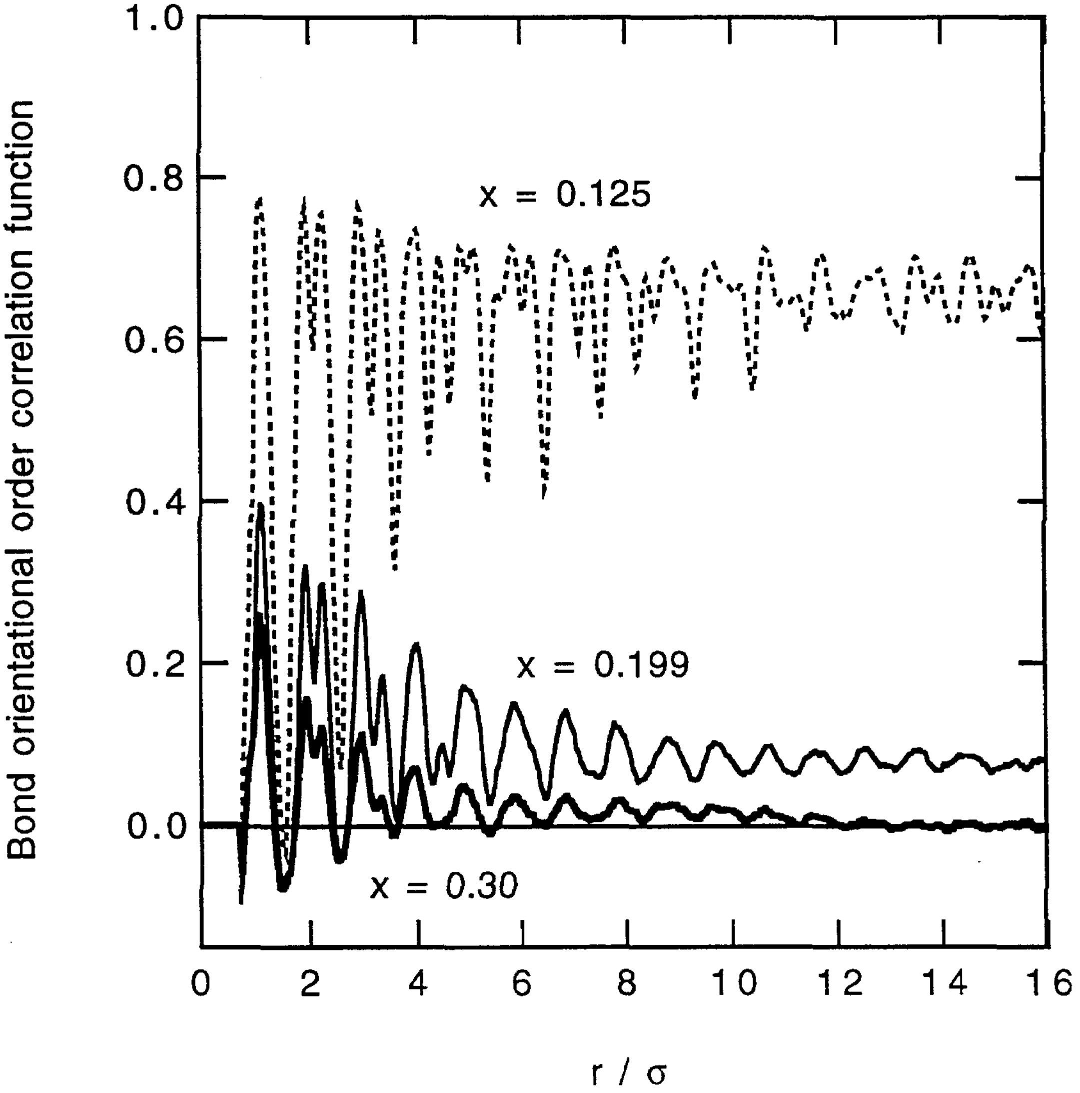

Fig. 5.7 (b) Bond orientational order correlation functions of the crystalline phase (dashed line), intermediate phase (solid line) and amorphous phase (thick line).

and

$$OOP = \frac{1}{N}\sum_{i}^{N}\Psi(r_i), \tag{5.5}$$

where $\rho_{\vec{G}}$ is defined by Eq. (2.24). $\Psi(r_i)$ is the averaged bond orientational order parameter associated with the ith atom over its nearest neighbor atoms,

$$\Psi(r_i) = \frac{1}{N_{nn}}\sum_{j}^{N_{nn}}\psi_m(r_j), \tag{5.6}$$

where ψ_m is given by Eq. (2.27) and N_{nn} is the number of its nearest neighbor atoms. Fig. 5.8 shows the averaged TOP and OOP defined above. The average TOP exhibits an abrupt decrease at $0.148 < x < 0.199$ and almost approaches zero at $x = 0.199$ where amorphization was observed to occur. The OOP drops in the same fashion as that of the TOP at $0.148 < x < 0.199$, but begins leveling off at $x > 0.199$. *The finite value of the OOP in* $0.199 < x < 0.30$ *defines an intermediate* region resembling that of the hexatic phase [5.11].

However, defect configurations presented in Fig. 5.9 for the two-dimensional binary solid solutions in the intermediate region do not reveal any significant increase in the number of single dislocations or disclinations. Instead density of the dislocation pairs increases rapidly. As their density increases, the collective defects become entangled as more solute atoms are added. As Fig. 5.9 shows, they start forming networks at higher solute concentrations. The collective behavior of dislocation pairs results directly from the mutual interactions between the pairs to lower the elastic energy associated with the defects [5.13]. Obviously the collective defects formed from the dislocation pairs preempt the formation of single dislocations, leading to the absence of unbinding of the dislocation pairs.

The peculiar morphology of the collective defects can be explained by the

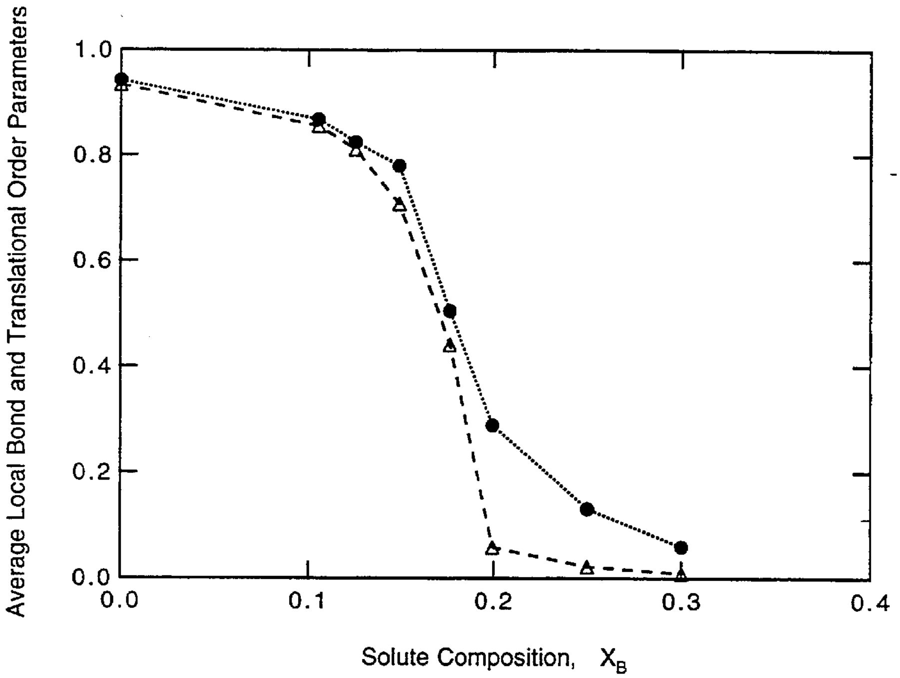

Fig. 5.8 Average local bond orientational (filled circle) and translational (triangle) order parameters of the two-dimensional solid solutions.

anisotropic stress field of an edge dislocation. Fig. 5.10 (Top) shows the force field between two parallel edge dislocations with parallel Burgers vectors. The equilibrium positions of the dislocation configuration are shown in Fig. 5.10 (Bottom). By forming a dislocation pair, a dislocation can reduced the anisotropic stress field at large distance. If more dislocations are present, they can be attracted to align on top of the pair by the residual force, thus forming the network structure.

It should be pointed out that the clustered dislocation pairs are caused by only local atomic arrangements, because the low temperature constraint does not permit the large-scale relaxation. They are essentially "frozen". On the contrary, the networks formed during thermal melting result from large scale atomic rearrangement assisted by long-range diffusion motion and large amplitude thermal vibration.

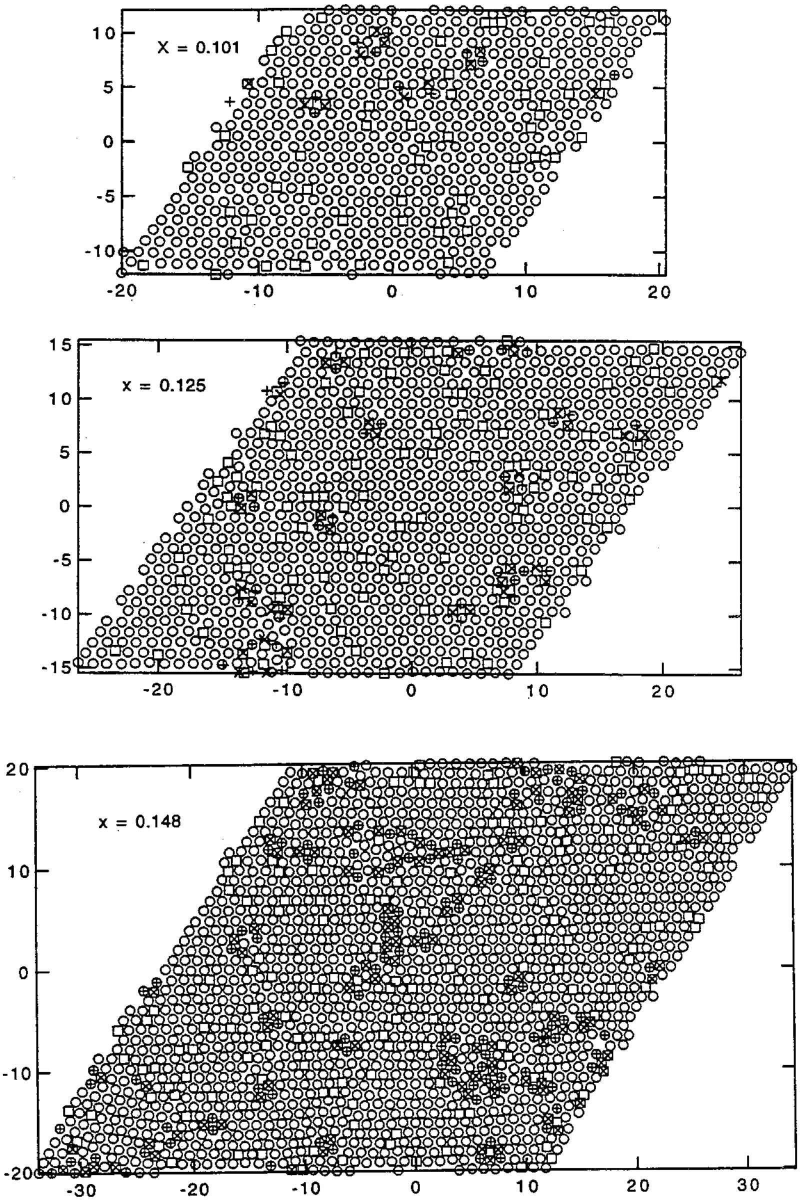

Fig. 5.9 Snapshots of atomic configurations of defects (dislocations and disclinations) of the two-dimensional solid solutions. In order to have a better view, we plot the solvent atoms as circles and solute atoms as squares. Atoms with 4 nearest neighbors are represented as triangles, 5 nearest neighbors as cross and 7 nearest neighbors as plus signs.

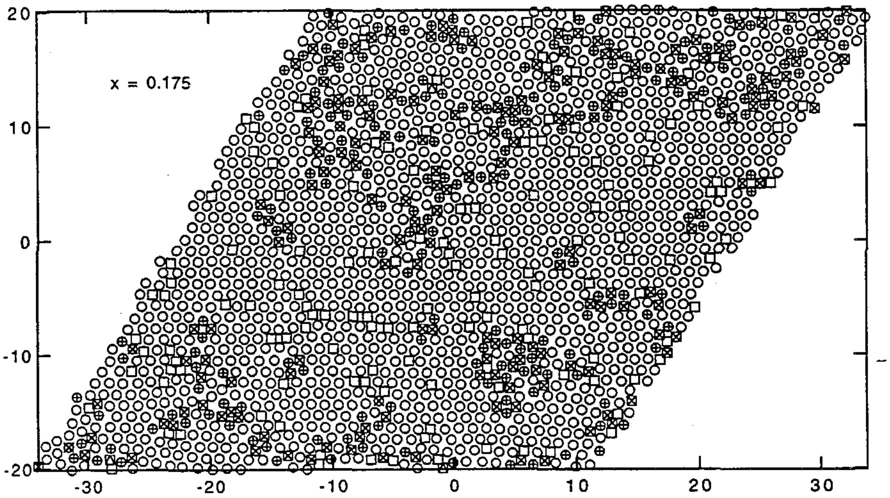

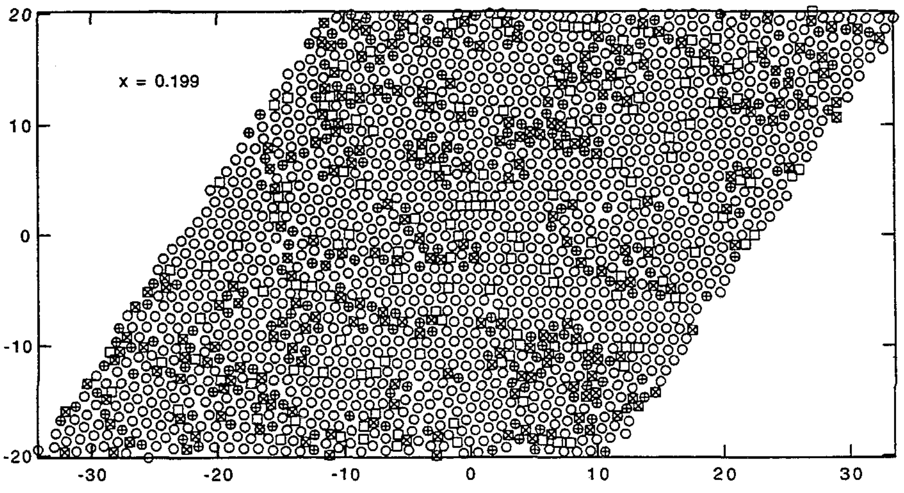

Fig. 5.9 (continued) Snapshots of atomic configurations of defects (dislocations and disclinations) of the two-dimensional solid solutions.

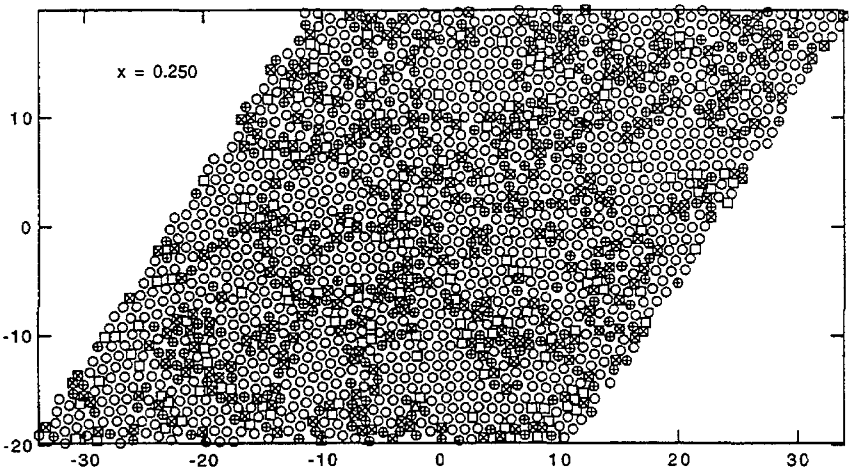

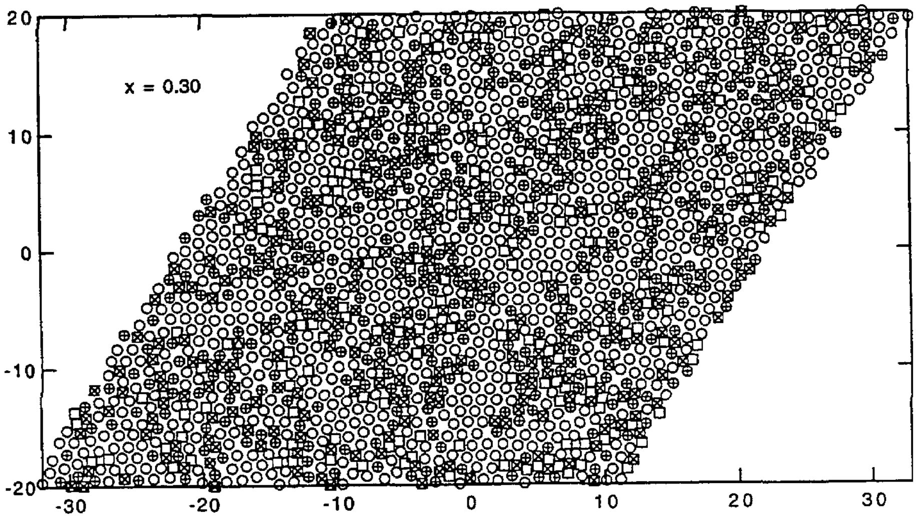

Fig. 5.9 (continued) Snapshots of atomic configurations of defects (dislocations and disclinations) of the two-dimensional solid solutions.

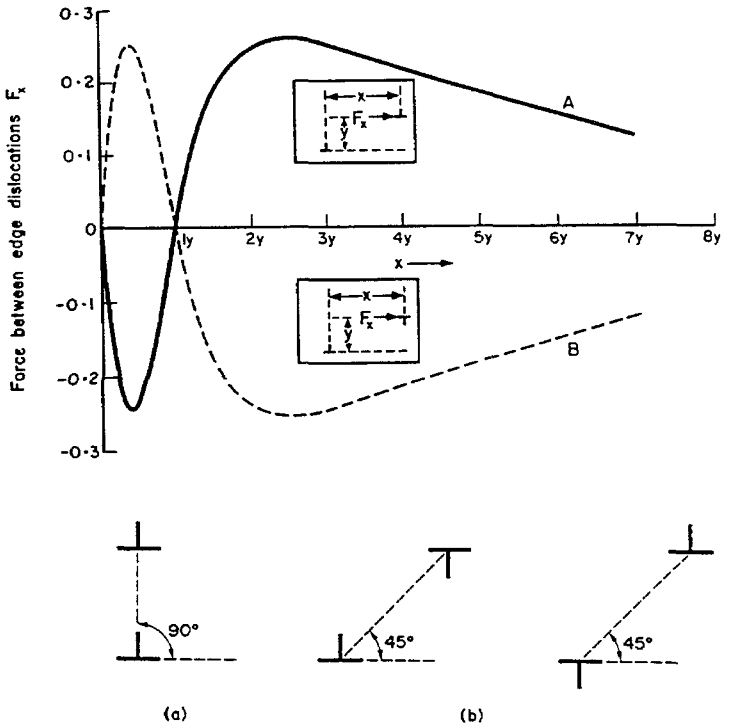

Fig. 5.10 *Top*: Forces between two parallel edge dislocations with parallel Burgers vectors. Unit of force is in $Gb^2/2\pi(1-\nu)y$, where G, b, ν are shear modulus, Burgers vector and Poisson's ratio respectively. Solid line is for like dislocations and broken line for unlike ones. *Bottom*: Stable positions two edge dislocations of the same sign and opposite sign (from Rdf. 5.15).

The total defect density is presented in Fig. 5.11, which sums up the total number of atoms that are topological defects. The majority of defects were found to have 5 and 7 nearest neighbors. We have never found 8 nearest neighbor defects. A few 4 nearest neighbor defects were found in the metastable crystalline phases at compositions very close to the CGT and in amorphous phases.

The defect density increases slowly, almost linearly at the crystalline phase. It starts to increase at around $x = 0.148$ and becomes saturated around $x \geq 0.199$

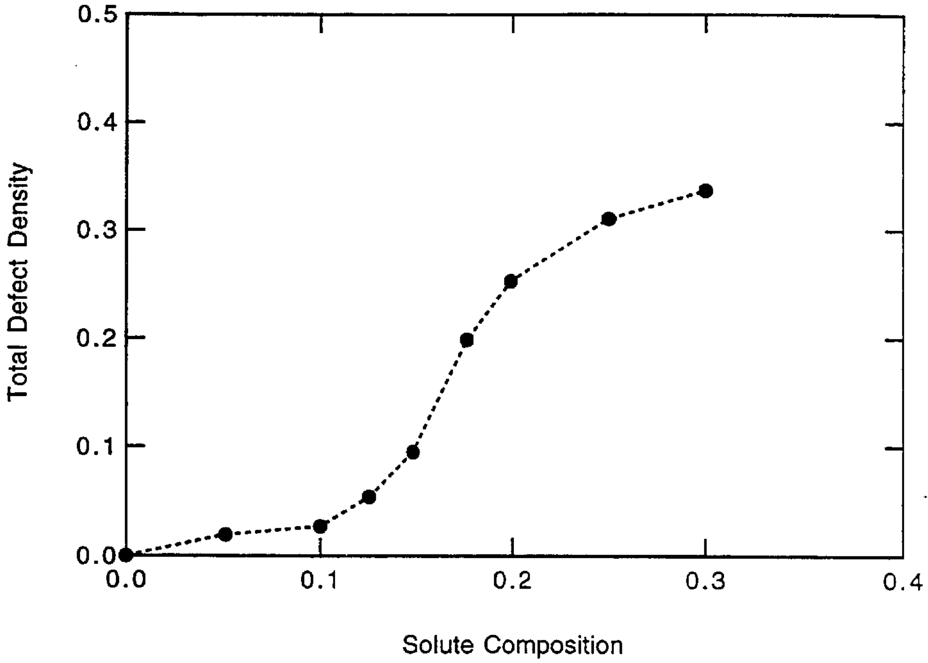

Fig. 5.11 The average total defect density. Most defects are composed of 5- and 7-nearest neighbor disclinations.

where the amorphous phase was observed to form. It is very intersting to note that the fashion of how the defect densities vary as the CGT and melting are approached. The defect density in two-dimensional LJ solids increases only slightly in the case of melting, usually from zero to 10 at. % close to melting. Then it increases abruptly at melting [5.14, 4.11]. The saturation defect density for the solid solution undergoing the CGT can reach 35 ~ 39 at.%, while that for melting is only 10.0 at.% [5.22, 4.11].

Although the behavior of the short-range translational order and the quasi-long-range orientational order in the intermediate stage of the CGT coincides with that predicted by the two-dimensional melting theory, the underlying microscopic defects that are responsible for this behavior are totally different. The dislocation pairs do not unbind into isolated dislocations, instead, they tend to connect to each other. Such networks formed by the dislocation pairs can effectively disrupt both translational and orientational symmetry. The atomic configurations shown in Figs. 5.5 clearly show the patches of crystalline regions that are rotated. We conclude that it is the *total number of defects* and the *microscopic configurations* that are primarily responsible for the CGT as well as melting.

The non-dislocation unbinding mechanism can be tested also by examining the dislocation pair coupling constant [2.21, 3.14, 5.11], or Kosterlitz-Thouless constant [5.12], which is expressed as a combination of two elastic constants, $\mu = C' = C_{44}$ and $\lambda = C_{12}$,

$$K = \frac{4a^2}{k_B T} \frac{\mu(\mu + \lambda)}{(2\mu + \lambda)}, \tag{5.7}$$

where a is the lattice parameter and T is the temperature of the system. If the dislocation pair unbinding occurs, K will approach the universal value 16π as predicted by the theory from renormalization group approach [5.11]. Instead it remains above this value (Fig. 5.12) when the long-range translational order disappears at $x = 0.199$ and begins leveling off at $x > 0.199$. In fact, we can attribute the large decrease of the dislocation coupling constant to the screening effects caused by increasing populations of dislocation pairs. Exactly as argued by Nelson [5.11], it is the new *dislocation pairs* generated by addition of solute atoms that can "block" or shield the elastic stress field between two existing dislocation pairs, thus reducing their couplings.

The shape that these collective defects adopted is not strictly linear. They form networks with finite, diffusive width. These networks remain isolated before the CGT, but begin to percolate through the system at/after the CGT. They mean-

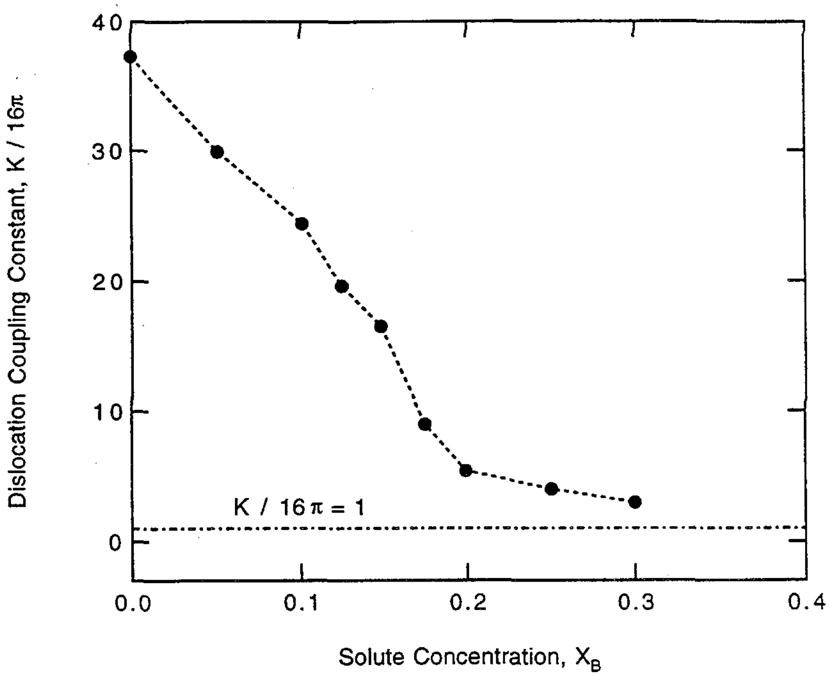

Fig. 5.12 Dislocation-dislocation interaction constants, or Kosterlitz-Thouless constant, K, as a function of solute composition. The dashed line is the universal value of 16π.

der through the entire sample and as a result, they partition the crystal into pieces each of which still retains the crystalline feature. The size of each "crystalline-like" region separated by the networks is determined by the correlation length of the translational order correlation function. The sizes and orientations of these "crystalline-like" clusters vary significantly. As the solute concentration increases, they become smaller and more misaligned. The network density as well as its thickness also increase with the increase of the solute concentration.

Apparently this type of special microstructure formed by a collection of dislocations is directly responsible for destroying the long range translational and orientational symmetries. Within the networks of the diffuse collective defects, the atoms completely lack *translational and orientational order. But in general the* orientations of the nearest neighbor atomic bond in the adjacent crystalline clusters separated by the disordered networks vary relatively slowly compared with that of the translational order. This explains the persistent behavior of the orientational order.

As the solute concentration increases further to $x = 0.30$, both orientational correlation functions start decaying exponentially. The corresponding correlation lengths reduce to only the third or fourth nearest neighbor distances. The detailed atomic configurations in Fig. 5.5 and Fig. 5.9 show that the dislocation networks become truly diffusive and only a small portions of the areas in the sample are still occupied by "crystalline-like" clusters. The correlation lengths of both translational and orientational order correlation functions actually coincide with the size of these clusters. Interestingly, even at this stage, we seldom observe any isolated dislocations or disclinations (see Fig. 5.9). The complete destruction of the quasi-long-range orientational order is caused by proliferation of the defect networks, not by spontaneous generation of single dislocations as predicted by the two-dimensional melting theory [5.11, 5.12].

The results presented above further confirm the role of collective defects in topological transitions such as melting and the CGT. The same phenomenon has been observed for melting transition at the much higher temperature than that for the CGT. Naturally, one does not expect that the clustering of defects can occur at such a low temperature, because thermal activation needed for the dislocation-pairs to migrate to form collective defects are not sufficient. Therefore, one might expect to have a better chance to see defect unbinding. Instead, one still observes the same *collective behavior of defects at this temperature. It suggests that the collective* defects are mainly responsible for the topological order to disorder transition.

In addition, we have never observed any point defects (such as vacancy) or any stacking fault in the crystalline solid solution at any compositions. The temperature is too low to create any thermal vacancies. Also because the configurations of point defects (such as Frankel pairs) and line defects in two dimensions are degenerate, they cannot be distinguished (see 2.6 for detailed discussions).

High density of stacking faults were reported [5.16] in a binary hard sphere solid solutions. In this experiment, two types of steel ball bearings of different sizes were used to simulate glass formation induced by defects. In addition to the same dislocations and dislocation networks found in the LJ binary solid solution, they found a large number of stacking faults. In a separate work [5.17] a similar result was reported in a binary array made of two types of hard spheres with different sizes [5.18] that was generated using Bennett's random packing model [5.18]. The stacking faults were found in a large quantity. They can retain the configurations even after a great number of violent shakings to simulate thermal annealing [5.16]. Also it was observed that the hard spheres sitting on the stacking faults possess local fourfold symmetry [5.16, 5.17], which can be observed clearly on computer generated rigid binary arrays [5.17].

The results that we obtained from the MD simulation on the binary solid solution with much softer LJ potential suggest that the stacking faults found in the hard sphere binary arrays are resulted from a combined effect by insufficient relaxation and extremely repulsive potential of the hard spheres. A stacking fault is mechanically unstable, normally it is not present in equilibrium crystalline phases.

A soft potential and a sufficiently long "annealing" can eliminate the artifact.

The stacking fault does not disturb long-range orientational symmetry, but it can disrupt the translational order very effectively. In the hard sphere experiments, the translational order was indeed found to decrease drastically, but the orientational order was found to decay extremely slowly [5.16-17].

5.5 Atomic Displacements and Random Static Strain Fields

There are two salient features of the low temperature solid solutions undergoing the CGT as we already mentioned in last two chapters. The first is the formation of the topological defects caused by local relaxation of the atoms with different sizes. The second is the retention of the configuration. These results have profound effects on the crystal to glass transition (Landau theory, chapter 4), thermodynamic and dynamic properties (sections 5.4, 5.5), and the formation of microstructures of metastable solid solutions and amorphous phase.

In principle, a topological order to disorder transition can be described exactly by the atomic displacements, $\mathbf{u}_i$, which are deviations of each atom from its equilibrium position in a topologically ordered phase. The only drawback to this approach is the number of degrees of freedom (dN numbers of them for a d-dimensional system with N atoms) of the displacement vectors. The quantity cannot be handled easily if it is used as an order parameter (it is equivalent to a Heisenberg spin but with a *variable length*). In the Landau theory (chapter 4), we used the coarse grained displacement field to simplify this issue. To simplify the matter further, one can even use an averaged atomic displacement (the Lindemann's criterion, see 3.3).

Fig. 5.13 (a) shows the static mean displacements of the binary arrays versus

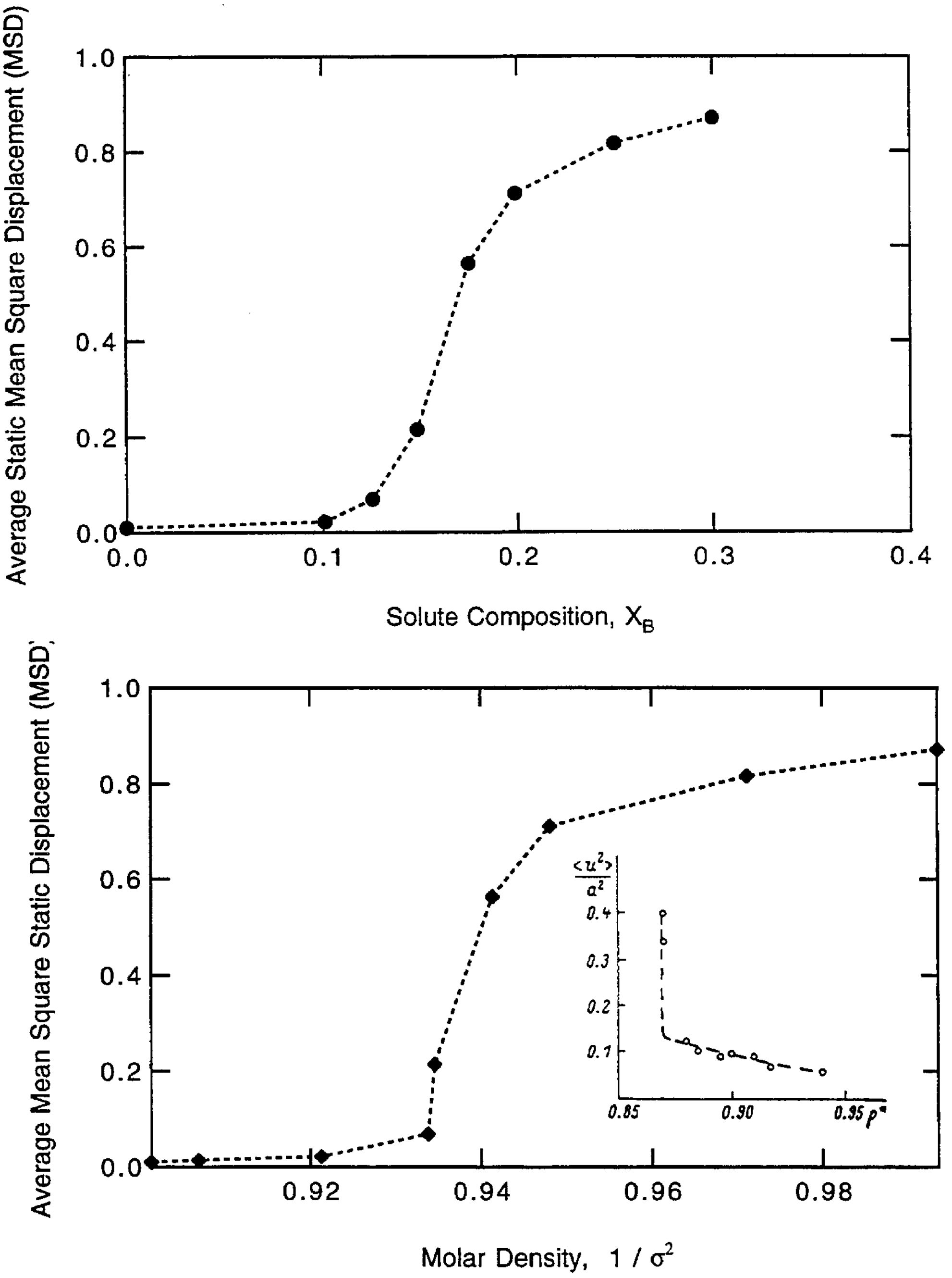

Fig. 5.13 *Top*: the average mean square static atomic displacement (MSAD) versus solute concentration (normalized by the lattice parameter a^2). *Bottom*: the same MSAD versus the molar density of the solid solution. *Insert*: the mean square displacement versus the density of a two-dimensional LJ solid during melting [5.19].

*the solute concentration. We notice the qualitative differences in the mean displace*ments between melting and the CGT (Fig. 5.13 (b)). In the case of thermal melting, it increases slowly and linearly up to melting temperature, but then abruptly jumps to a large value at melting temperature. In the CGT, the mean square displacement increases slowly in the crystalline side and shows a gradual rise at $x > 0.125$ and becomes almost saturated at $x > 0.20$ where the long-range translational order begins to disappear. Such the different characteristic of MSAD exhibited during the melting and the CGT suggests the profound difference between them. The similar abrupt change in defect density has been mentioned early [5.14].

The strain fields associated with the defects in the solid solution are closely related to the atomic displacement field caused by the particular atomic configurations of these defects [3.2]. In general, one cannot separate it from the rest of the displacements, such as those caused by thermal vibrations. In addition, since it is a tensor, visualization is not possible. Fig. 5.14 provides the atomic displacement fields for the binary solid solutions at different compositions corresponding to a crystalline phase and an amorphous phase.

Fig. 5.14 demonstrates some startling features of the atomic displacement field of the solid solution. One observes a large number of "displacement vertices". The displacements occur at the places where defects are present. The displacements take place in a circular fashion around an area that is free of defects. The dislocations as well as the dislocation networks generate the same type of displacements. The displacements associated with the defect networks are larger and more organized. As the solute concentration increases, more "displacement vertices" are generated and the distance between them becomes smaller. The CGT occurs when these

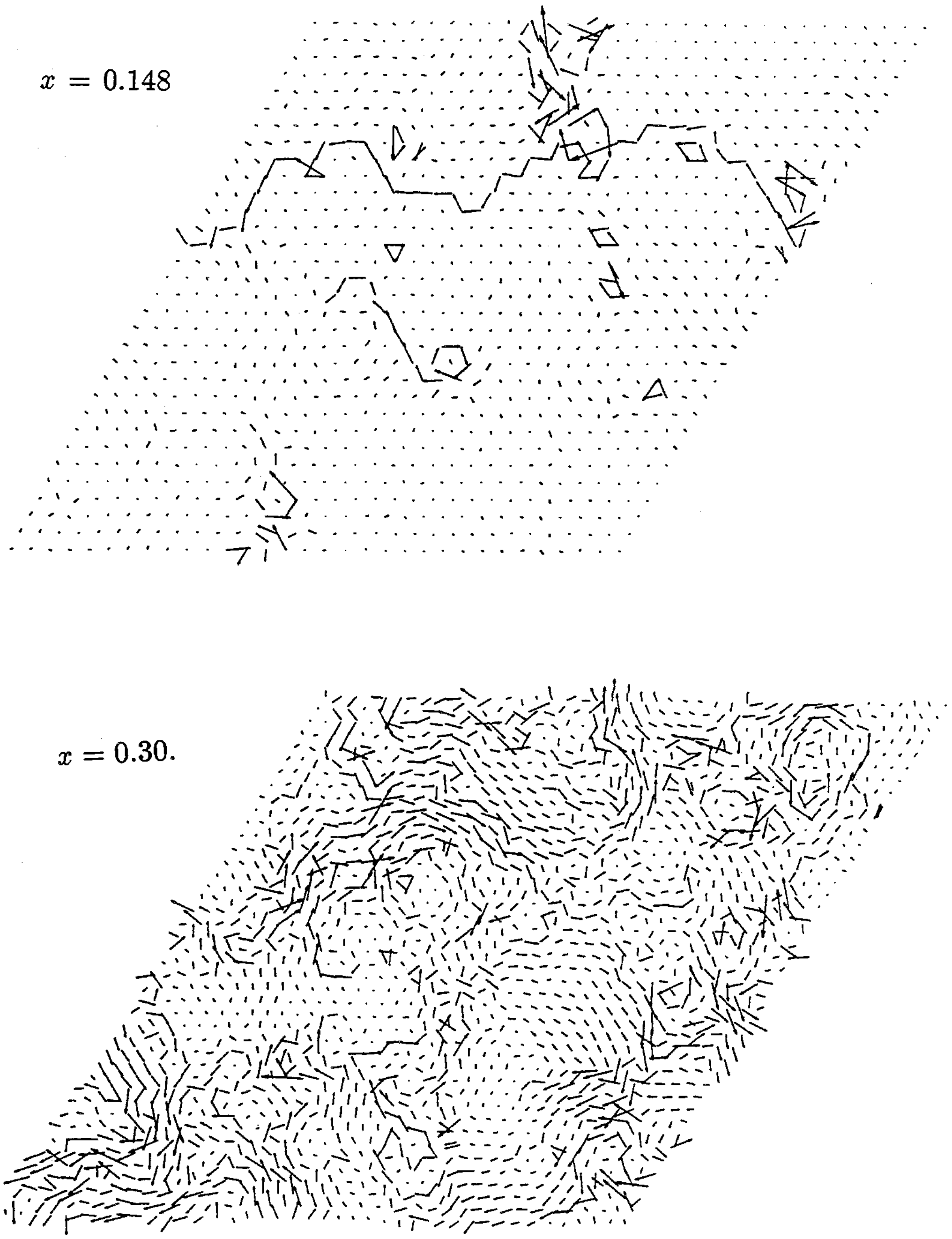

Fig. 5.14 Atomic displacement fields at the solute composition $x = 0.148$ and $x = 0.30$ for the two-dimensional LJ solid solution.

"displacement vertices" become highly populated and collide with each other. The displacement vectors between the colliding vertices are "frustrated", or misaligned, thus forming the amorphous structure.

The displacement field, especially in the crystalline phases, are representative of the strain field. One can see that the strain field is mainly generated by the defects, not only by dislocations and dislocation pairs, but also by collective defects. Most striking is the result of the almost similar strain fields generated by all those defects.

The displacement fields look "frozen" or static. They show little change of its configuration during the entire time of the simulation. This is in sharp contrast to that of a hot crystal or liquid where the configuration and the atomic displacement fields fluctuate quickly with a typical frequency comparable to the Debye frequency and the static strain dissipates quickly [5.9, 5.14]. This static nature of the displacement field in the solid solution is also confirmed by absence of long-range diffusion (section 5.6).

It is interesting to see the effects of these results to other related properties. First, the density of a metastable crystalline solid solution is microscopically inhomogeneous, but the amplitude of the density wave is small. The truly disordered regions have lower density, whereas the "crystalline-like" clusters have higher density. But the overall density of the system barely shows any significant change. Second, the solute atoms are also microscopically inhomogeneous. They are more populated in the dislocation networks than inside the "crystalline-like" clusters. But the scale of this distribution is small. These results could have significant impact on our understanding of mechanical properties of metallic glasses, nucleation *and growth of crystalline phases from the glass phase and other properties that* sensitively depend on the microstructures.

5.6 Thermodynamic Properties

We have demonstrated the thermodynamic aspects of the CGT in three-dimensional binary solid solutions that undergo the transition. However, we were limited by the finite size and time used in our simulations on this system. In two-dimensional system, we can obtain these results by using large samples and longer simulation times.

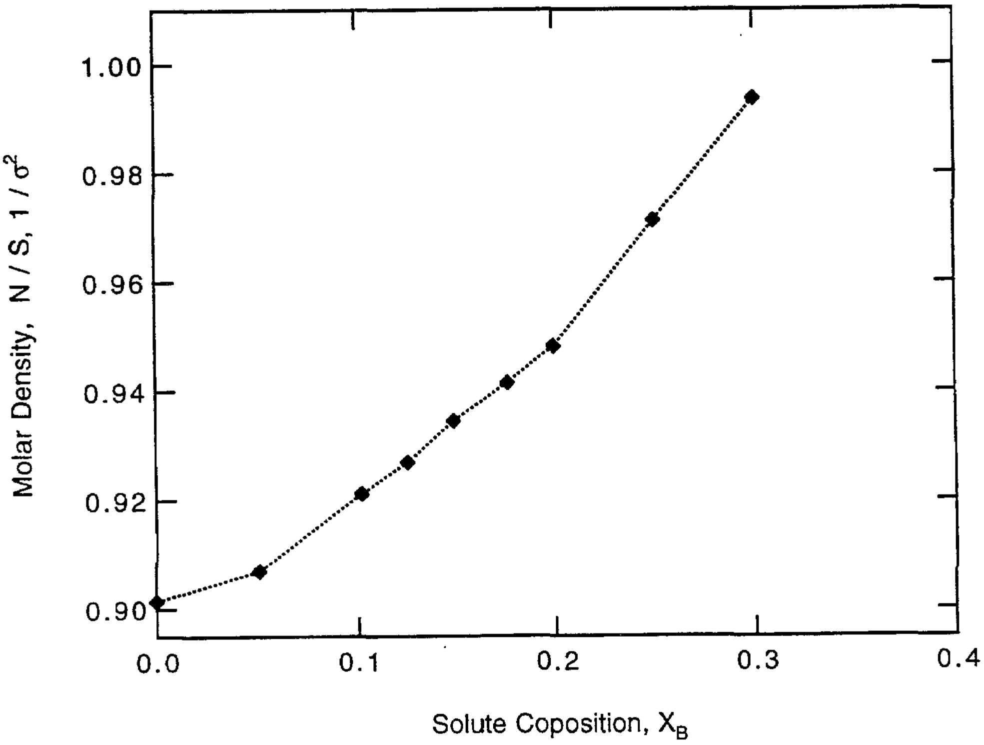

Fig. 5.15 (a) Molar density versus solute composition at $T = 0.20$.

The molar density and enthalpy change with increase of solute concentration are shown in Fig. 5.15 and 5.16. The density change (Fig. 5.15(a)) shows three

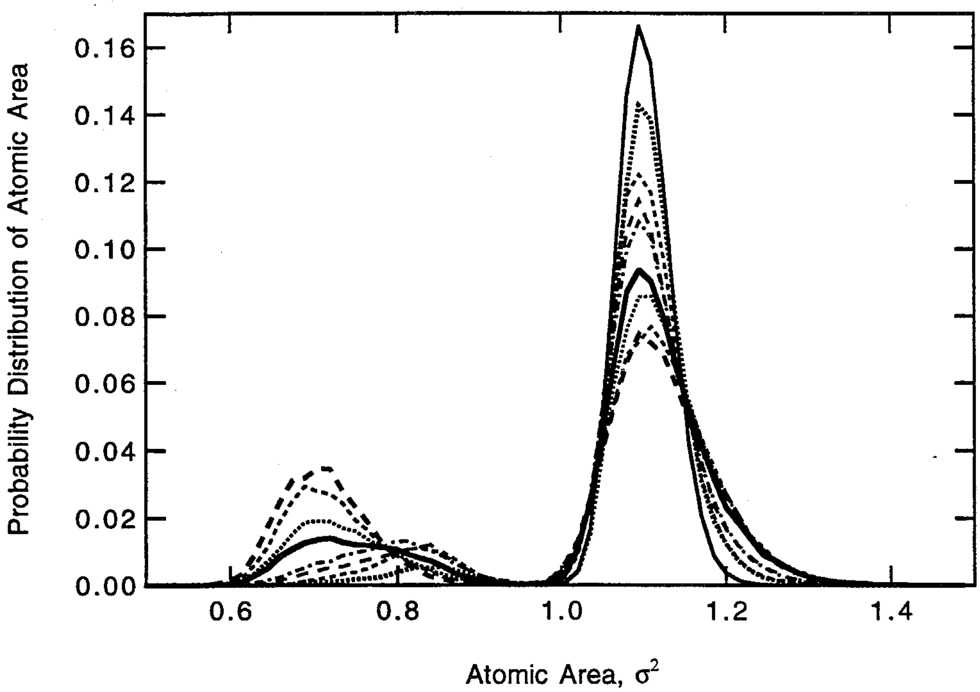

Fig. 5.15 (b) Atomic Volume distribution. From the top to the bottom: $x = 0.0, 0.05, 0.101, 0.125, 0.148, 0.175, 0.199, 0.25, 0.3$.

distinctive parts that can be seen from the different slopes in these regions. The first region is at $0.0 < x < 0.05$, the second at $0.05 < x < 0.199$ and the third at $x > 0.199$. From the results presented in previous sections, we know that the CGT occurs around $x = 0.199$. The first region in the dilute limit $x < 0.05$ likely corresponds to the equilibrium substitutional solid solution. The almost linear fashion shown in the density change in all three regions is striking.

The atomic area distribution was obtained using the Radical Plane method (Fig. 5.15 (b)). The area distribution of the large solvent atom is a Gaussian at the dilute solute concentration, but becomes slightly asymmetric at the high solute concentration. Most interesting is the solute atom area distribution. It shows a gradual shift from the mean at 0.82 for the crystalline phases at the dilute solute concentrations to the final Gaussian-like distribution for the amorphous phases with a mean at 0.71. At the CGT ($x = 0.199$), the solute atom exhibits a very broad distribution spreading over the entire area of both the crystalline phase and the amorphous phase. It appears that the solute atoms are liberated and free of being in both the crystalline phase and the amorphous phase.

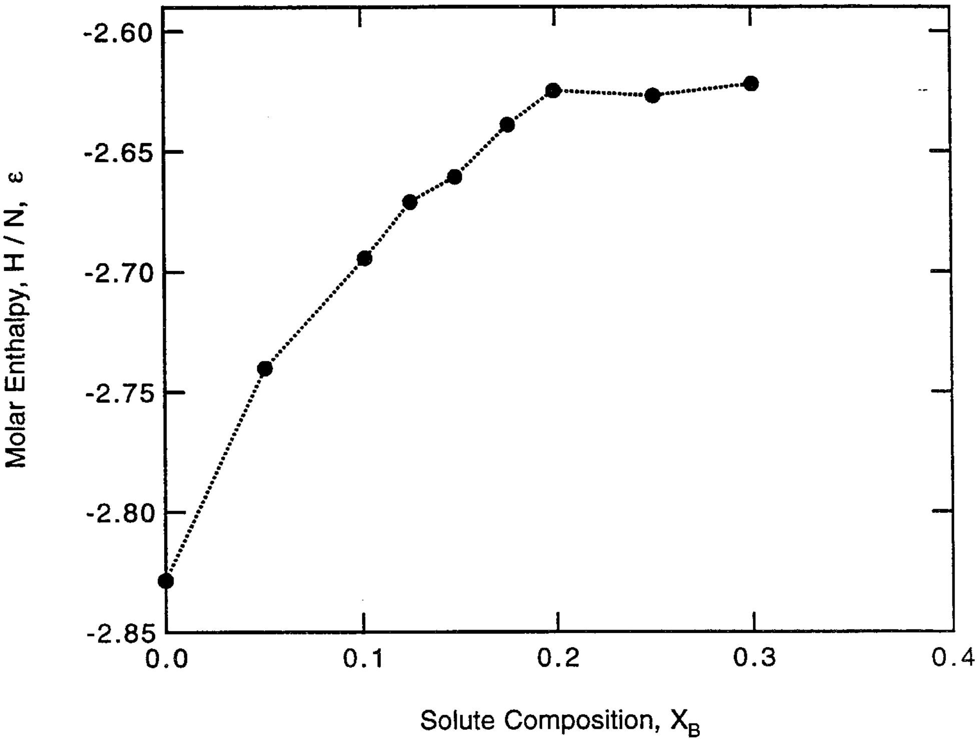

Fig. 5.16 Molar enthalpy versus solute composition at $T = 0.20$.

As for the CGT in three dimensions, the density change at the CGT at $T = 0.2$ from the crystalline phase to amorphous phase at $x \sim 0.199$ is also very small. The variations are almost within the errors introduced by thermodynamic averaging. In fact, in order to make sure that the system at $x = 0.199$ is sufficiently equilibrated, we performed several simulations with different sample sizes and extremely long equilibrating time (8×10^6 MD steps). We found no substantial change of the densities for these different runs.

The molar enthalpy also behaves similarly to that observed in the three-dimensional binary solid solutions. It increases rapidly at the dilute end of the solute concentration and begins curving down slightly before the CGT occurs. The change of the enthalpy at the CGT, by extrapolating the enthalpies from both the crystalline and the amorphous sides, is almost zero. In addition, no hysteresis was observed. The enthalpy appears to increase continuously from the crystalline phase to the amorphous phase. The system spontaneously transforms to amorphous, or a "hexatic"-like phase, which has no long-range translational symmetry.

Interestingly we observed some quantitative changes at higher temperature. Fig. 5.17 and Fig. 5.18 are the density and molar enthalpy at $T = 0.25$ which is very close to the glass transition temperature. By extrapolating the density and enthalpy from both sides, one can observe slight jumps at the CGT, which corresponds to solute composition at $x = 0.15$. These results, together with those presented above, suggest that the CGT indeed becomes more continuous as the temperature decreases, as predicted by the Landau theory. In the next section, one will find that the elastic properties at both temperatures show strikingly similar behavior.

The plateau region of the enthalpy on the amorphous side is directly related to the openness, or uncertainty of the amorphous structure. Unlike the crystalline phase where even a local distortion can lead to a large energy change, as seen at the dilute end of the binary solid solution, the amorphous phase can accommodate

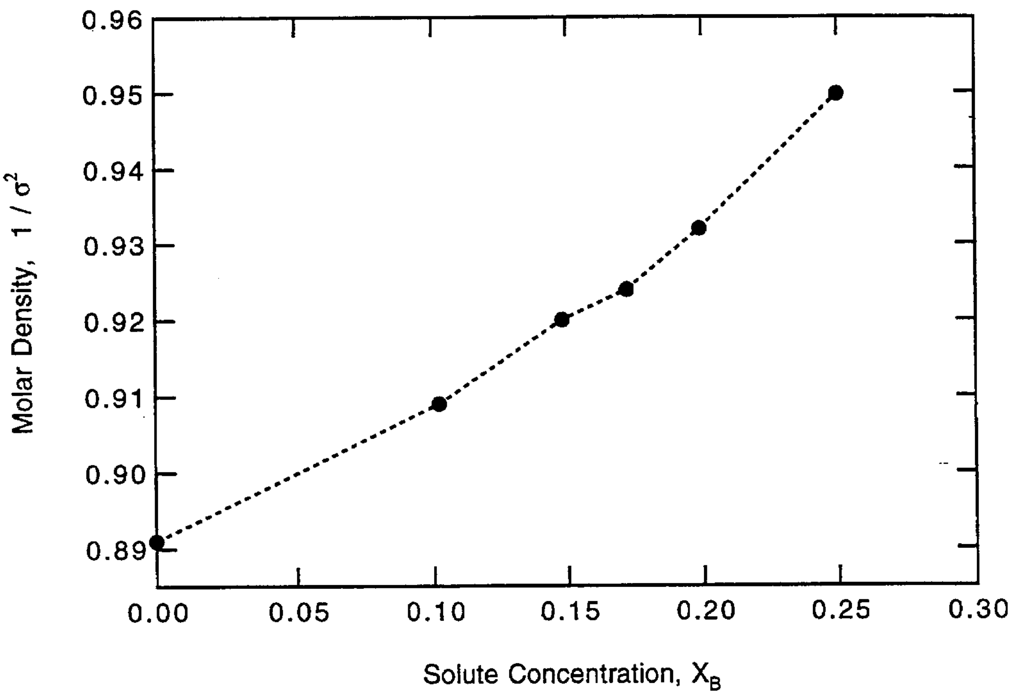

Fig. 5.17 Molar density versus solute composition at $T = 0.25$.

the local "imperfection" easily. This insensitivity of bulk properties to disordering in the amorphous phase is one of the interesting characteristics of the amorphous phase.

5.7 Elastic Properties

The crystal to glass transition is a structural phase transition, thus the susceptibility of the structure to any perturbation, such as temperature, composition, stress, etc., is directly related to the elastic constants (see 3.3). A thermodynamic phase transition such as the CGT is defined by the condition, $\Delta G(T, x) = 0$, at the transition. The transition is characterized by different behaviors of the elastic constant, which strongly depends on the polymorphic condition and material

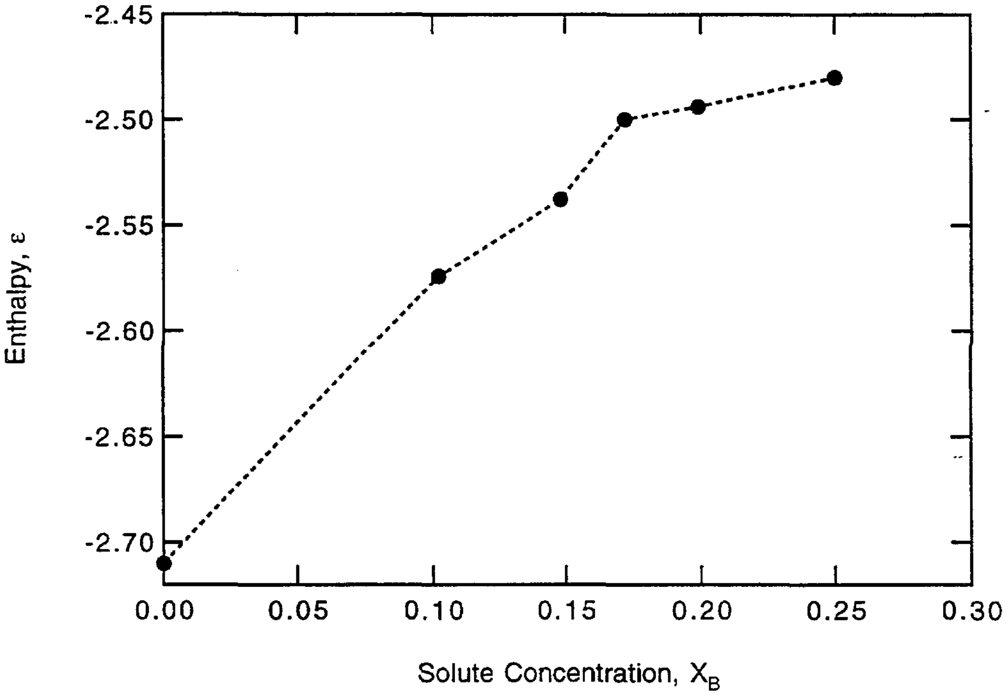

Fig. 5.18 Molar enthalpy versus solute composition at $T = 0.25$.

properties (chapter 4).

A pure mechanical instability occurs when an elastic constant vanishes, whereas the free energies of the starting and end phases bear no relationships. Fracture, cavitation and any other structural transformation with a characteristic time much shorter than the intrinsic atomic relaxation time with which thermodynamic (metal) equilibrium, or cooperative motions of atoms must be achieved, are related to mechanical instability.

The elastic constants of the solute solutions are shown in Fig. 5.19. Since the hexagonal lattice is isotropic, there are only two independent elastic constants, one shear and another bulk. The elastic anisotropy constant, C'/C_{44}, is unity in an ideal isotropic media, where $C' = (C_{11} - C_{12})/2$. From Fig. 5.20, one could see that the shear elastic constant decreases sharply in the two-dimensional solid solution. It plunges to almost 95% from that of a pure hexagonal crystalline solid at the transition and then levels off at a finite value at the amorphous side. Once again, we observe the slow response of the amorphous phase to the changing solute concentrations.

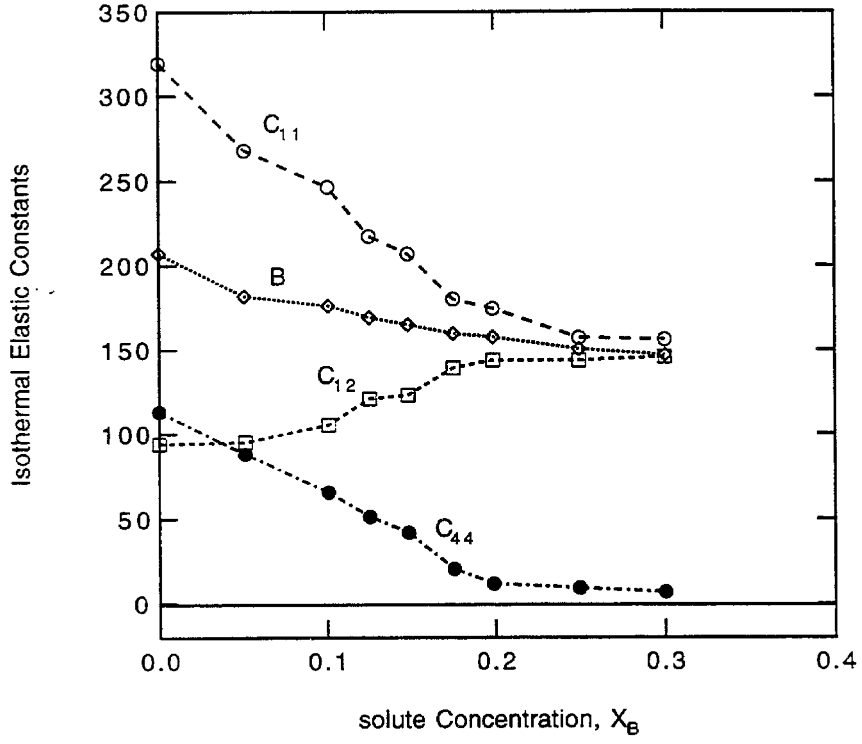

Fig. 5.19 Isothermal elastic constants versus solute composition. C_{11}, C_{12} and C_{44} are elastic constants which are related to the Lamé coefficients, $\lambda = C_{12}$ and $\mu = C_{44}$. B is the isothermal bulk modulus.

As suggested by the Landau theory, the elastic shear constant is determined by three variables, the homogeneous or non-normalized shear constant μ_0 when no static displacement occurs, the strain-displacement coupling constant ϵ, and the non-normalized susceptibility χ_0, $\mu = \mu_0 - e^2\chi$. μ_0 decreases usually decreases with both temperature and composition. If alloying occurs, which corresponds to the case where the LJ parameters, $\epsilon_{AA}, \epsilon_{AB}$, and ϵ_{BB}, take different values, μ may increase. In the case of the LJ solid solution where interaction between solvent and solute atoms are equal, we expect μ_0 to decrease. Extrapolating μ to the dilute limit of the solute concentration, one can obtain μ_0. Fig. 5.20 shows an almost linear decay of μ in the crystalline phase. It begins to curve down at $x > 0.13$. One expects the static, random strain to be in effect at/above this composition.

Although extremely small, the shear elastic constant does not go to zero, as does the Kosterlitz-Thouless coupling constant, K. We tested the finite size effect on the elastic constants at the concentration of $x = 0.199$. We did observe a decreasing μ as the system size is increased, but the convergence became very slow. More extensive simulations are required in the future to resolve this issue.

It is interesting to see the similar behavior of the elastic constants at a higher temperature. Fig. 5.21 shows the shear elastic constants at $T = 0.25$. The largest drop of the shear elastic constant occurs at $X = 0.16$, where the CGT was observed.

Because there is only one shear elastic constant, one can unambiguously determine its behavior as the crystalline solid becomes progressively disordered. The shear elastic constant decreases monotonously in the same way as we observed for C' in the three-dimensional case, but the magnitude of the softening is much larger.

The bulk modulus B_T (Fig. 5.22), which equals $B_T = (\mu + \lambda)$, does not show substantial variations through the crystalline and amorphous phase. It shows a smooth decrease at the CGT (Fig. 5.23).

It is very interesting to notice the effect of the elastic anisotropy on the CGT.

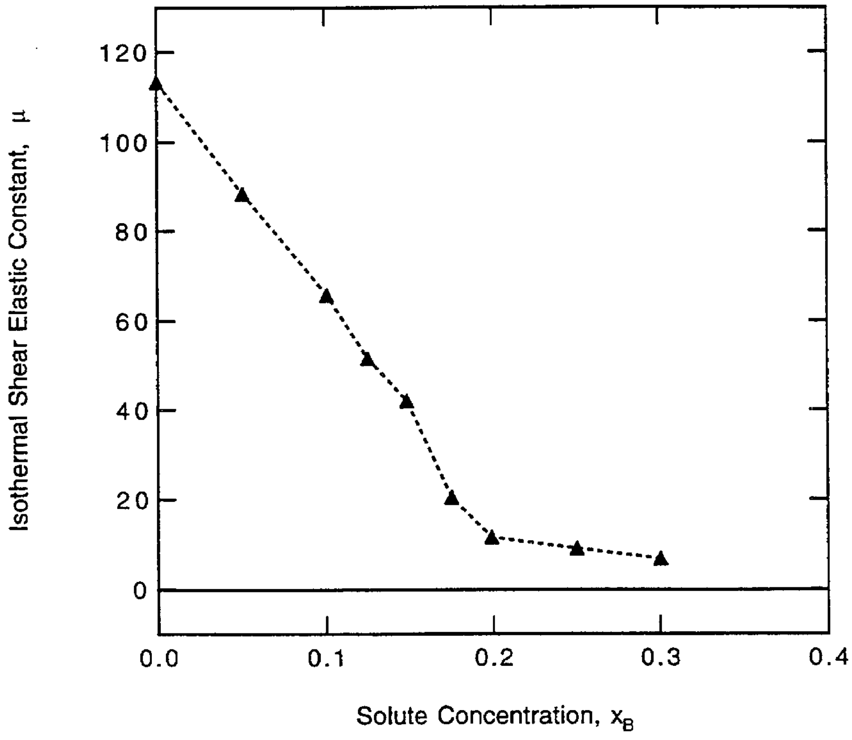

Fig. 5.20 Isothermal shear elastic constants versus solute composition at $T = 0.20$.

Most crystalline materials used to synthesize amorphous phases are not elastically isotropic, although most of them have Bravais lattices with high symmetry. So there are several shear elastic constants associated with the different shear deformation modes. On the other hand, an amorphous phase has only one shear elastic constant, because it is isotropic. It is important therefore to distinguish which shear elastic constant is the one that triggers the CGT and which one becomes softening merely because of the development of the elastic anisotropy at the transition from an anisotropic structure to another. A two-dimensional hexagonal binary array is the simplest example with only one shear elastic constant, so no ambiguity is involved in identification of the softest shear mode.

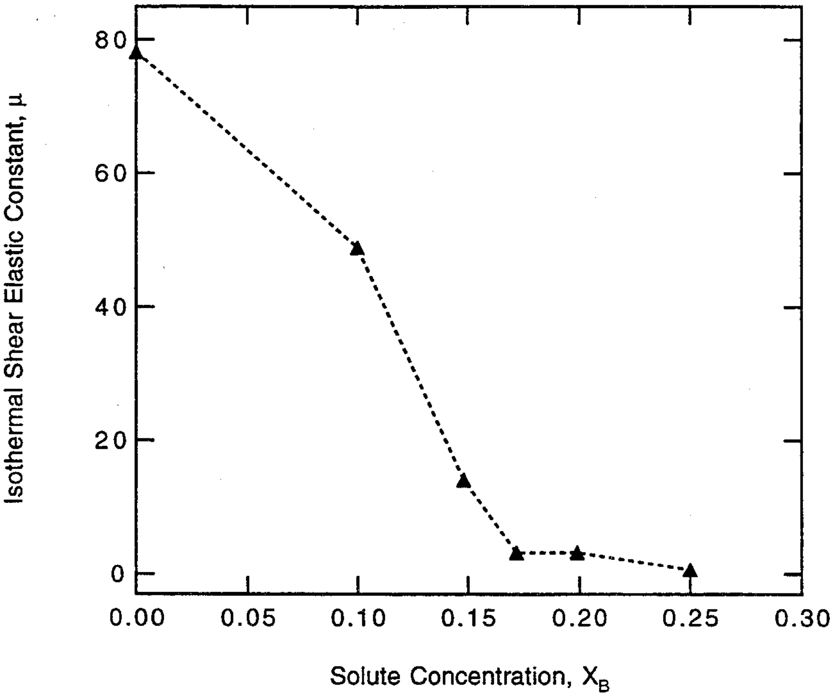

Fig. 5.21 Isothermal shear elastic constants versus solute composition at $T = 0.25$. Note the softening of the shear modulus due to increasing temperature (see Fig. 2.20).

5.8 Dynamic Properties

So far we have focused our attention on static, or time-independent properties of the LJ solid solutions in order to study thermodynamic aspects of the CGT. Dynamic properties, on the other hand, are also extremely useful for the understanding of kinetic aspects of the solid solution and the crystal to glass transition. For example, from time-dependent fluctuations of strains and radial distribution functions, one can gain insight of the temporal scale of how static the atomic displacements are; from time-dependent mean square displacements one can obtain diffusion constants; and from results of the velocity autocorrelation function and

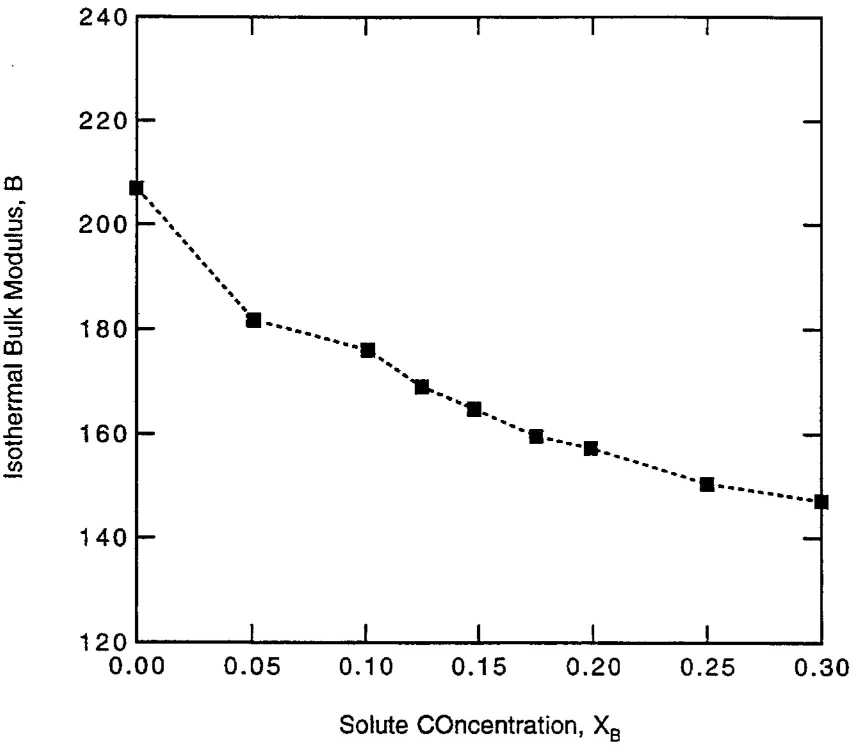

Fig. 5.22 Isothermal bulk modulus (its inverse is the compressibility) versus solute composition at $T = 0.20$.

its Fourier transform, which is the generalized vibrational density of states, one can perceive not only long-wave, low-frequency acoustic properties such as the elastic constants, but also localizations of lattice vibrations at high freqencies. In this thesis, we present only those properties that are most relevant to our understanding of the CGT.

The time dependence of the atomic displacements have been discussed in section 5.5, we shall not repeat them here. In the remainder of this section, we shall devote our attention to the following properties, time dependent mean square displacements (TMSD), velocity autocorrelation functions (VCF), and derived properties that can be directly obtained from these properties, such as diffusion constants, *generalized phonon density of states and elastic properties.*

A. Mean Square Displacement, Diffusion Constants

Figs. 5.23 show the time dependent mean square displacements of the binary solid solutions at different solute concentrations. According to the Einstein relation (2.19), the slope of the TMSD at long time limit gives twice the diffusion constants in two dimensions. Fig. 5.23 shows that all of the TMSD's for different solute compositions have a flat tail at relatively long time limit, indicating the absence of long-range diffusions in the system. One of the differences for these different systems is the slope at the earlier time caused by dynamic relaxation of atoms. The saturated values for the TMSD at long-time limit are also different. The dynamic relaxation at the short time becomes long and less sharp as the solute concentration increases, indicating the increasingly difficult for the system to reach equilibrium as the system become more metastable. The saturated mean square displacements at long time limit increase with the increase of the solute composition.

The intrinsic diffusivity for each type of atoms in the solid solution can be obtained from the slopes of the TMSD's of each atoms. The TMSD defined on the right-hand side of equation (2.19) can be separated into two parts for each type of atoms,

$$\begin{aligned} < |\delta \mathbf{r}(t)|^2 > &= \frac{1}{N} \sum_{i}^{N=N_A+N_B} < |\mathbf{r}_i(t) - \mathbf{r}_i(0)|^2 > \\ &= \frac{1}{N} \left[\sum_{i}^{N_A} < |\mathbf{r}_i(t) - \mathbf{r}_i(0)|^2 > + \sum_{i}^{N_B} < |\mathbf{r}_i(t) - \mathbf{r}_i(0)|^2 > \right] \\ &= x_A < |\delta \mathbf{r}_A(t)|^2 > + x_B < |\delta \mathbf{r}_B(t)|^2 >, \end{aligned} \tag{5.7}$$

where x_A and $x_B = 1 - x_A$ are the solvent and solute concentrations respectively.

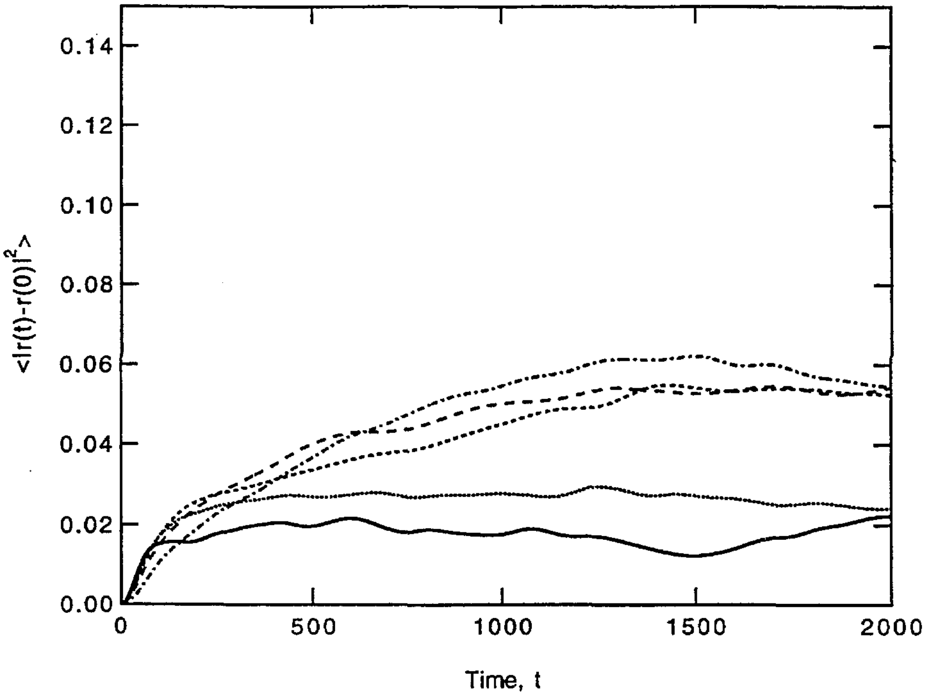

Fig. 5.23 Total time dependent mean square displacements. Diffusion constants are proportional to the slopes of the curve at long-time limit. The intrinsic diffusion constants of each types of atoms, D_A and D_B can be obtained from the slopes of the partial TMSD's of each atom. Solid line: $x = 0.0$, dotted line: $x = 0.101$, broken line: $x = 0.148$, dashed line: $x = 0.199$ and dash-dotted line: $x = 0.30$.

The partial mean square displacement is defined as

$$< |\delta \mathbf{r}_\alpha(t)|^2 >= \frac{1}{N_\alpha} \sum_{i}^{N_\alpha} < |\mathbf{r}_i(t) - \mathbf{r}_i(0)|^2 >, \tag{5.8}$$

where α denotes two types of atoms, A or B. The intrinsic diffusion constant for each type of atom in the solid solution can therefore be obtained by the Einstein relation (2.19) in two dimensions,

$$D_\alpha = \lim_{t \to \infty} \frac{1}{2t} < |\delta \mathbf{r}_\alpha(t)|^2 > . \tag{5.9}$$

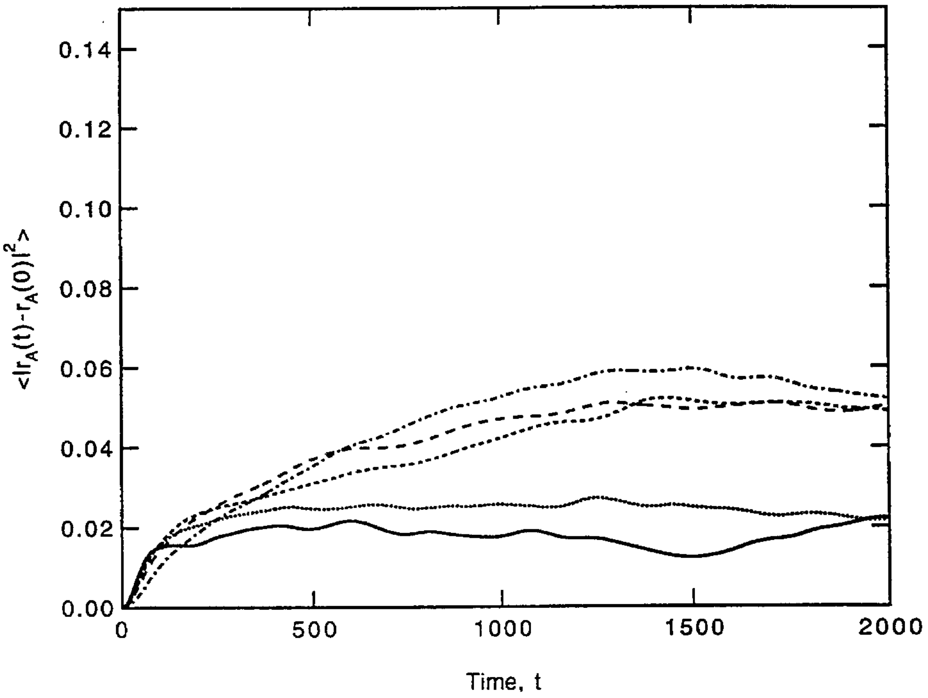

Fig. 5.23 (continued) TMSD for the solvent atom.

As shown by the partial TMSD's in Fig 5.24, the small atom always has a larger mean square displacement compared with the large atom. Also the intrinsic diffusivity of the smaller atom is larger too (not shown here). These results also indicate that the atoms, most of which are the solute atoms, in the disordered networks are more mobile than those inside the "crystalline-like" cluster, because solute atoms are usually situated in these regions. Such an observation is also confirmed by the velocity autocorrelation functions (2.20) for the two types of atoms.

B. Velocity Autocorrelation Functions

Fig. 5.24 (a) show the VCF's for the binary arrays. The VCF's are quantitatively different for the crystalline and amorphous phase. These features include the

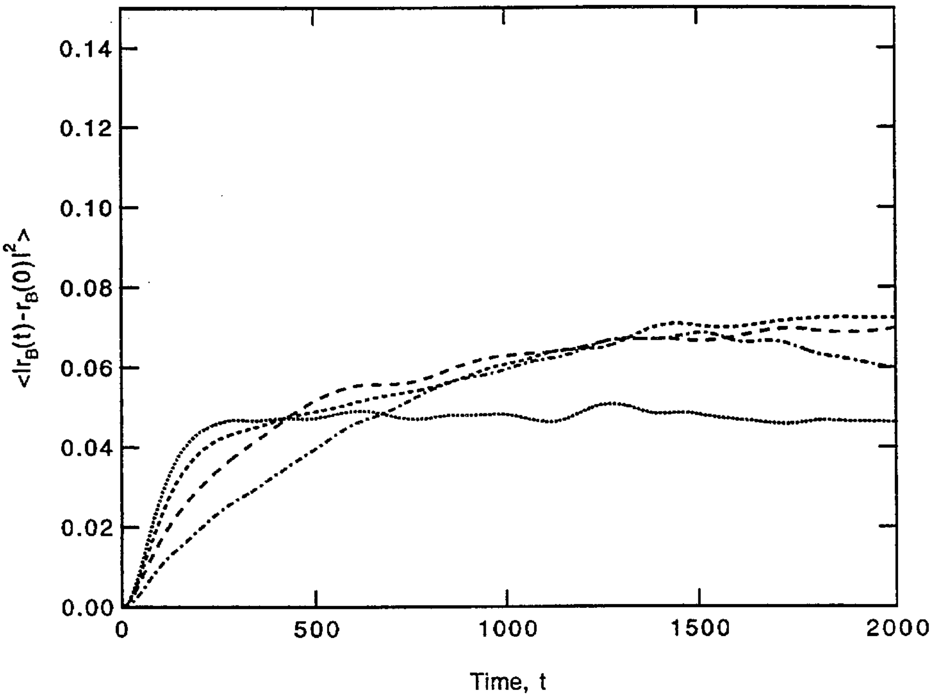

Fig. 5.23 (continued) TMSD for the solute atom.

"collision" time at which the velocity autocorrelation function changes the sign, the *magnitude of the oscillations*, and the *characteristic decaying time* of the oscillations to approach zero.

The "collision" time is about a picosecond for the crystalline phase. It increases gradually as more solute atoms are added, while the depths of the first oscillation become shallower. At the solute concentration $x > 0.199$, where the CGT was observed to occur, the VCF look much like that of a liquid.

More detailed information can be obtained from the partial VCF's of the solute and solvent atoms. From Fig. 5.24 (b) and (c), one can see that the solute atoms behave like a liquid, its characteristic vibration frequency, as indicated by the large

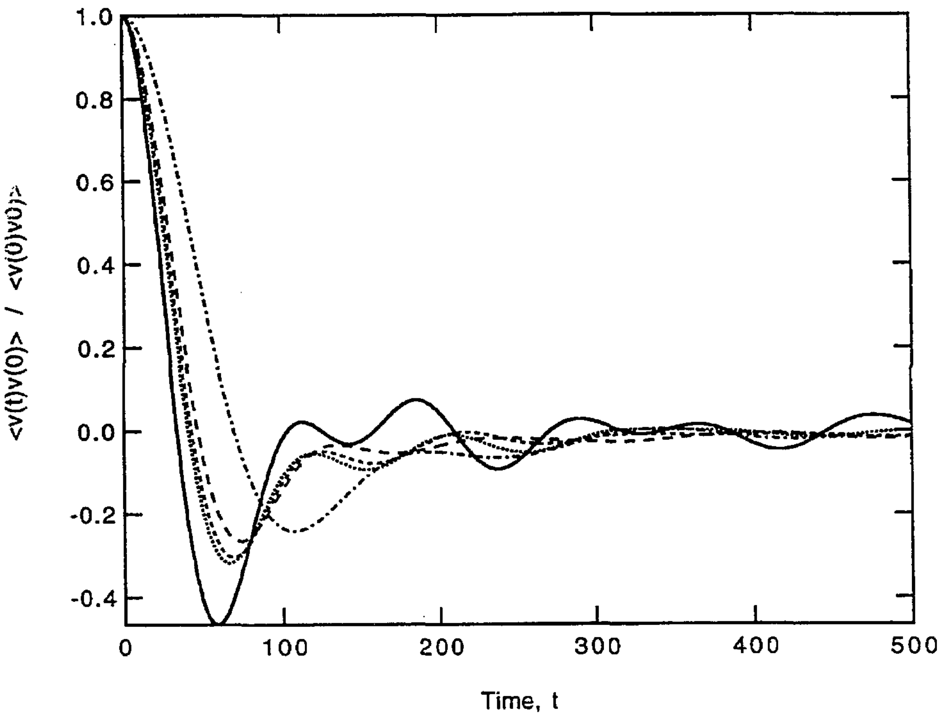

Fig. 5.24 (a) The total velocity autocorrelation functions. Solid line: $x = 0.0$, dotted line: $x = 0.101$, dashed line: $x = 0.148$, broken line: $x = 0.199$ and dash-dotted line: $x = 0.30$.

"collision" time, is extremely low. In fact, this result can be seen more clearly later from the generalized phonon density of states.

C. Genenralized Phonon Density of States

Fourier transformation of the VCF's gives the generalized vibrational density of states (DOS). The DOS obtained is no longer limited to low temperatures where the harmonic approximation is used to facilitate computations. Fig. 5.25 is the total DOS's and partial DOS's for the binary solid solutions at different solute concentrations. The DOS, and the phonon dispersion relations along high symmetry

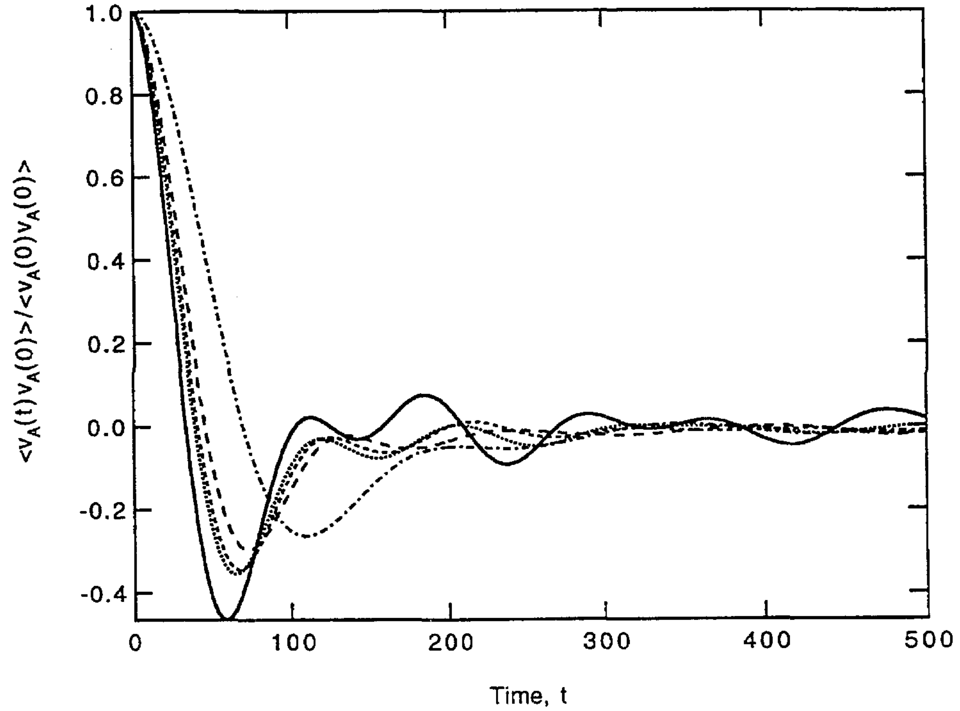

Fig. 5.24 (b) Partial VCF's for solvent atoms.

directions of the perfect two-dimensional LJ hexagonal crystal calculated using the harmonic approximation is also shown in Fig. 5.26 for comparison.

We shall summarize briefly some intersting properties that the DOS's reveal. First, the slopes at low frequency part of the DOS increases with the increase of the solute concentration. This part of the DOS is directly related to the slopes of the phonon dispersion curves, $\mathrm{DOS}(\omega) \propto 1/|\nabla_q \omega|$, where $\omega(\mathbf{q})$ is the phonon dispersions and $\mathbf{q}$ is the phonon wave vector. The increase of the slopes of the DOS's at the low frequency indicates softening of the transverse phonon dispersions, which has the lowest excitation energy, and thus softening of the shear elastic constant (elastic constants can be obtained from the the slopes of the phonon dispersion curves at

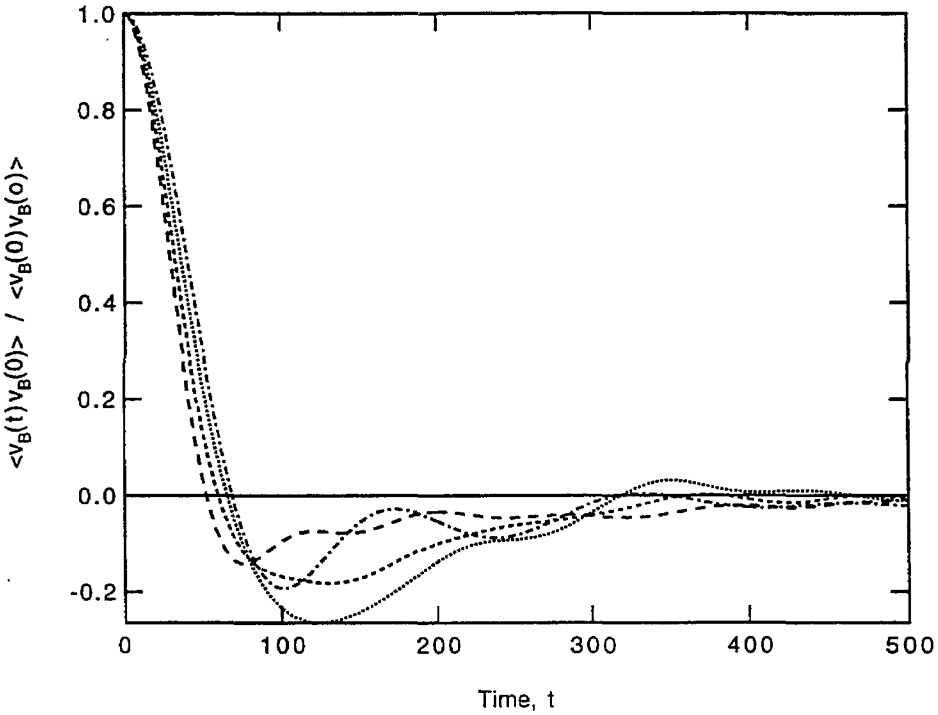

Fig. 5.24 (c) Partial VCF's for solute atoms.

the long-wage limit, $q \to 0$). In fact, the entire phonon spectra are shifted to lower frequency as the crystalline phase becomes more disordered. Second, a nonzero DOS at zero frequency, DOS($\omega = 0$), is directly proportional to the diffusion constants (average diffusion constants) For all systems simulated, the DOS($\omega = 0$) are close to zero. The small amount of increases of the DOS at zero frequency as shown in Fig. 5.26 suggests that there is no substantial diffusion occurring in the binary solid solution. Third, the DOS is largely determined by the behaviors of the solvent atoms at low solute concentrations, but dominated by that of the solute atom at higher concentrations. Fourth, at such a low temperature, we did not observe any sharp resonant mode at low frequencies caused by the small solute atoms. We

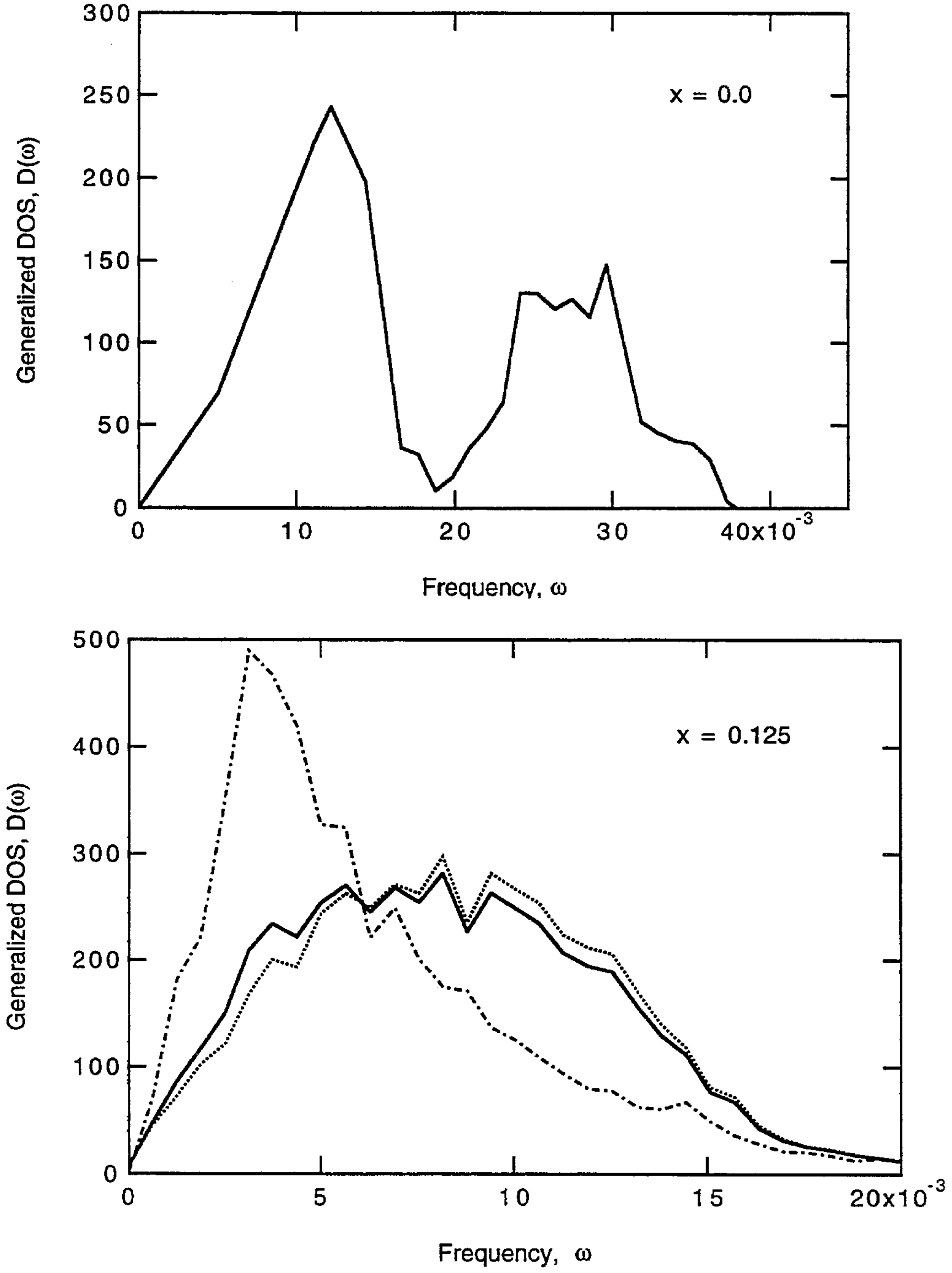

Fig. 5.25 The generalized phonon vibrational density of states for the two-dimensional solid solutions. The partial DOS's for the solvent (dotted line) and the solute atoms (dot-dashed line) are also shown.

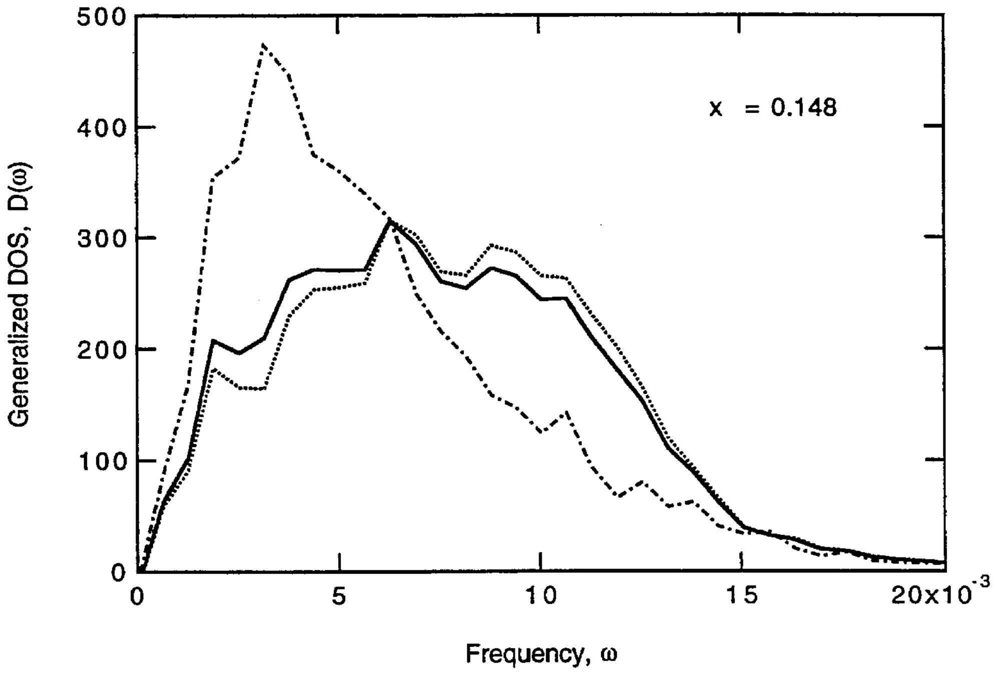

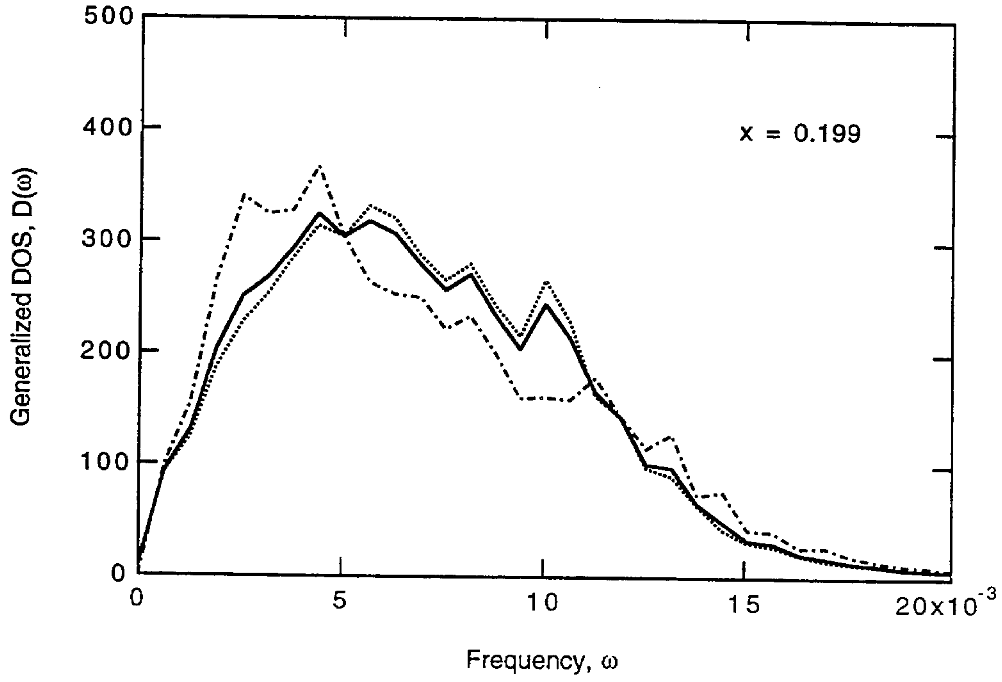

Fig. 5.25 (continued)

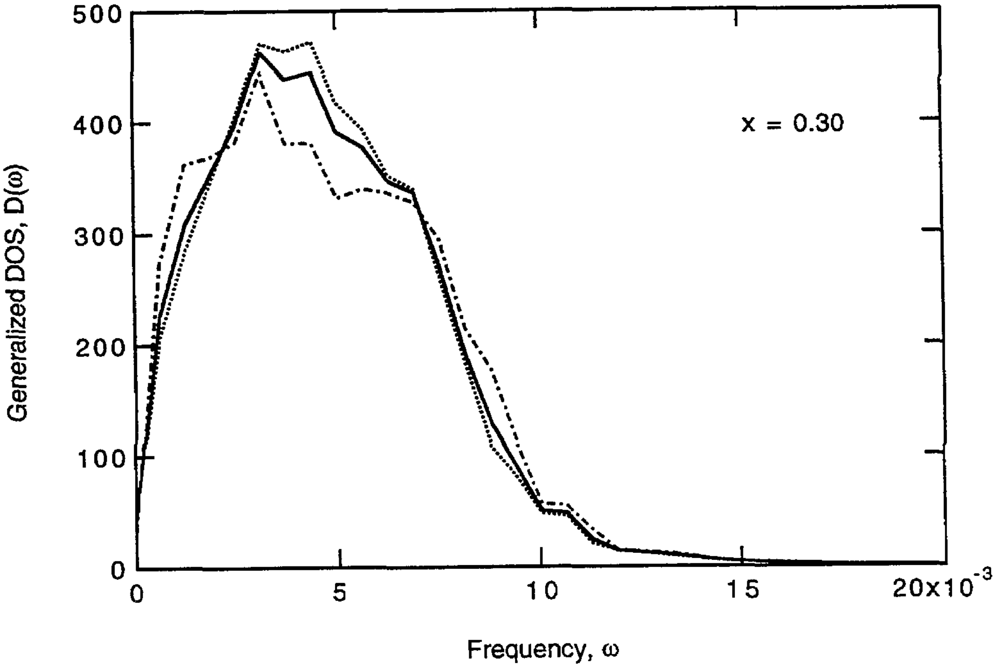

Fig. 5.25 (continued)

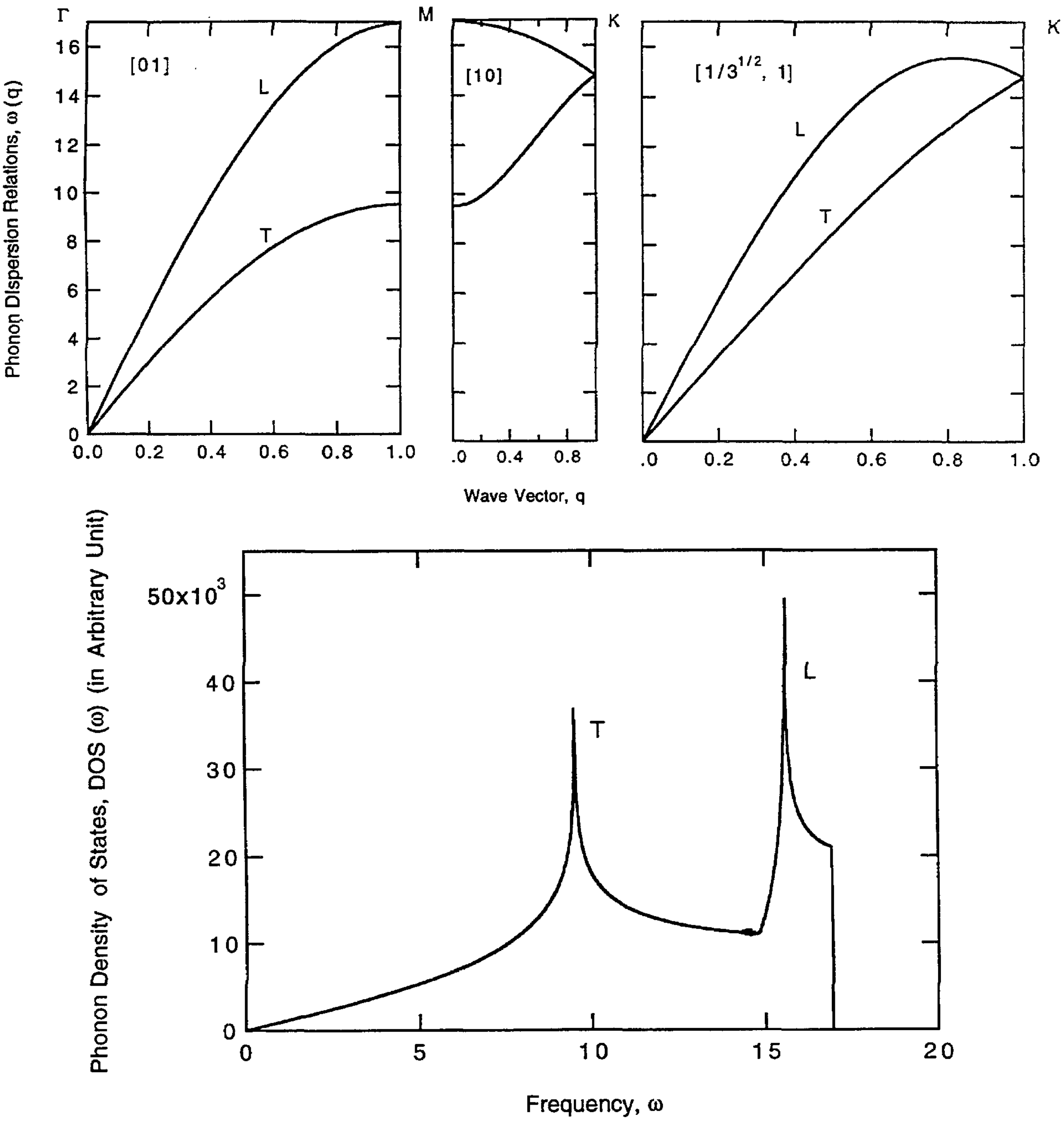

Fig. 5.26 *top*: phonon dispersion relations for a pure LJ hexagonal crystal calculated using the harmonic approximation; *bottom*: Generalized vibrational density of states. Note that from the Debye model, a linear DOS at low frequency is expected for a two-dimensional solid.

also did not see any localized mode at high frequencies resulting from the strong topological disorder.

References

5.1 For a comprehensive review, see K. J. Strandburg, Rev. Mod. Phys., **60**, 161, (1988).

5.2 F. H. Stinlinger and A. Rahman, J. Chem. Phys., **57**, 1281, (1972).

5.3 F. Spaepen, J. Noncryst. Solids, **31**, 207, (1978).

5.4 M. R. Hoare, J. Noncrystal. Solids, **31**, 157 (1978).

5.5 L. D. Landau, *Collected Papers of L. D. Landau*, edited by D. Ter Haar (Pergamon Press, Oxford, 1965), chapter 29.

5.6 R. E. Peierls, Helv. Phys. Acta., **7**, Suppl. II, 81, (1934).

5.7 N. D. Mermin and H. Wagner, Phys. Rev. Lett., **17**, 1133, (1966).

5.8 W. G. Hoover, W. T. Ashurst and R. J. Olness, J. Chem. Phys., **60**, 4043, (1974).

5.9 F. Abraham, Phys. Rept., **80**, 339, (1981).

5.10 J. M. Ziman, *Models of Disorder*, (Cambridge University Press, Cambridge, 1979), chapter 5.

5.11 D. R. Nelson and B. I. Halperin, Phys. Rev. B, **19**, 2457, (1979); Phys. Rev. B, **21**, 5312, (1980).

5.12 J. M. Kosterlitz and D. J. Thouless, J. Phys. C**6**, 1181, (1973).

5.13 S. T. Chui, Phys. Rev. B, **28**, 178 (1979).

5.14 M. P. Allen, D. Frenkel and W. Gignac, J. Chem. Phys., **78**, 4206 (1983).

5.15 A. H. Cottrell, *Dislocations and Plastic Flow in Crystals* (Oxford University, Press, Oxford, 1953).

5.16 D. R. Nelson, M. Rubinstein and F. Spaepen, Phil. Mag. A, **46**, 105 (1982).

5.17 D. R. Nelson, M. Rubinstein, Phys. Rev. B, **26**, 6254, (1982).

5.18 C. H. Bennett, J. Appl. Phys., **43**, 2727, (1972)

5.19 V. M. Bedanov and G. V. Gadiyak, Sov. Phys. Solid State, **26**, 382 (1984).

Chapter 6

Conclusion

6.1 Thermodynamics and Microscopic Mechanism for the CGT

The crystal to glass transition was investigated in a model LJ binary random substitution solid solution. The transition was observed to occur at a critical solute concentration and a solute/solvent atomic size ratio. A critical temperature exists below which the transition occurs with extremely small elastic shear rigidity, vanishing latent heat, and density. The microscopic origin of this phenomenon was sought and found to be related to the topological defects which are created by the solute/solvent atomic size difference and frozen randomly by the low temperature constraint. At the critical concentration and the solute/solvent atomic size ratio, the critical fluctuation of the static, random strain field becomes diverging, leading to the vanishing elastic shear modulus and the percolating disordered networks. This proposal of the microscopic mechanism agrees well with the existing experimental results of the irradiation induced amorphization [3.39, 6.1].

6.2 Comparison with Melting

From the results obtained from studying the crystal to glass transition, we could draw certain conclusions about necessary conditions required to induce the topological order to disorder transition. These criteria can be extended to thermal melting transition, which is a high temperature analogue of the crystal to glass transition.

A. Topological Defects

Topological defects are solely responsible for both transitions. In fact, because they play such a crucial role, the topological transitions can be considered as "defect-induced". The defects can be created in different ways, thermal vibration, solute alloying, irradiation, mechanical deformation, etc..

B. Density and Morphology of Topological Defects

It was found that the defect density *and* the defect morphology play equally important role in inducing the topological order to disorder transitions. Kinetic constraints, commonly implemented by varying temperature, can alter the transition profoundly. If the topological defects can be kept randomly distributed without large scale clustering, at a critical density the transition can be continuous and spontaneously. Otherwise, if the defects are allowed to coalesce and form extended aggregates, (correspondingly, the critical density is reduced), the required critical strain fluctuation will be suppressed or even eliminated, therefore, the transition will likely proceed with formation and growth of these disordered aggregates, or phases resulting from these disordered clusters.

Melting occurs at high temperature. The large thermal excitation makes it possible for atoms to seek equilibrium configurations, thus reducing the defect density and forming defect clusters. Melting, in two or three dimensions, are therefore, always first order. The CGT, on the other hand, could be either first order or continuous, depending on the kinetic constraints imposed on the crystalline phase undergoing the transition.

It is therefore, not surprising to find that the continuous melting in two dimensions has been observed only in systems of which the defects have extremely large chemical potentials to resist clustering. Such the systems include the dislocation vector model [6.2] and the Coulomb gas [6.3]. Whether or not melting in two-dimensional *atomic* solids is continuous has been much of debate [5.1, 5,9], however, evidences, mainly from computer simulations using larger samples and longer simulation times, suggest that it is a first order [5.1, 5.9, 6.4, 6.5].

The conclusion drawn from the CGT inspired us to study a binary solid solution with an extremely large solute-solute repulsion. The large chemical potential of the solute atoms could keep the defects, which were found mainly associated with the solute atoms, to remain separated, thus offering a chance to see the dislocation unbinding mechanism [5.11] for the CGT in the atomic system.

References

6.1 D. E. Luzzi, H. Mori, H. Fujita and M. Meshii, Act. Metall., **34**, 629 (1986).

6.2 Y. Saito, Phys. Rev. B, **26**, 6239 (1982).

6.3 A. P. Young, Phys. Rev. B, **19**, 1855, (1979); R. Morf, Phys. Rev. Lett., **43**, 931 (1979).

6.4 J. Lee and K. J. Strandburg, Phys. Rev. B, **46**, 11190 (1992).

6.5 J. A. Zollweg and G. V. Chester, Phys. Rev. B, **46**, 11186 (1992).